Meso-Neoarchean magmatism and episodic crustal growth in the Kudremukh-Agumbe granite-greenstone belt, western Dharwar Craton, India

Arijit Pahari, Li Tang, C. Manikyamba, M. Santosh, K.S.V. Subramanyam, Sohini Ganguly

PII: S0301-9268(18)30294-8
DOI: https://doi.org/10.1016/j.precamres.2019.01.005
Reference: PRECAM 5256

To appear in: *Precambrian Research*

Received Date: 29 May 2018
Revised Date: 29 November 2018
Accepted Date: 6 January 2019

Please cite this article as: A. Pahari, L. Tang, C. Manikyamba, M. Santosh, K.S.V. Subramanyam, S. Ganguly, Meso-Neoarchean magmatism and episodic crustal growth in the Kudremukh-Agumbe granite-greenstone belt, western Dharwar Craton, India, *Precambrian Research* (2019), doi: https://doi.org/10.1016/j.precamres.2019.01.005

Meso-Neoarchean magmatism and episodic crustal growth in the Kudremukh-Agumbe granite-greenstone belt, western Dharwar Craton, India

Arijit Pahari[a], Li Tang[c], C. Manikyamba[a], M. Santosh[b, c], K.S.V. Subramanyam[a], Sohini Ganguly[d]

[a]*National Geophysical Research Institute (Council of Scientific and Industrial Research), Uppal Road, Hyderabad 500 007*
[b]*Department of Earth Sciences, University of Adelaide, SA 5005, Australia*
[c]*School of Earth Science and Resources, China University of Geosciences, Beijing, China*
[d]*Department of Earth Science, Goa University, Taleigao Plateau, Goa 403206, India*

*E-mail: cmaningri@gmail.com

Abstract

Mafic volcanic rocks and dykes associated with Na-rich TTG and K-rich granites in the Kudremukh greenstone belt of western Dharwar Craton provides a window to Precambrian crustal evolution in the southern Peninsular India. Here we present zircon U-Pb geochronology and geochemistry of these rocks to constrain the greenstone-basement relationship and crustal growth events in the western Dharwar Craton. TTGs exhibit fractionated REE patterns [$(La/Yb)_N$= 11.8-50.3; $(Gd/Yb)_N$=2.1-4.9] whereas the granites with K_2O contents of 3.84-5.20 wt.% are peraluminouscalc-alkaline with moderate enrichment of LREE over HREE and depleted MREE abundances. The metabasalts are characterized as arc basalts with moderate to high Fe_2O_3, CaO, SiO_2, MgO, LILE, LREE and low HFSE contents. The higher Nb contents (6.2-11.4 ppm) in some of them, classify them as Nb-enriched basalts, were erupted at 2498±43 Ma, indicating a 2.5 Ga greenstone volcanism in the western Dharwar Craton. These are characterized by slightly fractionated chondrite normalized REE along with negative Nb, Zr, Hf and Ti anomalies on the primitive mantle normalized trace element patterns. The amphibolitic and doleritic dykes have overlapping chemistry with moderate Al_2O_3, moderate to high Fe_2O_3 and MgO displaying coherent chondrite normalized REE patterns. The 3068±34 Ga TTG were generated through high pressure melting of mafic crust in a garnet-spinel peridotite mantle regime with the assimilation of upper crustal material in a subduction zone environment. The granites of 2936±23 Ma were the products of partial melting and fractional crystallization of TTG melts which display intrusive relationship with the thickened TTG crust. The mafic volcanism took place at 2498 ± 43 Ma subsequently followed by the dyke emplacement at 2484 ± 29 Ma. Therefore, two major episodes of crustal growth are identified from this region: i) TTG-granite association ~3.0-2.9 Ga and ii) mafic volcanism - dyke emplacement between 2.49-2.48 Ga. The geochemical signatures of arc basalts and Nb enriched basalts indicate variable-slab-mantle interactions including fluid-fluxed metasomatism and melt-fluxed hybridization of mantle wedge in a subduction zone environment followed by the emplacement of amphibolitic dykes during post-subduction collision phase. Our results document the episodic growth of continental crust in western Dharwar Craton from 3.0-2.5 Ga.

Keywords: Meso-Neoarchean magmatism; U-Pb zircon geochronology; Kudremukh-Agumbe greenstone belt; Dharwar Craton

1. Introduction

The Precambrian accretionary orogens exposed in ancient continental nuclei of worldwide cratons provide a comprehensive time window to decipher the geochemical and geodynamic evolution of the earth in terms of juvenile crust generation and continental growth. These are dominated by three lithological associations: (i) tonalitic-trondhjemitic-granodioritic (TTG) representing first differentiated continental crust, (ii) volcano-sedimentary greenstone sequences represent cyclic episodes of magmatism and sedimentation and (iii) voluminous late potassic granites which provide information on crustal reworking processes and stabilization of cratons (Komiya et al., 2017). Higher rate of juvenile crust generation and protracted magmatism are salient features of Precambrian accretionary

orogens in contrast to their Phanerozoic counterparts characterized by low rates of crustal growth (Polat, 2012; Zhai, 2014; Jayananda et al., 2015 and references there in). The spatially, temporally and genetically correlatable lithological assemblages of Paleo to Neoarchean granite-greenstone terranes (4.0-2.6 Ga) preserve characteristic geological and geochemical signatures that account for distinct magmatic pulses and tectonic cycles for episodic crustal growth at 3.8 Ga, 3.5-3.2 Ga, 2.8-2.7 and 2.6-2.5 Ga through vertical and lateral accretion of juvenile crustal materials under diverse geodynamic conditions at oceanic and continental realms (Kerrich et al., 1999; Smithies et al., 2003, 2009; Manikyamba and Kerrich, 2012; Manikyamba et al., 2014a, 2014b, 2015, 2016, 2017; Singh et al., 2018; Tang and Santosh, 2018). The Dharwar Craton represents a composite Archean protocontinent with distinct thermal and tectonic antiquities spanning from 3.8 to 2.5 Ga. The exposed basement gneisses, supracrustal associations and intrusive plutons provide unequivocal evidence of Archean crustal growth, accretionary processes and evolution of continental lithosphere. Recently, Jayananda et al. (2018) identified five major periods of felsic crust formation in the Dharwar Craton at 3450-3300 Ma, 3230-3150 Ma, 3000-2960 Ma, 2700-2600 Ma and 2560-2520 Ma which are suggested to be sub-contemporaneous with the greenstone volcanism.

Diverse magmatic suites are juxtaposed in most of the greenstone terranes through subduction-accretion processes, plume-arc and plume-craton-lithosphere interactions and arc-continent collisions (Polat and Kerrich, 2006; Polat et al., 1999; Kusky and Polat, 1999; Polat et al., 2002; Dostal and Mueller, 2013; Manikyamba et al., 2005; 2009, 2012, 2013; Smithies et al., 2005; Barnes and Van Kranendonk, 2014, Manikyamba and Kerrich, 2012; Santosh and Li, 2018) collectively contributing to Archean crustal growth, terrane accretion and tectonic evolution of early earth. Greenstone belt lithologies are well preserved in the western Dharwar Craton (WDC) and the available geochemical data reflect on plume-arc accretion for the generation of various litho units (Manikyamba et al., 2017). Besides, the basement-greenstone association is well preserved in the greenstone belts of WDC. The northwestern Kudremukh-Agumbe greenstone belt which is the westernmost belt of WDC has no comprehensive geochemical and geochronological studies to understand its evolution in terms of basement-greenstone relationship. Therefore, the present studies are focused on the geochemistry and age relationships of the TTG, granites and the greenstone lithologies to evaluate the overall crustal growth process in this greenstone belt of WDC.

The Kudremukh greenstone belt (KGB) of western Dharwar Craton (WDC) represents an integral part of the composite Shimoga-Western Ghat belt. This belt is exposed in the Western Ghats section bordering the western margin of Karnataka. Keeping in view of the continuity and petrographic and geochemical similarities of greenstone belt lithologies up to Agumbe (Fig. 1), the authors coin the Western Ghat belt as Kudremukh-Agumbe greenstone belt. It comprises TTG–granites association with thick accumulations of mafic volcanic rocks and dyke emplacementpreserving the history of distinct stages of magmatism and crust generation during the Meso-Neoarchean times. This paper presents field, petrological, whole rock geochemical and zircon U-Pb geochronological data for TTG -granite-metabasalt-mafic dyke association from Kudremukh-Agumbe greenstone belt in the WDC to provide a comprehensive understanding on magmatic and tectonic processes contributing to Archean crustal evolution in the Dharwar Craton. The petrogenetic and tectonic implications derived from the geochemical and geochronological data for the studied lithologies from Kudremukh-Agumbe greenstone belt address magma genesis and episodic crustal growth through subduction-accretion-collision processes during Meso- to Neoarchean timeframe.

2. Regional Geology

The Dharwar Craton (Fig. 1) represents one of the oldest landmasses of the Indian sub-continent preserving ancient continental nuclei with the volcano-sedimentary sequences of Archean greenstone belts that range in age from 3.6 to 2.5 Ga (Peucat et al., 1995; Balakrishnan et al., 1999; Chadwick et al., 2000; Jayananda et al., 2000, 2006, 2008; Ramakrishnan and Vaidyanadhan, 2010; Manikyamba et al., 2017; Jayananda et al., 2018). The Precambrian continental crust exposed in the Dharwar Craton is marked by a progressive transition from upper to lower crustal levels with granite-greenstone terranes grading southward into granulites (Swami Nath and Ramakrishnan, 1981; Janardhan et al., 1982; Radhakrishna, 1983; Jayananda et al., 2013a, 2013b). The major lithological components of the craton include 3.36–2.7 Ga Tonalite-Trondhjemite-Granodiorite (TTG), two generations of volcano-sedimentary successions (~3.3-3.1 Ga Sargur Group and 2.9–2.56 Ga Dharwar Supergroup) and 2.6–2.52 Ga calc-alkaline to potassic granitoid plutons (Chadwick et al., 2000; Jayananda et al., 2000, 2006, 2008, 2013a, 2013b; Chardon et al., 2011; Tushipokla and Jayananda, 2013) preserving records of Paleo to Neoarchean crust-building episodes that are well-correlatable with the magmatic and tectonic evolution as documented from other Archean cratons the of the world (Naqvi and Rogers, 1987; Manikyamba et al., 2004a, b, 2005, 2008, 2009, 2012, 2013, 2014c, 2015, 2017; Manikyamba and Kerrich, 2011, 2012; Jayananda et al., 2000; Chadwick et al., 2000; Moyen et al., 2003). The greenstone belts of WDC are composed of komatiite (3.38–3.32Ga)-tholeiites with subordinate felsic volcanic rocks (2.91–2.72 Ga) and interlayered quartzites, pelites, carbonates and BIFs. The emplacement of highly potassic granitoid plutons at 2.62–2.61 Ga represents the youngest magmatic activity (Nutman et al., 1992, 1996; Kumar et al.,

1996; Peucat et al., 1995, 2013; Jayananda et al., 2006, 2008, 2013a, 2013b; Chardon et al., 2011; Manikyamba et al., 2017). However, in EDC, the overall age of the greenstone belts is 2.7 Ga which are associated with 2.7 Ga gneisses (TTG) and intruded by younger granite of 2.5 Ga. The older peninsular gneisses are sporadic in the EDC (Balakrishnan et al., 1990, 1999; Krogstad et al., 1991; Jayananda et al., 2000; Chadwick et al., 2000; Moyen et al., 2003).

The WDC consists of migmatitic, tonalitic peninsular gneisses of 3.4–2.2 Ga with interlayered, highly deformed and metamorphosed, komatiite-rich Sargur Group (3.38–3.2 Ga) greenstone belts (Jayananda et al., 2008; Peucat et al., 1995) which are unconformably overlain by basalt-dacite-rhyolite rich 2.91–2.72 Ga supracrustals of the Dharwar Supergroup predominantly consists of metasediments along with the volcanic rocks (Kumar et al., 1996; Nutman et al., 1996; Jayananda et al., 2013a, 2013b). The TTG forms the basement for the greenstone belts which were accreted mainly during Mesoarchean (Peucat et al., 1993) along with Neoarchean (~2.6 Ga) potassic plutons (Taylor et al., 1984; Nutman et al., 1996; Jayananda et al., 2006). Two generations of greenstone sequences are present in the WDC, the older Sargur Group (~3.0 Ga) and the younger Dharwar Supergroup (2.9-2.5 Ga; Hokada et al., 2013). The Sargur Group greenstone belts are present as linear slivers and enclaves within the TTG in the southern part of the WDC in Holenarsipur, Nuggihalli, Krishnarajpet, Mayasandra, Nagamangala, Ghattihosahalli, Kalyadi, Banavara, and Hadanur areas. The 3.4–3.3 Ga Sargur Group greenstone belts consist of amphibolites, spinifex textured komatiites, komatiitic basalts, layered ultramafic sequences, subordinate anorthosite layers, banded iron formations (BIFs), quartzites, carbonates, pelites, fuchsite quartzite and other chemogenic argillaceous sediments (Swami Nath and Ramakrishnan, 1981; Jayananda et al., 2008; Tushipokla and Jayananda, 2013). The Gorur gneiss dated at 3.4 Ga near Kattaya in the western part of Holenarsipur belt shows tectonic contact with the Sargur Group greenstone belts reflecting their contemporary evolution. However, 3.6-3.5 Ga SHRIMP U-Pb zircon ages of the Gorur gneisses have also been reported (Jayananda et al., 2015; Guitreau et al., 2017). In contrast, the Bababudan and Chitradurga Groups are deposited on the quartz pebble conglomerate (QPC) classified as younger Dharwar Supergroup (2.9-2.6 Ga). The metavolcanics of Kudremukh is considered to be equivalent and lateral extent of Bababudan basin which are dated ca. 3020 ±230 Ma (Drury et al., 1983). The volcanic rocks of younger Dharwar Group are overlain by a thick sequence of BIFs, schists, greywackes and conglomerates in the Kudremukh-Agumbe, Shimoga, Bababudan and Chitradurga greenstone belts of WDC. Sm-Nd whole rock isochron reveals the age of 2.9-2.8 Ga for the volcanic rocks (Kumar et al., 1996). Detailed strain fabrics mapping and kinematic analysis in WDC reveal dome-basin patterns, sagducting greenstone ridges which are bordered by spaced shear zones (see Bouhallier et al., 1993; Chardon et al 1996, 1998, 2008). N-S trending brittle/ductile shear zones have been traced all along the eastern margins of the greenstone belts of WDC and EDC. The volcano-sedimentary sequences were metamorphosed to lower greenschist to upper amphibolite facies (Swami Nath and Ramakrishnan, 1981; Naqvi and Rogers, 1987). Younger belts are less metamorphosed in the northern region than their southern counterparts (Naqvi et al., 1988).

The Western Ghat is located in the westernmost part of the WDC and it is hosted by the Peninsular gneisses of Karnataka. The Western Ghat section of Karnataka comprises the Kudremukh-Agumbe greenstone belt covering 2200 sq. km and ranging from Jog falls to Agumbe-Kodachadri in the north. According to Beckinsale et al. (1980), the lithounits of Western Ghat belt are equivalent to the rocks of Bababudan Supergroup. In the Kudremukh-Agumbe greenstone belt, the basal Walkunje Formation consisting of oligomictic conglomerate, garnet bearing chlorite-biotite schist and quartzite (Table 1) which are unconformably resting on Peninsular gneisses. These conglomerates are overlain by metamorphosed volcano sedimentary rocks of Kudremukh Formation consisting of well-preserved mafic-ultramafic rocks, high Mg basalts, gabbros and BIFs. Recently, boninite-komatiite sequence has been reported by Chandan Kumar and Ugarkar (2017). The Kudremukh Formation is overlain by the Kodachadri Formation with a conformable contact and characterized by Algoma type oxide and silicate facies BIFs with the intercalation of quartz sericite chlorite schist (Sreeramachandra Rao, 1970). Within this formation, the lower Thirthabare iron formation is separated by thick sericite quartzite schist from the upper Sampekatte iron formation. The uppermost Narsiparvata Formation is dominated by medium grained quartz porphyry with prominent phenocryst of blue quartz and minor abundance of metavolcanics rocks. NNW-SSE trending doleritic and dioritic dykes are predominant in this Formation (Table 1; Ramakrishnan and Vaidyanadhan, 2010). The grade of metamorphism varies from upper greenschist to amphibolite facies. The Peninsular gneisses are granodioritic in composition with colour bands, ptygmatic folds along with other magmatic features (Mehnert, 1973). The K-Ar ages (biotite-hornblende gneiss) indicate a 3.2 Ga age whereas the Rb-Sr isochron yield an age of 3204±30 Ma (Balasubrahmanyan, 1976; Bhaskar Rao et al., 1991). The whole rock Sm-Nd and Rb-Sr ages of the metavolcanics from the Kudremukh area recorded 3020±230 Ma and 3280+-230 ages respectively (Drury et al., 1983). Detailed geochemical and geochronological studies to constrain the precise ages on the TTG, granites, volcanic rocks and intruded dykes from this belt are sparse. These studies are essential to unravel the genesis of metabasalts during the Meso-Neoarchean crustal evolution in the Kudremukh-Agumbe composite greenstone terrane representing the westernmost part of

WDC, as well as to evaluate the basement-greenstone relationship in terms of episodic crustal growth events and its mode of accretion. With this objective, this study presents comprehensive geological, geochemical and geochronological investigations on the TTG, granites, metabasalts and dykes from the Kudremukh-Agumbe composite greenstone terrane. Our results provide key constraints on the episodic growth of continental crust during 3.0-2.5 Ga in the WDC.

The exposed outcrops are very sparse due to thick vegetation and lateritic cover. Relatively least weathered samples were collected from this belt covering TTG, granites, metabasalts and dykes. The samples were collected away from shear zones, quartz and carbonate veins. The TTG were collected from quarries and fresh outcrops of Lakshmidevarahalli whereas the granites were collected from Kattimane village of Koppa ((Figs. 2A, B). The metabasalts along the ghat section are thick, massive, slightly foliated and schistose at some places. Further north, the NW-SE trending metabasalts are graded into garnetiferous amphibolites exposed along the Tunga river section having a sharp contact with the gneisses. The garnets are 3-4 cm embedded in the amphibolitic matrix showing the rusted appearance and traversed by numerous quartz veins. Metabasalts and mafic dykes have been sampled from well exposed Ghat sections of Kudremukh and Agumbe (Figs. 2C, D, E, F). After detailed petrography, fifty-one (51) samples of metabasalts; thirteen (13) samples of TTG; seven (7) samples of granites and ten (10) samples of basic dykes were powdered using agate mortar and analyzed for major, trace including rare earth elements (REE) at CSIR-National Geophysical Research Institute (CSIR-NGRI), Hyderabad, India. Major elements were determined by using pressed pellets on XRF (Phillips MAGIX PRO Model, 2440); with relative standard deviation <5%. Trace elements including REE were determined by HR-ICP-MS (Model: ATTOM, Nu Instruments, UK), following the procedure of closed vessel acid digestion technique (see Supplementary text).

3. Petrography

3.1. Tonalite-Trondhjemite-Granodiorite (TTG)

TTG are melanocratic to leucocratic with distinct banding and deformation evidenced by folding at some places. The TTG are characterized by high modal abundance of sodic plagioclase (An_{15-30}~55%), quartz (~25%) with minor orthoclase feldspar (<15%) and biotite (~5%) along with tourmaline, apatite, epidote and amphiboles as accessory minerals. The coarse to medium grained TTGs display crystalloblastic, hypidiomorphic, idioblastic and porphyritic textures (Fig 3A; phenocrysts of quartz and feldspar) along with intergrowth myrmikitic texture (Fig 3B) formed by irregular growth of quartz into albite. The interlocking textures manifested by quartz and sodic feldspars reflect on metamorphic recrystallization forming the mosaic of elongated aggregates. However, the undulatory extinction of quartz (Fig 3C) as well as thin lamella of feldspar in these TTG indicates recrystallization and solid-state deformation.

3.2 Granites

The studied granites are pink to grey in colour, homogeneous, devoid of any magmatic banding and are intrusive into the TTG. They display a consistent modal composition with microcline (~35%), Plagioclase feldspar (An_{16-32}~25%), quartz (~30%) and biotite (~10%). The accessory minerals are tourmaline, muscovite, zircon, apatite, titanite, magnetite. The granites are coarse grained, inequigranular with subhedral orthoclase, anhedral quartz and plagioclase. The microcline occurs between the interstitial spaces of anhedral quartz and plagioclase displaying intergranular texture (Fig 3D). At places, the cumulophyric, hypidiomorphic and porphyritic textures are also observed (Fig 3E). The perthitic texture is shown by the irregular veins and patches of sodic plagioclase in orthoclase feldspar (Fig 3F). The worm-like intergrowths of quartz in microcline form the graphic texture. Quartz and plagioclase are showing granophyric texture where they penetrate each other as feathery irregular intergrowth. Rarely, saussuritization is observed in some sections.

3.3. Metabasalt

The overall mineralogical composition of the metabasalts from Agumbe and Kudremukh are characterized by varying proportions of clinopyroxene, plagioclase and actinolite as essential minerals; chlorite and opaques as accessories (Fig. 3G). In most of the samples, parallel alignment of the actinolite reflects development of schistosity (Fig. 3H). The metabasalts are fine- grained and sparsely distributed inequigranular plagioclase, clinopyroxene and actinolite (Fig. 3I)

which is secondary after clinopyroxene. The metamorphic grade of the studied samples corresponds to greenschist to lower amphibolite facies reflected by chlorite-actinolite-plagioclase mineral association.

3.4. Dyke

Amphibolitic and doleritic dykes have been chosen for the present study. L-23 and L-30 series collectively consisting of six samples belong to amphibolitic type, characterized by large elongated crystals of hornblende embedded in a groundmass of plagioclase microlites showing porphyritic texture (Fig. 3J) in which the opaques are accessory phases. Iddingsitized olivine is observed in few samples. The lath shaped plagioclase and large crystals of pyroxenes are showing intergranular texture (Fig. 3K). L-22 series consisting of four samples which are doleritic in composition showing characteristic subophitic texture with partial engulfment of euhedral plagioclase laths by clinopyroxene (Fig. 3L) which is the most abundant mineral (~50%) in the doleritic variety. Plagioclase crystals show distinct lamellar twinning which is saussuritized at some places.

4. Zircon U-Pb Geochronology

Zircon grains from four samples including TTG (L-20), granitoid (L-29), Agumbe basalt (L-31), amphibolitic dyke (L-23) were analyzed for U-Pb geochronology. Representative Cathodoluminescence (CL) images of zircon grains along with U-Pb age and their concordia-discordia plots are discussed below. The obtained data on the studied samples for U-Pb zircon geochronology are presented in table 2

4.1. Tonalite-Trondhjemite-Granodiorite (TTG)

Zircon grains of TTG (L 20) are euhedral to subhedral and show near prismatic morphology. The grains size ranges between 50 to 150 µm and show length to width ratios of 2:1 to 1:1. In CL images, most grains show oscillatory zoning in the cores with core-rim texture. The oscillatory zoning cores display features of typical magmatic zircon, and the thin rims show bright and luminescence features around the zoned cores, representing typical metamorphic overgrowth (Figs. 4a, b; Kirkland et al., 2015; Kohn et al., 2015). A total of 26 spots were analyzed from 26 zircon grains. The age data obtained from the zircon cores are distributed along the Pb loss line, yielding upper intercept age of 3068 ± 34 Ma (MSWD = 2.5) with Th/U ratios of 0.36-1.02 (Figs. 4a, b; Table 2). The oscillatory zoning features and high Th/U ratios infer the age of 3068 Ma to represent the crystallization age of this rock (Kirkland et al., 2015). Zircon ages from rim domains were not obtained as the thin rims were not sufficient for analysis.

4.2. Granite

Zircon grains of granite (L 29) are translucent and light brown to colorless. The euhedral to subhedral grains show prismatic morphology with size ranges from 50-150 µm and length to width ratios of 3:1 to 1:1. In CL images, most zircons show oscillatory zoning or heterogeneous fractured domains, together with their relatively high Th/U ratios (0.14-1.37) suggesting magmatic origin (Figs. 4c, d; Table 2). A total of 26 spots were analyzed from 26 magmatic zircon grains. Five spots on the oscillatory zoned domains form a coherent group and fall on or near the concordia line, showing mean age of 2936 ± 23 Ma (MSWD = 1.2). Fifteen spots are distributed along a Pb loss line and yield an upper intercept age of 3063 ± 13 Ma (MSWD = 1.3). The remaining six zircon grains show older ages between 3119 ± 23 Ma and 3424 ± 24 Ma. Three age groups are identified based on the age data of sample L-29. The oldest population of 3119-3424 Ma is interpreted to represent the age of inherited magmatic zircons which show oscillatory zoned or heterogeneous fractured domains and relatively high Th/U ratios (0.14-1.37), and the remaining two groups with mean ages of 3063 ± 13 Ma and 2936 ± 23 Ma represent magmatic crystallization age. They do not show distinct features in CL images and chemistry, as all of them are magmatic zircons with zoning patterns. The zircons have typical magmatic features in CL images and relatively high Th/U ratios (0.14-1.37), implying the oldest zircon population of 3119-3424 Ma to represent the age of inherited zircons, and the mean ages of 3063 ± 13 Ma and 2936 ± 23 Ma representing magmatic crystallization at ca. 3.0 Ga (Figs. 4 c, d; Table 2).

4.3. Agumbe basalt

Zircon grains are rare in L 31 which are light brown to colorless and translucent with near prismatic to irregular morphology ranging in size between 50 to 200 µm. In CL images, most grains show oscillatory zoning and few zircon grains display core-rim texture with thin and bright rims (Figs. 4 e, f). A total of 8 spots were analyzed from 8 zircon grains. Two analytical spots have $^{207}Pb/^{206}Pb$ ages of 2494 ± 32 Ma to 2502 ± 30 Ma with a mean age of 2498±43 Ma (MSWD = 0.03) and

Th/U ratios (0.25-0.26), probably indicating the formation age of the basalt. The remaining four spots are distributed along the concordia line and show ages ranging from 1939 ± 37 Ma to 420 ± 4 Ma, implying multiple thermal overprints (Figs. 4 e, f; Table 2).

4.4. Dykes

Zircon grains in amphibolitic dyke (L 23) are light brown to colorless, and translucent with near prismatic morphology. The grains range in size between 40 to 150 μm and show aspect ratios of 2:1 to 1:1. In CL images, most grains show oscillatory zoning and few zircon grains displaying core-rim texture with very thin and bright rims (Figs. 4 g, h). A total of 28 spots were analyzed from 28 zircon grains. The age results obtained from the zircon cores are distributed along the Pb loss line, yielding upper intercept age of 2484 ± 29 Ma (MSWD = 1.8) with Th/U ratios of 0.03-0.98 (mean = 0.37), representing the intrusion age of the mafic dyke (Figs. 4 g, h; Table 2).

5. Geochemistry

It is essential to evaluate the elemental mobility due to alteration and metamorphism in the greenstone belt lithologies as they are metamorphosed to lower greenschist to upper amphibolites facies. The effect of alteration on the studied TTG and granites has been evaluated using the major element relationship such as K_2O/Na_2O vs. SiO_2, CaO, MgO, Al_2O_3, Fe_2O_3 and LOI which are consistently indicating their unaltered nature and the primary magmatic chemistry of these rocks (Páez et al., 2010; Fig. 5). Furthermore, the alteration box plot for the metabasalts and mafic dykes display the least altered nature of the studied samples (Large et al., 2001; Fig. 6A). In addition, their co-variance between the immobile elements, along with loss on ignition (< 2 wt.%) reflect the preservation of primary geochemical signatures in the analysed rocks (Fig. 6B, C, D, E). Besides, all the analyzed samples display a coherent REE and multielement patterns. The Ce/Ce* ratios of these rocks are in the range of 0.9-1.1 suggesting negligible LREE mobility (Polat et al., 2002). Therefore, the immobile trace elements and their ratios have been used for the petrogenetic and tectonic interpretations.

5.1. TTG and granites

The rocks of this belt show a broad spectrum of silica concentrations in TTG marked by relatively lower SiO_2 contents (63.57-69.73 wt.%) than the granites (70.45-77.14 wt.%). In terms of normative anorthite (An), albite (Ab) and orthoclase (Or) compositions the TTGs occupy the trondhjemite field while the granites correspond to field of granite (Fig. 7A). The Alumina Saturation Index (ASI) is a viable means to discriminate the granites and TTG. In the studied samples, the granites are occupying on the line dividing the meta and peraluminous character whereas the TTGs are predominantly peraluminous. These characteristics may reflect on the role of feldspars during their genesis (Fig. 7B;). The TTG have high alumina (15.36-17.38 wt.%) and alkalies (7.61-10.04 wt.%) with low K_2O/Na_2O ratio (0.31-0.52), low ferroan to high magnesian contents (Fe_2O_3+MgO+TiO_2+MnO<5%), low Mg# (15-28) and Ni composition (6-13 ppm; Table 3; Fig. 7C). The granites show relatively lower Al_2O_3 (12.10-15.93 wt.%) and total alkali (7.87-10.62 wt.%), Mg# (14-22) and Ni (6-8 ppm) compared to the TTG at a higher K_2O/Na_2O ratio (0.57-1.49). On the QAP diagram, TTG are classified as granodiorites indicating a calcic trend whereas the granites occupy the granite field displaying the intermediate calc-alkaline- trend (Fig. 7D). The MgO and Fe_2O_3 concentrations are relatively higher for TTG (MgO= 0.19-1.18 wt.%; Fe_2O_3= 1.14-3.14 wt.%) than that of granites (MgO= 0.09-0.30 wt.%; Fe_2O_3= 0.55-1.42 wt.%). On K_2O vs. SiO_2 plot, the TTG are straddling between the calc-alkaline to high K-calc-alkaline fields and the granites belong to high K calc-alkaline series (Fig. 7E). On K_2O-Na_2O-CaO diagram, the TTG and granites collectively indicating the common calc-alkaline trend (Fig 6F). Systematic decrease in Mg#, CaO, Al_2O_3, Y, Zr/Hf and La/Sm is observed with increasing SiO_2 reflecting their typical magmatic trends (Fig. 8). Trace and REE compositions (Table 3) of the studied samples show variable concentrations. Transitional trace elements like Ni, Co and Cr exhibit depleted concentrations with respect to the primitive mantle. Large ion lithophile elements (LILE) such as Rb, Sr, Ba show elevated abundances than high field strength (HFSE) elements such as Zr, Th, and Nb for both TTG and granites. Chondrite normalized REE patterns (Fig. 9A, C) for the TTG display pronounced LREE and MREE enrichment with sharp HREE fractionation trends $(La/Yb)_N$= 11.82-50.33; $(Gd/Yb)_N$= 2.17-4.89), while the granites with $(La/Yb)_N$= 1.81-3.19 and $(Gd/Yb)_N$= 0.61-0.86 conform to moderate enrichment of LREE over HREE with depleted MREE abundances. Granites are displaying distinct negative Eu anomalies indicative of plagioclase fractionation from the parent magma (Eu/Eu*<1) whereas the TTG are showing minor positive Eu anomalies (Eu/Eu*=0.8-1.4). On the primitive mantle normalized multielement diagram (Figs. 9 B, D) both TTG and granites exhibit negative U, Nb and Ti anomalies.

5.2. Metabasalts

The metabasalts from Kudremukh and Agumbe Ghat sections are compositionally characterized by a non-uniform spectrum of major element concentrations with 46.58 to 52.78 wt.% SiO_2, moderate to high Al_2O_3 (11.53 to 15.07 wt.%), Fe_2O_3 (10.86 to 16.99 wt.%), MgO (4.37-9.87 wt.%), CaO (5.26-13.57 wt.%) and moderate TiO_2 (0.78-1.57 wt.%). Mg# ranging from 26-46 suggests evolved nature of these metabasalts (Table 3). Based on total alkali vs. silica as well as the immobile element relationship (Fig. 10A, B; Le Bas et al., 1986), the studied samples are classified as subalkaline basalts and reflect a tholeiitic trend for precursor magma compositions on AFM plot (Fig. 10C). MgO exhibits strong to moderate negative correlations for SiO_2, TiO_2 and alkalies thereby indicating fractional crystallization of olivine and early formed plagioclase. CaO, Cr and Ni show strong positive correlations with MgO suggesting involvement of clinopyroxene during fractional crystallization (Fig. 11).

In general, island arc basalts have Nb content <2 ppm while Nb enriched basalts (NEB) possess >7 ppm Nb (Defant et al., 1992; Sajona et al., 1996). The Nb contents of the studied samples range from 2.98 to 11.45 ppm at 4.37-9.87 wt.% MgO. The widely varying Nb concentrations classify the metabasalts as Nb enriched basalts (NEB; Nb: 6.2-11.45 ppm, MgO: 4.4-9.5 wt.%) and normal arc basalts (Nb: 2.98-5.83 ppm, MgO: 5.3-9.9 wt.%).

5.2.1. Nb enriched basalts

The high Nb signatures (6.20 to 11.44 ppm Nb) of the metabasalts are substantiated by relatively higher Nb/Th (1.78-7.62) and Nb/Yb (2.31-5.92) ratios with low magnitude of negative Nb anomalies than normal intra-oceanic arc basalts. Among transitional trace elements, the NEB samples show moderate concentrations of Co (37-66 ppm) with widely varying Cr (24-693 ppm) and Ni (32-374 ppm) contents. REE chemistry of NEB from this greenstone belt reflects prominent LREE enrichment marked by La=8.67 to 18.77 ppm and Ce=22.43-45.48 ppm with ∑REE concentrations ranging from 62.50-125.74 ppm. The enriched ∑REE along with slight LREE fractionation in the NEB than the island arc basalts reflect the predominance of actinolite in them. Chondrite normalized REE patterns exhibit negative Eu anomalies (Eu/Eu*=0.33-0.60 except L32/4; Table 3) in combination with (i) pronounced LREE enrichment over MREE and HREE, sharp LREE/MREE and LREE/HREE fractionation trends corroborated by $(La/Sm)_N$ =1.37-3.03 and $(La/Yb)_N$= 2.20-9.97 respectively and (ii) moderate MREE enrichment over HREE and MREE/HREE fractionations depicted by $(Gd/Yb)_N$=1.06-2.69 (Figs. 12A,C). Primitive mantle normalized trace element abundance patterns (Figs. 12B, D) for the studied NEB show enrichment of compatible trace elements such as Th, La, Ce and relative depletion of incompatible elements Nb and Ti with enrichment and depletion of Zr and Hf. Magnitudes of negative Nb anomalies of NEB are high compared to their low Nb counterparts. Zr/Hf, Zr/Sm and Nb/Ta ratios for the studied NEB (Zr/Hf: 29.11-53.21; Zr/Sm: 16.40-37.93; Nb/Ta: 3.06-18) shows variable ranges with respect to the primitive mantle values (Zr/Hf: 36, Zr/Sm: 25, Nb/Ta: 17).

5.2.2. Island arc basalts

These are low Nb (2.98-5.83 ppm) basalts from this belt, show low to moderate Nb/Th (1.95-6.06) and Nb/Yb (1.23-3.06) in comparison with their high Nb counterparts. These are geochemically similar with the island arc basalts. ∑REE ranges from 35.86-84.84 ppm with LREE enrichment characterized by 4.72-14.53 ppm La, 11.43-31.64 ppm Ce. Chondrite normalized REE patterns reflect negative Eu (Eu/Eu*=0.38-0.61) anomalies with moderate to strong LREE/HREE [$(La/Yb)_N$=1.59-5.09]; moderate LREE/MREE [$La/Sm)_N$=1.40-2.58] and feeble to moderate MREE/HREE [$(Gd/Yb)_N$=0.91-1.65] fractionations (Fig. 12E). Primitive mantle normalized trace element patterns (Fig. 12F) are similar to their high Nb counterparts. Zr/Hf, Zr/Sm and Nb/Ta ratios show wide variations relative to the primitive mantle values of 17, 36 and 25 respectively.

5.3. Dykes

The amphibolitic and doleritic dykes from this greenstone belt shares uniform major element chemistry (Table 3) characterized by moderate silica contents varying between 45.56-46.93 wt.%; moderate Al_2O_3 (14.44 -15.01 wt.%), moderate to high Fe_2O_3 (12.05-14.22 wt.%); and MgO (10.13-13.11 wt.%) abundances. The studied samples characterized by total alkali content in the range of 1.63-2.35 wt.% occupy the field of basalt in total alkali vs. silica diagram (Fig. 10A, B) and display tholeiitic trend on AFM diagram (Fig. 10B). Variation trends for major elements with respect to MgO show negative correlations consistent with normal

magmatic differentiation controlled by fractional crystallization (Fig 11.). The doleritic and amphibolitic dykes show coherent trace and REE compositions marked by elevated abundances of compatible elements with respect to incompatible elements. Among transitional trace elements, the amphibolitic and doleritic dykes have overlapping abundance of Cr (643-1280 ppm; 1092-1234 ppm respectively) at a similar range of MgO, uniform Ni (188-377 ppm) and Co contents (60-91 ppm). Total REE concentrations for both dykes vary from 30 to 55 ppm. The amphibolitic [La=4.39-8.32 ppm; Ce=9.41-18.73 ppm; $(La/Sm)_N$ =1.75-2.08] and doleritic [La= 4.74-7.50 ppm; Ce=10.03-17.25 ppm; $(La/Sm)_N$= 1.68-2.18] dykes exhibit pronounced LREE enrichment. Chondrite normalized REE patterns (Fig. 12G) display LREE enrichment over MREE and HREE with prominent LREE/MREE and LREE/HREE fractionation trends substantiated by $(La/Sm)_N$ =1.75-2.08 and $(La/Yb)_N$ = 2.67-4.60 for amphibolitic dyke and $(La/Sm)_N$= 1.68-2.18, $(La/Yb)_N$=2.67-4.17 for the doleritic variety respectively. MREE/HREE fractionation reflect relatively smooth patterns for amphibolitic [$(Gd/Yb)_N$= 1.21-2.06] and doleritic [$(Gd/Yb)_N$= 1.04-2.01] dykes of this belt. Primitive mantle normalized multielement diagram (Fig. 12H) depicts prominent depletion over compatible elements such as La, Ce and Th over Nb and Ti. Both depletion and enrichment are observed in the Zr and hf in these dykes and other incompatible elements. Zr and Hf show depletion to enrichment. The negative Eu anomalies reflect the fractionation of plagioclase from the parent melts (Eu/Eu*<1).

6. Discussion

6.1. Origin of TTG and granites: Crust-mantle processes

Geochemical attributes have classified TTGs as high, medium and low-pressure types (Moyen et al., 2006; Moyen, 2011). The high-pressure (HP) type is relatively enriched in Al_2O_3, and Sr, depleted in Y, Yb, Ta and Nb, and shows highly fractionated REE patterns. It is considered to form under *P-T* conditions of 1.5-2.0 GPa and 700-900°C through partial melting of rutile-bearing eclogite in oceanic subduction zones with low-medium geothermal gradients of 10-30°C/km. The low-pressure (LP) TTG are characterized by contrasting geochemical characteristics with the HP type and is considered to form under *P-T* conditions of 1.0-1.2 GPa and 900–1000°C through partial melting of garnet amphibolite in the presence of abundant plagioclase in oceanic plateau settings with high geothermal gradients of 30–50°C/km. The medium-pressure (MP) TTG exhibits the geochemical characteristics between the HP and LP types, attributed to partial melting of garnet-rich and plagioclase-poor amphibolite in an intra-oceanic thickened arc crust. The principal models explaining the origin of TTGs (Moyen and Laurent, 2018) include (i) melting of hot, subducted slab influenced by hotter Archean mantle in a subduction zone (Martin, 1986; Moyen and Martin, 2012); (ii) melting at the base of a thick oceanic crust associated with a basaltic oceanic plateau or delaminated portions below an oceanic plateau (Van Kranendonk et al., 2007; Bédard, 2006; Nair and Chacko, 2008; Polat, 2012) and (iii) fractionation of hydrous basaltic melts into tonalities involving amphibole and garnet (Arth et al., 1978; Barker, 1979; Maaløe, 1982; Smith et al., 1983; Davidson et al., 2007; Kleinhanns et al., 2003). Jayananda et al. (2015) studied the TTGs from various parts of WDC and identified low-Al and high-Al varieties in which the former is suggested to be derived through the melting of heterogeneous thickened oceanic crust at shallower depth (30-40 km; 10-12 kbar) while the latter has been derived from the melting of base of oceanic arc crust/oceanic plateau at a greater depth (>60 km; 14-18 kbar). The geochemical characteristics of TTG from the studied greenstone belt classified as high pressure (HP) type marked by elevated abundance of Al_2O_3 (15.36-17.38 wt.%), Na_2O (0.31-0.52%) and Sr (220.29-590.32 ppm), with depleted Y (5.03-33.54 ppm), Yb (0.43-2.09 ppm), Ta (0.74-4.00 ppm) and Nb (4.59-16.31 ppm) contents with highly fractionated REE patterns [$(La/Yb)_N$= 11.82-50.33; $(Gd/Yb)_N$= 2.17-4.89]. Further, moderate enrichment in incompatible elements (10 times of primitive mantle), negative Nb and positive Sr anomalies, low Zr (45-245 ppm), fractionated REE patterns, high Sr/Y (20-200), absence of Eu anomaly, depletion in transition elements (<20 ppm), moderate HFSE (Nb = 1-7 ppm) are the criteria of typical high pressure TTG which are met by the studied TTG from this belt (Laurent et al., 2014). In addition, the Ab-An-Or ternary plot along with $(Gd/Er)_N$ vs. MgO relationship clearly indicate the high and low pressure origin of the studied TTG and potassic granites respectively (Fig. 13A, B). The obtained REE trends of the TTGs are resembling with the high pressure TTG of Karelian and Kola Cratons of Fennoscandian Shield, Russia (Fig. 13C; Halla et al., 2009). On $(Yb)_N$ vs. $(La/Yb)_N$ discrimination plot, all the TTG are occupying the Archean TTG field correlating with the fields of Gorur gneiss, Siggeguda-Chikmagalur Eastern gneiss and Trondhjemite plutons (Jayananda et al., 2015), whereas the granites are displaying their arc nature (Fig. 13D). Based on the experimental studies conducted by Foley et at. (2002), Moyen (2011) and Moyen and Martin (2012) evaluated the global TTG and suggested that the low pressure TTG with subchondritic Nb/Ta ratios (<17.6) are derived from amphibolite source whereas the high pressure TTG with superchondritic Nb/Ta ratios (>17.5) are generated from eclogite and rutile bearing eclogite source. The mantle generated mafic melts are characterized by subchondritic Nb/Ta ratios (Niu, 2012 and references therein). Although Nb/Ta are subchondritic (1.6-6.2), other geochemical parameters such as $(Gd/Yb)_N$ (>1), very high $(La/Yb)_N$ ratio (11-55), low

HREE relative to LREE indicating that the studied TTGs are high pressure type derived from garnet bearing spinel peridotite mantle depth. Therefore, the geochemical features of the studied TTG suggest parent melt derivation by partial melting of a hot, rutile bearing, eclogitic subducted slab in an oceanic subduction regime (Rapp et al., 1991; Xiong et al., 2005). The K-enrichment in three samples of TTG (L16/4, 16/1 and 20/1) appear to reflect the influence of K-rich fluids during the intrusion of granites into these TTG.

Granittes are characterized by a large compositional diversity arising from different source compositions, variable melting conditions, complex chemical and physical interactions between mafic and felsic magmas, fractional crystallization and crustal contamination (DePaolo 1981; Thompson and Connolly, 1995; Ray et al., 2011). The negative correlation between SiO_2 vs. Mg#, CaO, Al_2O_3, Zr/Hf and La/Sm (Fig. 8) indicate the fractional crystallization as a dominant process. This is also evidenced through petrography by the presence of cumulus nature of K-feldspar, quartz and interstitial biotite showing intergrowth textures like perthite (Fig. 3F). Based on the field observations, geochemical and geochronological studies, it is suggested that the granites are derived from TTG melts. The intrusive nature of the studied granites into the TTG, the narrow gap in U-Pb zircon ages between TTG (3068 Ma) and granites (2936 Ma) along with coherent REE and trace element distribution patterns confirm the derivation of granites from the TTG. These observations are further supported by earlier studies which have documented the genesis of potassic granites from older TTG in the greenstone terranes of Dharwar (Moyen et al., 2003) and Congo Cratons (Shang et al., 2007).

6.2. Metabasalts: Subduction signatures and source characteristics

Primary basaltic magmas derived from partial melting of mantle peridotite are characterized by high Mg# (68-75) with 250-300 ppm Ni, 500-600 ppm Cr and 27-80 ppm Co contents (Hanson and Langmuir, 1978; Frey et al., 1978; Perfit et al., 1980; Jiang et al., 2017). The MgO, Ni, Cr, Co concentrations and Mg# (Table 3) of the studied metabasalts (including NEB and arc basalts) of this greenstone belt collectively attest partial melting of a chemically evolved, heterogeneous mantle source responsible for the parent magma generation which experienced variable extents of depletion-enrichment processes. The LILE-LREE enriched, HFSE depleted signatures of these rocks with respect to primitive mantle compositions also manifest pronounced negative anomalies at Nb, Zr-Hf and Ti. The average REE patterns of the studied metabasalts (arc basalts and Nb-enriched basalts) are comparable to IAB among the OIB, E-MORB and N-MORB (Fig. 14A). An OIB source component in magmatic rocks is corroborated by higher Nb and Ta with respect to primitive mantle (Zhao and Zhou, 2007, Wang et al., 2017). However, low to high magnitude of Nb in combination with negative Zr-Hf anomalies for the studied metabasalts discard the involvement of OIB mantle component or possible contamination of continental crust. Further, the negative Nb-Ti anomalies for the metabasalts (Figs. 12B, D, F) have Ta/La ratios (0.02-0.06) lower than primitive mantle (Ta/La: 0.06). The HFSE and HFSE/HFSE ratios serve as reliable geochemical proxies to probe melt extraction history of the sub-arc mantle wedge and address the enrichment-depletion characteristics of the melt source (McCulloch and Gamble, 1991; Pearce and Peate, 1995; Pearce et al., 2000; Pearce and Stern, 2006; Zhao and Zhou, 2007; Pearce, 2008; Manikyamba et al., 2009; 2015). The HFSE are particularly useful to constrain the nature of the mantle sources which may have been depleted by previous melt extraction events in back-arc basins (Woodhead et al., 1993; Elliott et al., 1997) or in arc settings (Grove et al., 2002). The lower Nb/Ta ratios for majority of these metabasalts (Nb/Ta: 3-23) with respect to primitive mantle (17) are interpreted to reflect previous melt extraction from the mantle wedge. Zr/Hf, Zr/Sm and Nb/Ta ratios indicate involvement of heterogeneous melting of different mantle sources that are responsible for the generation of Cenozoic island arc lavas such as (i) depleted MORB source in the sub-arc mantle wedge, (ii) MORB like source with signatures of slab melts having rutile-eclogite residues of cold, deep slabs and (iii) melts from hot shallow slabs having amphibole-garnet residue (Konig and Schuth, 2011; Xiong et al., 2011; Manikyamba et al., 2008; 2009; 2014a; 2015). The low and high Nb metabasalts from this greenstone belt are characterized by widely varying Zr/Hf, Zr/Sm and lower Nb/Ta ratios compared with the primitive mantle (Zr/Hf = 36, Zr/Sm = 25 and Nb/Ta = 17) endorsing subduction driven metasomatism, variable contributions from subduction components and enrichment of depleted MORB like mantle source in the sub-arc mantle wedge (Sun and Mc Donough, 1989; Konig and Schuth, 2011; Kerrich and Manikyamba, 2012; Singh et al., 2017). The troughs at Zr-Hf for the studied rocks (Figs. 12 B, D, F) are attributed to fractionation of a Zr-bearing phase like amphibole or magnetite during the hydrous metasomatism of mantle wedge. Metasomatic melts from the primitive mantle source have La/Nb ratios of 0.53, whereas those derived from a MORB source have a value of 1.02 (McKenzie and O'Nions, 1995; Lai et al., 2012; Manikyamba et al., 2015). The high La/Nb ratios for the metabasalts (0.98-3.30) suggest their derivation from a metasomatically enriched mantle source in a subduction environment. Ratios of Zr/Nb in Archean arc basalts are within the range of recent MORB (Zr/Nb= 11-39) thereby reflecting the depleted nature of Archean upper mantle (Polat et al., 1999; Wyman et al., 1999; Polat and Kerrich, 2002; Hollings and Kerrich, 2004, 2006; Polat and Munker, 2004; Wyman and Kerrich, 2009). The Zr/Nb ratios of the studied metabasalts (9.03-25.06) depict wide ranges

which overlap with that of N-MORB (Zr/Nb =11-39) and are also in conformity with oceanic primitive arc tholeiites (Zr/Nb= 9–87). These geochemical features in conjunction with variable Zr/Hf (metabasalts: 28.07-53.21), Zr/Sm (metabasalts: 13.00-42.86) and Nb/Ta (metabasalts: 3.06-22.87) against primitive mantle indicate depleted to enriched character of the mantle source through metasomatism by the influx of slab-derived components. Accordingly, we infer that the mantle source generating the parent magmas for the metabasalts experienced an interaction between depleted MORB-type sub-arc mantle wedge and subducting oceanic lithosphere through influx of subduction components and mantle wedge metasomatism during different stages of oceanic subduction.

6.3. Role of fluids and melts: Variable slab wedge interactions

Hydrous melts and slab-derived fluids serve as most viable agents for element transfer from slab to mantle wedge, metasomatism and melting of mantle wedge peridotite (Prigent et al., 2018). The fluid-immobile elements like HFSE are retained in the subducted slab, whereas fluid-mobile elements such as LILE and LREE are fluxed into the mantle wedge through slab-dehydrated fluids. The LILE-LREE enrichment and relative HFSE depletion of the studied metabasalts can be ascribed to infiltration of LILE-LREE rich fluids in the mantle wedge by fluid-transfer processes (Anderson et al., 1980; Saunders et al., 1980; Wilson and Davidson, 1984). Th/Ce ≥0.1 in some of the volcanic rocks of present study reflect minor contributions from melting of pelagic sediments over the subducted oceanic lithosphere (Hawkesworth et al., 1997). The Nd-Hf compositions of arc magmas reveal that in comparison with Hf, Nd behaves as a mobile element in slab-derived fluids/melts. Increased concentrations of Nd compared to Hf have been attributed to subduction-metasomatized mantle wedge (Pearce et al., 1992; Manikyamba et al., 2004b). Therefore, the LREE-HFSE systematics of the Kudremukh-Agumbe metabasalts are marked by elevated abundances of Nd with relative Hf depletion resulting into high Nd/Hf ratios (metabasalts: 2.25-11.34). Oceanic island arcs and active continental margins have higher Th/Yb and lower Ta/Yb due to magma generation from a metasomatized mantle (Deng et al., 2015). On Th/Yb vs. Nb/Yb diagram, the studied samples plot in the calc-alkaline field with an active continental margin affinity (Fig. 14B). The Th/Yb ratios for the Nb-enriched and normal arc basalts suggest variable extents of slab-mantle interactions induced by strong input from subduction-derived components (Fig. 14B). The arc basalts are collinear with the low Ce-Yb trend of Archean intraoceanic arc basalts from Pilbara Craton, South Africa and Abitibi greenstone belt, Canada. The Nb-enriched basalts with relatively higher Ce-Yb trend display their similarities with Wawa greenstone belt, Superior Province, Canada and Baltic Shield, Russia (Fig. 14C; Manikyamba et al., 2015). Further, the island arc basalt are correlatable with the Phanerozoic counterparts of Tonga Kermadec, Marianas and New Britain indicating their intraoceanic nature whereas the Nb-enriched basalts are resembling with the Aleutians and Andes thereby reflecting continental arc signatures (Figure not shown; Hawkesworth et al., 1993). The Nb/Y and Nb/Zr ratios are key indicators to discriminate between fluids or melt contributions from subducted slab into the mantle wedge (Munker, 1998; Zhao and Zhou, 2007). Rutile is stable in eclogitic subducted slabs and subducted sediments during dehydration or partial melting and therefore plays a major role in depleting Nb in arc magmas (Green, 1995; Zhao and Zhou, 2007). The arc basalts (Nb/Y: 0.12-0.24; Nb/Zr: 0.05-0.11) are characterized by low Nb/Zr and Nb/Y ratios endorsing residual rutile and amphibole in the slab along with dominant contributions from slab-derived fluids. The relatively higher Nb/Y and Nb/Zr ratios for the Nb enriched basalts suggest that their precursor melts were generated by interaction between siliceous slab melts and mantle wedge peridotite. The geochemical compositions of the studied basalts indicate that their mantle sources experienced both fluid and melt metasomatism above a subduction zone. The Nb enriched basalts shows evidence of a mantle source strongly modified by slab melts, whereas the geochemical compositions of arc basalts were mainly controlled by fluids. The parent magmas for arc basalts are products of slab-dehydration and wedge melting, while those of Nb enriched basalts were derived by melting of subducted oceanic slab associated with an active continental margin setting.

6*.4. Nb-enriched basalts: role of hybridized mantle wedge*

In general, the elevated Nb abundance in the NEB has been correlated with (i) melting of young, hot, subducted oceanic lithosphere under garnet amphibolite to eclogite facies conditions (ii) metasomatism and hybridization of mantle wedge by slab melts iii) presence of asthenospheric or lithospheric OIB component in the mantle wedge and (iv) incorporation of subducted sediments or assimilation of continental materials during magma ascent (Wyman et al., 2000; Zhang et al., 2005; Wang et al., 2007,2008, Manikyamba et al., 2015; Singh et al., 2017). Lower Nb/U in combination with higher La/Nb, Ba/Nb ratios (Table 3) for island arc basalts, Nb enriched basalts and mafic dykes of this greenstone belt compared to average crust (Nb/U: 8.45, Ba/Nb: 32.5, La/Nb: 1.5), N-MORB (Nb/U: 49.57, Ba/Nb: 2.70, La/Nb: 1.07), primitive mantle (Nb/U: 33.95, Ba/Nb: 9.8, La/Nb: 0.96) and OIB (Nb/U: 47.06, Ba/Nb: 7.29, La/Nb: 0.77) commensurate with the role of a metasomatized, enriched mantle source. Thus, lower Nb/U of Nb enriched basalts from Kudremukh-Agumbe greenstone belt do not support their generation by melting of OIB-enriched mantle source. Magmas derived from OIB source are characterized by positive Nb anomalies. However, the negative Nb anomalies for the studied Nb enriched basalts exclude the possibility of OIB component in the mantle source (Hollings and Kerrich, 2000; Polat and Kerrich, 2001; Wang et al., 2008;

Kerrich and Manikyamba, 2012; Liao et al., 2018). The geochemical signatures of the studied Nb enriched basalts suggest their generation through convergent margin processes where slab melts played a vital role in the metasomatism of the mantle wedge.

Amphibole is the most common Nb-bearing metasomatized phase in Nb enriched basalts (Ionov and Hofmann, 1995; Sajona et al., 1993, 1996). However, amphibole-ilmenite or amphibole-orthopyroxene also host Nb-Ta during the generation of Nb enriched basalts (Hollings and Kerrich, 2000; Polat and Kerrich, 2001). As amphibole is the most common mineral phase during the slab-wedge interaction, it is the common host for Nb in the melting of metasomatized mantle peridotite (Zhang et al., 2005). Melts of subducted oceanic slab are produced at >700°C and 75–85 km depth that carry greater amount of LREE and HFSE than the hydrous fluids and ascend to percolate through the mantle wedge resulting into its hybridization and metasomatism (Sajona et al., 1993; 1996; Kepezhinskas et al., 1995; 1996). Trace and rare earth element systematics of the studied Nb enriched basalts indicate partial melting of a hybridized peridotitic mantle (adakitic melt-mantle wedge interaction) leaving a mantle residue carrying Nb enriched phases (amphibole, ilmenite). These metasomatic minerals trap HFSE (Nb, Ti and Ta) and decomposition of these phases in the convecting mantle peridotite trigger partial melting at depths above the zone of slab melting generating Nb enriched basalts. Thus, slab-melting, wedge hybridization and partial melting of a metasomatized, mantle wedge dragged up to spinel peridotite mantle regime (from 80-120 km; Sajona et al., 1993) by subduction-induced convection in sub-arc mantle account for the generation of the Nb enriched basalts of this greenstone belt in the western Dharwar Craton as also observed in high Nb basalts from Penakacherla, Jonnagiri and Gadwal greenstone terranes of eastern Dharwar Craton (Manikyamba et al., 2017 and references therein) and Malangtoli lavas of Singhbhum Craton (Singh et al., 2017).

6.5. Amphibolitic and doleritic dykes: role of crustal contamination

The mafic dykes of Kudremukh-Agumbe belt are characterized by low SiO_2 (45.56-46.93 wt.%), high MgO (10.13-13.11wt.%) and Mg# (44-54) indicating the evolved nature of the parent melts derived from sub-continental lithospheric mantle (e.g., Hirajima et al., 1990; Yang et al., 1993; Zhang et al., 1994, 1995; Kato et al., 1997). The amphibolitic and dolerite dikes are further characterized by relatively lower Nb (1.25-3.50ppm), Zr (38-82 ppm), Th (0.67-1.15 ppm), and Rb (2.42–12.86 ppm) compared to upper crust (Nb=25 ppm, Zr=190 ppm, Th=10.5 ppm and Rb=84 ppm; Rudnick and Fountain, 1995; Rudnick and Gao, 2003) suggesting minor crustal contamination. Besides, moderate magnitude of negative Nb in combination with Zr-Hf anomalies for the studied mafic dykes discard the involvement of OIB mantle component in their source. The positive correlation between MgO and Ni, Cr, CaO indicate that the studied dykes experienced olivine and pyroxene dominated fractionation from a mafic magma. Similarly, the separation of plagioclase and Ti-bearing phases could account for the observed negative Eu and Nb anomalies in chondrite-normalized REE and primitive-mantle-normalized trace element patterns. The presence of negative Nb and Ti anomalies in the analyzed samples supports the fractionation of Fe–Ti oxides (e.g., rutile, ilmenite, and titanite) or that these magmas formed in a convergent margin environment with a residual Ti-bearing phase (e.g., spinel) in the mantle source during partial melting.

The lower Nb/Ta ratios of mafic dykes (Nb/Ta: 6.06-14.73) with respect to primitive mantle (17) are the signatures of depleted mantle wedge due to previous melt extraction. The Ba/La, Th/Yb, $(Hf/Sm)_N$ and $(Ta/La)_N$ relationship (Fig. 15A, B) of these dykes corroborate subduction-driven fluid-controlled mantle wedge metasomatism in an arc environment. The varying Zr/Hf (35-42), Zr/Sm (15-31) and lower Nb/Ta (6.03-14.73) ratios when compared to primitive mantle endorse subduction driven metasomatism, variable contributions from subduction components (Sun and Mc Donough, 1989; Konig and Schuth, 2011; Kerrich and Manikyamba, 2012; Singh et al., 2017). These dykes were influenced by the subduction zone signatures which is evidenced from the narrow age gap between the metabasalts (2498 Ma) and the amphibolitic dykes (2484 Ma) that are related to post subduction event. Their emplacement through thickened arc crust imparted crustal signatures in the studied dykes. It is suggested that these dykes were emplaced during the collision stage soon after subduction which is evident from the overlapping geochemical characteristics along with their U-Pb zircon ages.

6.6. Mantle melting and tectono-magmatic evolution

Trace element concentrations and their ratios are effective geochemical proxies to identify the mantle source characteristics by providing information about the degree and depth of partial melting, crustal assimilation and fractional crystallization (Lassiter et al., 1995; Condie, 2001; Reichow et al., 2005; Shellnut et al., 2014). The higher distribution coefficients of HREE (Yb and Y) for garnet are proxies for the degree and depth of mantle melting (Song et al., 2006). However, La, Sm and Gd are incompatible and have low garnet/melt partition coefficients (Irving and Frey, 1978; Kelemen, 1990; Rollinson, 2014). The La/Yb is strongly fractionated when melting occurs in the garnet stability field and slightly fractionated during melting in the spinel lherzolite domain (Yaxley, 2000; Xu et al., 2005; Lai et al.,

2012). The La/Yb ratio gives a measure of LREE/HREE fractionation and is particularly sensitive to the amount of garnet left in the restite which in turn reflects the degree of melting of a garnet lherzolite source (Condie, 2001). The $(La/Yb)_N$ ratios for the metabasalts (1.59-9.97) and mafic dykes (2.67-4.17) corroborate moderate to strong LREE/HREE fractionations corresponding to variable degree of partial melting of the mantle source. The $(La/Sm)_N$ ratios of the studied samples (metabasalts: 1.37-3.03; mafic dykes: 1.68-2.18) indicate that the melting domain corresponds to the stability field of garnet to spinel lherzolite. Partial melting in the garnet stability field results in high Dy/Yb ratios (>2.5), which is low (<1.5) in case of spinel stability field. The Dy/Yb ratios (1.5-2.5) for the studied volcanic rocks and dykes reflect on the garnet to spinel peridotite melting conditions. The metabasalts occupy the field of spinel-peridotite facies on Dy/Yb vs. La/Yb relationship (Fig. 16A). The Nb enriched basalts in particular corresponds to a mantle melting domain with garnet as residual phase in the restite. Plots for the amphibolitic and doleritic dykes on La/Sm vs. Sm/Yb (Fig. 16B) melting curve reflect 5-10% partial melting of a source having garnet to spinel lherzolitic composition at a variable depth. $(Gd/Yb)_N$ ratios for the metabasalts and mafic dykes (Table 3) suggest deeper to shallow level partial melting of mantle having garnet to spinel peridotite compositions.

The TTG and granites of this belt correspond to a subduction-collision related tectonic setting based on their Nb/Zr vs. Zr relationship (Fig. 17A). On Nb vs. Yttrium plot, the TTG and the granites occupy the volcanic arc field thereby attesting their subduction-related tectonic affinity (Fig. 17B). A typical arc related tectonic setting is envisaged for the studied metabasalts which are characterized by low and high Nb compositions (Figs. 17C). The Zr/Nb vs. Nb/Th plot for these metabasalts indicates a subduction-related tectonic environment whereas the overall geochemical characteristics further substantiate an active continental margin setting. Zr/Y vs. Zr relationship (Fig. 17D) corroborates an arc-related tectonic regime for the emplacement of the mafic dykes.

A summary of zircon data from the TTG (L-20), granitoid (L-29), metabasalt (L-31) and amphibolitic dyke (L-23) shows that majority of zircon grains in all these rock types are characterized by magmatic textures and high Th/U ratios. Core-rim textures with very thin and bright metamorphic rims are observed in few samples. Zircon grains from the TTG (L-20) yield upper intercept age of 3068 ± 34 Ma, and the granitoid (L-29) has a group of zircons yielded mean age of 3063 ± 13 and 2936 ± 23 Ma, recording the 3.06-2.94 Ga magmatism. The metabasalts were erupted during 2498±43 Ma. The mafic dyke (L-23) displays upper intercept age of 2484 ± 29 Ma, implying intrusion of the ~2.84 Ga mafic dyke into the greenstone belt lithologies. The obtained geochronological data suggest the tectonic evolution of the Kudremuh-Agumbe greenstone belt with distinct episodes of magmatism and crustal growth through subduction-accretion processes. A three-stage schematic tectonic model deciphers the magmatic and accretionary episodes contributing to the crustal evolution of this belt (Fig. 18). The genesis of high pressure type TTG is attributed to Mesoarchean subduction process with melting of hot, eclogitic oceanic slab producing the parental melts which were assimilated by the upper crustal material during their emplacement. Subsequently, the granites are produced through fractional crystallization of TTG melts in a thickened crust that are evidenced by their geochemical signatures including U-Pb ages (Fig.18A). The narrow age gap of the metabasalts and dykes indicate arc magmatism immediately followed by collision during ocean-continent convergence in an active continental margin setting, where the mafic dykes mark a Neoarchean intrusive activity during the collision stage. The Nb-enriched basalts from this belt provide insights into matured stage of Neoarchean oceanic subduction. Thus, the evolutionary history of Kudremukh-Agumbe greenstone belt in the western Dharwar Craton marked by episodic crustal growth through distinct magmatism and subduction-accretion processes during Meso- to Neoarchean timeframe involving development of TTG and granites followed by greenstone sequences and stabilized by dyke intrusion (Fig.18 B, C). The petrological, geochemical and geochronological signatures of Kudremukh-Agumbe greenstone belt collectively support episodic crustal growth in WDC and attest to the operation of Phanerozoic style convergent margin tectonics during Meso- to Neoarchean which is evidenced through TTG, granites, arc basalts, Nb enriched basalts and emplacement of dykes.

6.7. The greenstone belts of WDC – a geochronological perspective

The TTG occurring in the eastern margin of Kudremukh belt are younger (Kudremukh TTG=3068±34 Ma; present study) compared to the southernmost (Gorur TTG=3309±7 Ma) and eastern parts of WDC (Chitradurga gneiss=3350±9 Ma; Jayananda et al., 2015 and references therein). The reported ages combined with the present ages from Kudremukh Agumbe belt document that the gneiss-greenstone association developed within a short span of time at different intervals from 3.3-2.5 Ga in the WDC. This is evidenced through the present study wherein the U-Pb zircon ages of TTG are 3068±34 Ma and the mafic volcanism took place at 2498±43 Ma. The final accretionary phase is marked by the dyke activity at 2484±29 Ma. The granites are coeval intrusions into the TTG at 2936±23 Ma. The

available U-Pb zircon ages (Jayananda et al., 2015 and references there in) from various parts of WDC indicates an episodic crustal growth from 3.3-2.7 Ga in the WDC. The present study reports 2.5 Ga greenstone volcanism for the first time from the WDC documenting the extended crustal growth upto 2.5 Ga.

In the absence of age data, earlier workers (Chandan Kumar and Ugarkar, 2017) have assumed that the mantle was depleted at >3.3 Ga due to the repeated melt extraction up to ~3.0 Ga. According to them, the depleted upper mantle reservoir generated boninites through partial melting in an arc regime. Further, the authors also mentioned that the eruption of komatiitic lavas at 3.0 Ga through plume magmatism which is debatable as the generation of TTG crust in this part of Dharwar Craton took place 3068±34 Ma (present study). However, keeping in view of the mafic magmatism at 2498±43 Ma, the generation of komatiites through mantle activity could have been initiated prior to 2.5 Ga, but after 3.0 Ga, which depleted the upper mantle and initiated the island arc processes considering the Archean microblock concept of crustal growth (Jayananda et al., 2018). Our study provides clear evidence of mantle depletion, metasomatism and wedge hybridization at 3068±34 to 2498±43 Ma through the eruption of arc and Nb-enriched basalts.

Based on the SHRIMP U-Pb zircon ages of the felsic volcanic rocks, Jayananda et al. (2013a) documented two stages of crustal growth in the Dharwar Craton in which the 2.7-2.6 Ga crustal growth has been assigned to the greenstone belts present in the eastern margin of WDC whereas the 2.58-2.52 Ga is evidenced from the greenstone belts of EDC. The 2.7 Ga event is coinciding with the global crustal growth event which is missing in Kudremukh-Agumbe belt, the westernmost greenstone belt of WDC. The younger ages of TTGs, granites and mafic volcanics of this belt (3.0-2.9 Ga and 2.49-2.48 respectively) when compared to other greenstone belts of WDC reflect the latter stage of crustal growth, resembling with the timeframe of the greenstone belts of EDC (2.58-2.52 Ga). This punctuated, short lived and delayed mafic magmatism indicate the generation of oceanic crust at 2.5 Ga. In addition, based on lithological association, Naqvi (1983) proposed five stages of BIFs deposition in WDC wherein the third stage BIFs are associated with metavolcanics (~2.5 Ga) which might be the age of ocean basin closure. This stage of BIF deposition and associated metavolcanics is evidenced from this belt where extensive development of BIF took place and the associated volcanic rocks gave an age of 2.49 Ga. Further, the age gap between the TTG and metavolcanic rocks of this belt indicate a thermal quiescence for more than 500 million years. This is further substantiated by cessation of TTG generation (due to cooling of Earth) and change in mantle convection from two layered to whole mantle convection with a progressive cooling of Earth between 3.0-2.5 Ga (Condie, 2018). During Dharwar stage, the amalgamation of micro continental blocks/arc crust with younger greenstone belts acted as accretionary complexes along with TTGs which might have released the heat or acted as thermal insulators that led to the cooling and stabilization of craton (Kunugiza et al., 1996). Further, the accretionary tectonics indicates synchronous growth of TTG and greenstone belts (with bimodal volcanics, metasediments and younger granites). However, the Kudremukh-Agumbe belt is an exception, wherein the younger granites are missing and the age gap between TTG and greenstone lithologies reflect the possibilities of major convection changes or thermal instability of mantle. In other words, the present studies clearly interpret the concept that older greenstone belts are associated with older TTGs whereas younger ones like this belt have younger TTGs in WDC (Kunugiza et al., 1996). Although, several WDC greenstone belts have formed by same subduction polarity at different time frames, the mantle beneath them is widely varying in terms of temperature, composition and depth. Condie (2018) while describing 3.0 - 2.0 Ga Earth, suggested increasing proportion of basalts with “arc-like” mantle sources mostly derived from enriched (EM) and depleted (DM) mantle sources. The onset of a Great Thermal Divergence in the mantle after 2.5 Ga led to a decrease in the degree of mantle melting which initiated large lateral plate motions. Keeping in view of the obtained ages of TTG, granites, mafic volcanic rocks and intruded dykes, a 2.5 Ga volcanism has been identified for the first time and the globally recorded mafic magmatism at 2.7 Ga is missing in the Kudremukh-Agumbe greenstone belt.

7. Conclusions

- The composite Kudremukh-Agumbe greenstone terrane located in the northwestern part of WDC consists of TTG, intrusive granites, dominant mafic volcanic rocks and banded iron formations. The amphibolitic/doleritic dykes cut across the mafic volcanic rocks of this belt.
- The TTGs are high-pressure type, marked by elevated abundance of Al_2O_3, alkalis, Sr and depleted in Y, Yb, Nb and Ta. The metabasalts are classified as Island arc and Nb-enriched basalts on the basis of their geochemistry. The doleritic and amphibolitic dykes show similar geochemical characteristics with the metabasalts having variable Nb-Ta, Zr-Hf and Ti contents.
- The U-Pb zircon age of the TTG is 3068±34 Ma whereas the intrusive granites were emplaced at 2936±23 Ma. The associated metabasalts yielded an age of 2498±43 Ma and the dykes were emplaced at 2484±29 Ma indicating that the crustal growth in the Kudremukh-Agumbe belt is between 3.0 to 2.5 Ga.

- The available geological, geochemical and geochronological data of this belt reflect that the crust growth was initiated at ~3.0 Ga through partial melting of hydrated oceanic crust in an ocean-continent convergent zone. The granites were emplaced simultaneously at ~2.9 Ga through partial melting of TTG crust and subsequent fractional crystallization.
- The island arc and Nb-enriched basalts were subsequently erupted at ~2.5 Ga by the melting of mantle wedge and sub-arc mantle under the influence of slab derived melts in a subduction zone environment.
- The amphibolitic dykes were intruded at 2484±29 Ma during the post subduction collision stage which marked the cessation of the compression-accretion event in the Kudremukh-Agumbe greenstone belt.
- The geochronological data on various lithounits of this belt combined with the available ages from the adjacent greenstone belts of Sargur and Dharwar Groups reveal multiple crustal growth events from 3.3-2.5 Ga through plume-arc accretionary tectonics in the western Dharwar Craton.

Acknowledgements

The authors thank Dr. V. M. Tiwari, Director, CSIR-NGRI for permitting to publish this work. CM acknowledges the funds from Council of Scientific and Industrial Research (CSIR) to National Geophysical Research Institute through the projects of Ministry of Earth Sciences (No: MoES/PO(Geosci)/8/2014) and MLP 6406-28(CM). Arijit Pahari acknowledges the DST INSPIRE fellowship for pursuing the Ph D programme at NGRI. Drs. M. Satyanarayanan, S.S. Sawant, and A.K. Krishna are acknowledged for providing the geochemical data. The authors are grateful to Prof. Guochun Zhao for efficient editorial handling and anonymous reviewers for their critical and thought-provoking reviews which enhanced the scientific content of the manuscript.

Figure Captions

Fig. 1: A) showing different cratons of India. B) Geological map of Dharwar Craton (after Chardon et al., 2008; Jayananda et al., 2013b) and C) Geological map of Kudremukh-Agumbe composite greenstone belt (after Balasubramanyan et al ., 1976; Sampat Iyengar, 1910).

Fig. 2: Field photos of A) Tonalite Trondhjemite Granodiorite (TTG), B) Granite, C) Kudremukh basalt D) Agumbe basalt, E) Dolerite dyke and F) Amphibolitic dyke

Fig. 3: Photomicrographs A) showing the porphyritic and hypidiomorphic textures marked by quartz and albite in TTGs, B) exhibiting myrmikitic intergrowth texture formed by irregular growth of quartz into albite, C) The undulatory extinction of quartz and thin lamella of feldspar indicating recrystallization and solid-state deformation in TTGs, D) occurrence of microcline at the interstitial spaces of anhedral quartz and plagioclase showing intergranular texture in granites, E) Cumulophyric and hypidiomorphic textures marked by quartz and K-feldspar, F) Perthitic texture marked by irregular vein and patches of sodic plagioclase in K-feldspar in the granites, G) Laths of plagioclase, clinopyroxene and hornblende in the basalt of Kudremukh Ghat section, H) development of schistosity in the Agumbe basalt, I) metabasalts exhibiting intergranular texture with plagioclase, clinopyroxene, actinolite and opaques, J) Hornblende phenocrysts surrounded by plagioclase microliths in amphibolitic dyke showing porphyritic texture, K) large crystals of plagioclase and pyroxene showing intergranular texture in the doleritic dykes and L) sub-ophitic texture with partial engulfment of euhedral plagioclase laths by pyroxene in the doleritic dykes

Fig. 4: Cathodoluminescence (CL) images of representative zircons in the analyzed samples from gneisses (L 20; a, b), granites (L 29; c, d) Agumbe basalt (L 31; e, f) and dyke (L 23; g, h). Blue circles represent U-Pb age of various analyzed spots.

Fig. 5: Major element relationship showing the unaltered nature of TTG and granites.

Fig. 6: A) Alteration box plot showing the least altered nature of metabasalts and mafic dykes, B) to E) Relationship between different immobile elements and their ratios depicting their covariance.

Fig. 7: A) Ternary diagram An-Ab-Or displaying TTG and granite field (after O'Connor. 1965), B) Alumina Saturation Index (ASI) Vs. SiO_2 indicating the peraluminous and metaaluminous nature of the studied TTG and granites, C) SiO_2 vs. Ferroan Index (after Frost et al., 2001) showing magnesian to ferroan nature of TTGs and granites, D) QAP diagram in which the TTGs occupy granodiorite field and Granites plotted in the granite field (after Strereckeisen., 1979) and trends (i) tholeiitic, (ii) alkaline, (iii) Intermediate calc-alkaline, (iv) K-rich calc-alkaline, (v) K-poor calc-alkaline are from Lameyre and Bowden (1982), E) SiO_2 Vs. K_2O relationship in which TTGs straddle between medium K to high K- calc-alkaline field and the granites have high K-calc-alkaline

characteristics (after Peccerillo and Taylor, 1976) and F) Trilinear K_2O-Na_2O-CaO diagram in which the studied TTG and granites are showing calc-alkaline trend (after Rajesh et al., 2018) and trends from Barker and Arth (1976).

Fig. 8: SiO_2 vs. major, trace elements and their ratios exhibiting magmatic trends for TTGs and granites.

Fig. 9: Chondrite normalized REE patterns displaying positive Eu anomaly in TTG (A) and negative Eu anomaly in the granites (C). Primitive mantle normalized trace element distribution pattern (B, D) showing negative Nb and Ti anomalies in TTGs and Granite both. Normalizing factors are from Sun and McDonough (1989).

Fig. 10: A) Total alkali vs. SiO_2 plot (Le Bas et al., 1986) in which basalts and dykes are occupying the field of basalts (Inset) and B) Relationship between the ratios of immobile trace elements indicating the sub-alkaline nature of the metabasalts and dykes (Winchester & Floyd (1977) and C) AFM diagram (Irvine and Baragar, 1971) indicating the tholeiitic trend of basalts and dykes.

Fig. 11: MgO Vs. major and transitional elements in the metabasalts and mafic dykes showing typical magmatic trends.

Fig. 12: Chondrite normalized REE and primitive mantle normalized trace element distribution patterns of Nb-enriched basalts (A, B, C, D), arc basalts (E, F) and dykes (G, H) displaying slight fractionation of LREE, negative Eu anomies along with negative anomalies of Nb and Ti. Normalizing factors are from Sun and McDonough (1989).

Fig. 13: A) Ab-An-Or ternary plot (after O'Connor. 1965), B) MgO Vs. $(Gd/Er)_N$ (after Halla et al., 2009) depicting the high and low pressure origin of TTG and granites respectively, C) Average REE patterns of TTG and granites of Kudremukh Agumbe belt showing similarities with the high pressure TTG of Karelian and Kola Cratons of Fennoscandian Shield, Russia (Data from Halla et al., 2009) and D) $(Yb)_N$ Vs. $(La/Yb)_N$ plot (after Hanson et al., 2002) in which the studied TTG are resembling with the TTG from the western Dharwar Craton (data from Jayananda et al. (2015) and granites are characterized as island arc type.

Fig. 14: A) Average REE patterns of the studied Nb-enriched and island arc basalts compared with OIB, N-MORB, EMORB and IAB (Data from Sun and McDonough, 1989 and Elliott et al., 2003), B) HFSE/HFSE ratio plots indicating oceanic to continental margin nature of the studied basalts (Pearce et al., 2005) and C) Ce Vs. Yb plot of the studied basalts occupying the fields of the island arc basalts from different Archean Cratons (after Manikyamba et al., 2015).

Fig. 15: A) Ba/La vs La/Yb (after Hou et al., 2012) and B) $(Ta/La)_N$ $(Hf/Sm)_N$ (after LaFl'eche et al., 1998) depicting fluid induced metasomatism in the amphibolitic and doleritic dykes.

Fig. 16: A) La/Yb vs. Dy/Yb (after Jung et al., 2006) and B) La/Sm vs. Sm/Yb (after Aldanmaz et al., 2000) showing spinel-peridotite-lherzolite melting regime for the studied metabasalts and dykes.

Fig. 17: A) Zr vs. Nb/Zr plot with fields from Thieblemont and Tegyey (1994) showing subduction-collision tectonic regime for the genesis of TTGs and granites, B) Y+Nb Vs. Nb (after Pearce et al., 1984) showing subduction origin for the TTG and granites, C) Zr/Nb vs Nb/Th (after Condie, 2005) displaying arc affinity of metabasalts and (D) Zr vs Zr/Y (Pearce and Norry, 1979) indicating island arc affinity for the amphibolites and dolerite dykes.

Fig. 18: Schematic tectonic model explaining A) the genesis of TTG through the melting of mafic oceanic crust and emplacement of granites through the partial melting of TTG crust and subsequent fractional crystallization during 3.0-2.9 Ga. B) Eruption of island arc and Nb-enriched basalts in a subduction zone setting by wedge melting and sub-arc mantle under the influence of slab derived melts during 2.98 Ga and C) The collision of arc and continent along with the emplacement of doleritic and amphibolitic dykes during post-subduction-collision at ~2.84 Ga.

References

Aldanmaz, E., Pearce, J.A., Thirlwall, M.F. and Mitchell, J.G., 2000. Petrogenetic evolution of late Cenozoic, post-collision volcanism in western Anatolia, Turkey. Journal of Volcanology and Geothermal Research 102, 67-95.

Anderson, R. N., Stephen, E. D., Schwarz, W. M., 1980. Dehydration, asthenospheric convection and seismicity in subduction zones. The Journal of Geology 88, 445–451.

Arth, J.G., Barker, F., Peterman, Z.E., and Friedman, I., 1978. Geochemistry of the gabbro-diorite-tonalite-trondhjemite suite of southwest Finland and its implications for the origin of tonalitic and trondhjemitic magmas. The Journal of Petrology 19, 289-316.

Balakrishnan, S., Hanson, G.N., Rajamani, V., 1990. Pb and Nd isotope constraints on the origin of high Mg and tholeiitic amphibolites, Kolar Schist Belt, South India. Contribution to Mineralogy and Petrology 107, 272–292.

Balakrishnan, A.S., Rajamani, V., Hanson, G.N., 1999. U - Pb Ages for Zircon and Titanite from the Ramagiri Area, Southern India : Evidence for Accretionary Origin of the Eastern Dharwar Craton during the Late Archean Evidence. The Journal of Geology 107, 69–86.

Balasubramanyan, M.S., Ram Mohan Rao, G., Venkataraman, S., 1976. The gneissic complex and kanara batholith , Mysore State. Geological Survey of India Miscelleneous Publication 23, 363-373.

Barker, F., 1979. Trondhjemite: definition, environment and hypotheses of origin. In Developments in Petrology 6, 1-12.

Barker, F. and Arth, J.G., 1976. Generation of trondhjemitic-tonalitic liquids and Archean bimodal trondhjemite-basalt suites. Geology 4, 596-600.

Barnes, S.J., Van Kranendonk, M.J., 2014. Archean andesites in the east Yilgarn craton, Australia: Products of plume-crust interaction? Lithosphere 6, 80–92.

Beckinsale, R.D., Gale, N.H., Pankhurst, R.J., Macfarlane, A., Crow, M.J., Arthurs, J.W. and Wilkinson, A.F., 1980. Discordant Rb-Sr and Pb-Pb whole rock isochron ages for the Archean basement of Sierra Leone. Precambrian Research 13, 63–76.

Bédard, J.H., 2006. A catalytic delamination-driven model for coupled genesis of Archaean crust and sub-continental lithospheric mantle. Geochimica et Cosmochimica Acta 70, 1188–1214.

Bhaskar Rao, Y.J., Naha, K., Srinivasan, R. and Gopalan, K., 1991. Geology, geochemistry and geochronology of the Archaean Peninsular gneiss around Gorur, Hassan district, Karnataka, India. Proceedings of the Indian Academy of Sciences-Earth and Planetary Sciences 100, 399-412.

Bouhallier, H., Choukroune, P. and Ballèvre, M., 1993. Diapirism, bulk homogeneous shortening and transcurrent shearing in the Archaean Dharwar craton: the Holenarsipur area, southern India. Precambrian Research 63, 43-58.

Chadwick, B., Vasudev, V.N. and Hegde, G.V., 2000. The Dharwar craton, southern India, interpreted as the result of Late Archaean oblique convergence.

Precambrian Research 99, 91-111.

Chandan-Kumar, B., Ugarkar, A.G., 2017. Geochemistry of mafic–ultramafic magmatism in the Western Ghats belt (Kudremukh greenstone belt), western Dharwar Craton, India: implications for mantle sources and geodynamic setting. International Geology Review 59, 1507-1531.

Chardon, D., Choukroune, P. and Jayananda, M., 1996. Strain patterns, décollement and incipient sagducted greenstone terrains in the Archaean Dharwar craton (south India). Journal of Structural Geology 18, 991-1004.

Chardon, D., Choukroune, P. and Jayananda, M., 1998. Sinking of the Dharwar basin (South India): implications for Archaean tectonics. Precambrian Research 91, 15-39.

Chardon, D., Jayananda, M., Chetty, T.R. and Peucat, J.J., 2008. Precambrian continental strain and shear zone patterns: South Indian case. Journal of Geophysical Research: Solid Earth 113, B08402.

Chardon, D., Jayananda, M., Peucat, J.J., 2011. Lateral constrictional flow of hot orogenic crust: Insights from the Neoarchean of south India, geological and geophysical implications for orogenic plateaux. Geochemistry, Geophysics, Geosystems 12, 1–24.

Condie, K.C., 2001. Mantle plumes and their record in Earth history. Cambridge University Press.

Condie, K.C., 2005. High field strength element ratios in Archean basalts: A window to evolving sources of mantle plumes? Lithos 79, 491–504.

Condie, K. C. 2018. A Planet in transition: The onset of plate tectonics on Earth between 3 and 2 Ga? Geoscience Frontiers 9, 51-60.

Davidson, J., Turner, S., Handley, H., Macpherson, C., Dosseto, A., 2007. Amphibole "sponge" in arc crust? Geology 35, 787–790.

Defant, M.J., Jackson, T.E., Drummond, M.S., De Boer, J.Z., Bellon, H., Feigenson, M.D., Maury, R.C. and Stewart, R.H., 1992. The geochemistry of young volcanism throughout western Panama and southeastern Costa Rica: an overview. Journal of the Geological Society 149, 569-579.

Deng, Y., Yuan, F., Zhou, T., Xu, C., Zhang, D. and Guo, X., 2015. Geochemical characteristics and tectonic setting of the Tuerkubantao mafic-ultramafic intrusion in West Junggar, Xinjiang, China. Geoscience Frontiers 6, 141-152.

De Paolo, D.J., 1981. Trace element and isotopic effects of combined wall rock assimilation and fractional crystallization. Earth and Planetary Science Letters 53, 189-202.

Dostal, J., Mueller, W.U., 2013. Deciphering an Archean mantle plume: Abitibi greenstone belt, Canada. Gondwana Research 23, 493–505.

Drury, S.A., Holt, R.W., Van Calsteren, P.C., Beckinsale, R.D., 1983. Sm-Nd and Rb-Sr ages for Archaean rocks from western Karnataka, South India. Journal of the Geological Society of India 24, 454–459.

Elliott, T., Plank, T., Zindler, A., White, W., Bourdon, B., 1997. Element transport from slab to volcanic front at the Mariana arc. Journal of Geophysical Research: Solid Earth 102, 14991-15019.

Elliott, T., 2003. Tracers of the slab. Goephysical Monograph-American Geophysicl Union 138, 23-46.

Foley, S., Tiepolo, M. and Vannucci, R., 2002. Growth of early continental crust controlled by melting of amphibolite in subduction zones. Nature 417, 837.

Frey, F.A., Green, D.H. and Roy, S.D., 1978. Integrated models of basalt petrogenesis: A study of quartz tholeiites to olivine melilitites from South Eastern Australia utilizing geochemical and experimental petrological data. The Jounal of Petrology 19, 463-513.

Frost, B.R., Barnes, C.G., Collins, W.J., Arculus, R.J., Ellis, D.J. and Frost, C.D., 2001. A geochemical classification for granitic rocks. The Journal of petrology 42, 2033-2048.

Green, T.H., 1995. Significance of Nb/Ta as an indicator of geochemical processes in the crust-mantle system. Chemical Geology 120, 347–359.

Grove, T., Parman, S., Bowring, S., Price, R., Baker, M., 2002. The role of an H_2O-rich fluid component in the generation of primitive basaltic andesites and andesites

from the Mt. Shasta region, N California. Contribution to Mineralogy and Petrology 142, 375–396.

Guitreau, M., Mukasa, S.B., Loudin, L. and Krishnan, S., 2017. New constraints on the early formation of the Western Dharwar Craton (India) from igneous zircon U-Pb and Lu-Hf isotopes. Precambrian Research. 302, 33-49.

Hansen, J., Skjerlie, K.P., Pedersen, R.B. and De La Rosa, J., 2002. Crustal melting in the lower parts of island arcs: an example from the Bremanger Granitoid Complex, west Norwegian Caledonides. Contributions to Mineralogy and Petrology, 143, 316-335.

Halla, J., van Hunen, J., Heilimo, E. and Hölttä, P., 2009. Geochemical and numerical constraints on Neoarchean plate tectonics. Precambrian Research 17, h155-162.

Hawkesworth, C.J., Gallagher, K., Hergt, J.M. 1993. Mantle and slab contributions in arc magmas. Annual Review of Earth and Planetary Sciences 21, 175–204.

Hawkesworth, C.J., Turner, S.P., McDermott, F., Peate, D.W. and Van Calsteren, P., 1997. U-Th isotopes in arc magmas: Implications for element transfer from the subducted crust. Science 276, 551-555.

Hanson, G.N., Langmuir, C.H., 1978. Modelling of major elements in mantle-melt systems using trace element approaches. Geochimica et Cosmochimica Acta 42, 725-741.

Hirajima, T., Ishiwatari, A., Cong, B., Zhang, R., Banno, S., Nozaka, T., 1990. Coesite from Mengzhong eclogite at Donghai county, northern Jiangsu province, China. Mineralogy Magazine 54, 579–583.

Hokada, T., Horie, K., Satish-Kumar, M., Ueno, Y., Nasheeth, A., Mishima, K., Shiraishi, K., 2013. An appraisal of Archaean supracrustal sequences in Chitradurga Schist Belt, Western Dharwar Craton, Southern India. Precambrian Research 227, 99–119.

Hollings, P., Kerrich, R., 2000. An Archean arc basalt–Nb-enriched basalt–adakite association: the 2.7 Ga Confederation assemblage of the Birch–Uchi greenstone belt, Superior Province. Contribution to Mineralogy and Petrology 139, 208–226.

Hollings, P., Kerrich, R., 2004. Geochemical systematics of tholeiites from the 2.86 Ga Pickle Crow Assemblage, northwestern Ontario: Arc basalts with positive and negative Nb-Hf anomalies. Precambrian Research 134, 1–20.

Hollings, P., Kerrich, R., 2006. Light rare earth element depleted to enriched basaltic flows from 2.8 to 2.7 Ga greenstone belts of the Uchi Subprovince, Ontario, Canada. Chemical Geology 227, 133–153.

Hou, T., Zhang, Z., Encarnacion, J. and Santosh, M., 2012. Petrogenesis and metallogenesis of the Taihe gabbroic intrusion associated with Fe–Ti-oxide ores in the Panxi district, Emeishan Large Igneous Province, southwest China. Ore Geology Reviews 49, 109-127.

Ionov, D.A., Hofmann, A.W., 1995. NbTa-rich mantle amphiboles and micas: Implications for subduction-related metasomatic trace element fractionations. Earth and Planetary Science Letters 131, 341–356.

Irvine, T.N.J., Baragar, W.R.A.F., 1971. A guide to the chemical classification of the common volcanic rocks. Canadian Journal of Earth Sciences 8, 523-548.

Irving, A.J., Frey, F.A., 1978. Distribution of trace elements between garnet megacrysts and host volcanic liquids of kimberlitic to rhyolitic composition. Geochimica et Cosmochimica Acta 42, 771–787.

Janardhan, A.S., Newton, R.C., Hansen, E.C., 1982. The transformation of amphibolite facies gneiss to charnockite in southern Karnataka and northern Tamil Nadu, India. Contribution to Mineralogy and Petrology 79, 130–149.

Jayananda, M., Moyen, J.F., Martin, H., Peucat, J.J., Auvray, B., Mahabaleswar, B., 2000. Late Archaean (2550-2520 Ma) juvenile magmatism in the Eastern Dharwar craton, southern India: Constraints from geochronology, Nd-Sr isotopes and whole rock geochemistry. Precambrian Research 99, 225–254.

Jayananda, M., Chardon, D., Peucat, J.J., Capdevila, R., 2006. 2.61 Ga potassic granites and crustal reworking in the western Dharwar craton, southern India: Tectonic, geochronologic and geochemical constraints. Precambrian Research 150, 1-26.

Jayananda, M., Kano, T., Peucat, J.J., Channabasappa, S., 2008. 3.35 Ga komatiite volcanism in the western Dharwar craton, southern India: Constraints from Nd

isotopes and whole-rock geochemistry. Precambrian Research 162, 160-179.

Jayananda, M., Peucat, J.J., Chardon, D., Rao, B.K., Fanning, C.M., Corfu, F., 2013a. Neoarchean greenstone volcanism and continental growth, Dharwar craton, southern India: Constraints from SIMS U-Pb zircon geochronology and Nd isotopes. Precambrian Research 227, 55–76.

Jayananda, M., Santosh, M., Jahn, B. ming, 2013b. Precambrian accretionary orogens. Precambrian Research 227, 1–3.

Jayananda, M., Chardon, D., Peucat, J.J., Tushipokla, Fanning, C.M., 2015. Paleo- to Mesoarchean TTG accretion and continental growth in the western Dharwar craton, Southern India: Constraints from SHRIMP U-Pb zircon geochronology, whole-rock geochemistry and Nd-Sr isotopes. Precambrian Research 268, 295–322.

Jayananda, M., Santosh, M. and Aadhiseshan, K.R., 2018. Formation of Archean (3600–2500 Ma) continental crust in the Dharwar Craton, southern India. Earth-Science Reviews 181, 12-42.

Jiang, H., Han, J., Chen, H., Zheng, Y., Lu, W., Deng, G. and Tan, Z., 2017. Intra-continental back-arc basin inversion and Late Carboniferous magmatism in Eastern Tianshan, NW China: Constraints from the Shaquanzi magmatic suite. Geoscience Frontiers 8, 1447-1467.

Jung, C., Jung, S., Hoffer, E., Berndt, J. 2006. Petrogenesis of Tertiary mafic alkaline magmas in the Hocheifel, Germany. The Journal of Petrology 47, 1637-1671.

Kato, T., Enami, A., Zhai, M., 1997. Ultrahigh-pressure marble and eclogite in the Su-Lu ultrahigh-pressure terrane, eastern China. Journal of Metamorphic Geology 15,169–182.

Kelemen, P.B., 1990. Reaction between ultramafic rock and fractionating basaltic magma I. phase relations, the origin of calc-alkaline magma series, and the formation of discordant dunite. The Journal of Petrology 31, 51–98.

Kepezhinskas, P.K., Defant, M.J., Drummond, M.S., 1995. Na metasomatism in the island-arc mantle by slab melt-peridotite interaction: Evidence from mantle xenoliths in the north Kamchatka arc. The Journal of Petrology 36, 1505–1527.

Kepezhinskas, P., Defant, M.J., Drummond, M.S., 1996. Progressive enrichment of island arc mantle by melt-peridotite interaction inferred from Kamchatka xenoliths. Geochimica et Cosmochimica Acta 60, 1217–1229.

Kerrich, R., Manikyamba, C., 2012. Contemporaneous eruption of Nb-enriched basalts - K-adakites - Na-adakites from the 2.7 Ga Penakacherla terrane: implications for subduction zone processes and crustal growth in the eastern Dharwar craton, India. Canadian Journal of Earth Sciences 49, 615–636.

Kerrich, R., Wyman, D., Hollings, P. and Polat, A., 1999. Variability of Nb/U and Th/La in 3.0 to 2.7 Ga Superior Province ocean plateau basalts: implications for the timing of continental growth and lithosphere recycling. Earth and Planetary Science Letters 168, 101-115.

Kohn, M.J., Corrie, S.L. and Markley, C., 2015. The fall and rise of metamorphic zircon. American Mineralogist 100, 897-908.

Kirkland, C.L., Smithies, R.H., Taylor, R.J.M., Evans, N. and McDonald, B., 2015. Zircon Th/U ratios in magmatic environs. Lithos 212, 397-414.

Kleinhanns, I.C., Kramers, J.D., Kamber, B.S., 2003. Importance of water for Archaean granitoid petrology: A comparative study of TTG and potassic granitoids from Barberton Mountain Land, South Africa. Contribution to Mineralogy and Petrology 145, 377–389.

Komiya, T., Yamamoto, S., Aoki, S., Koshida, K., Shimojo, M., Sawaki, Y., Aoki, K., Sakata, S., Yokoyama, T.D., Maki, K. and Ishikawa, A., 2017. A prolonged granitoid formation in Saglek Block, Labrador: Zonal growth and crustal reworking of continental crust in the Eoarchean. Geoscience Frontiers 8, 355-385.

Konig, S., Schuth, S., 2011. Deep melting of old subducted oceanic crust recorded by superchondritic Nb/Ta in modern island arc lavas. Earth Planetary Science Letters 301, 265–274.

Krogstad, E.J., Hanson, G.N., Rajamani, V., 1991. U-Pb Ages of Zircon and Sphene for Two Gneiss Terranes Adjacent to the Kolar Schist Belt, South India: Evidence for Separate Crustal Evolution Histories. The Journal of Geology 99, 801–815.

Kumar, A., Rao, Y.J.B., Sivaraman, T.V., Gopalan, K., 1996. Sm-Nd ages of Archaean metavolcanics of the Dharwar craton, South India. Precambrian Research 80,

205–216.

Kunugiza, K., Kato, Y., Kano, T., Takaba, Y., Kuruma, I., Sohma, T., 1996. An Archean tectonic model of the Dharwar craton, southern India: the origin of the Holenarasipur greenstone belt (Hassan district, Karnataka) and reinterpretation of the Sargur-Dharwar relationship. Journal of Asian Earth Sciences 14, 149–160.

Kusky, T.M., Polat, A., 1999. Growth of granite-greenstone terranes at convergent margins, and stabilization of Archean cratons. Tectonophysics 305, 43–73.

La Flèche, M.R., Camire, G. and Jenner, G.A., 1998. Geochemistry of post-Acadian, Carboniferous continental intraplate basalts from the Maritimes Basin, Magdalen islands, Quebec, Canada. Chemical Geology 148, 115-136.

Lai, S., Qin, J., Li, Y., Li, S., Santosh, M., 2012. Permian high Ti/Y basalts from the eastern part of the Emeishan Large Igneous Province, southwestern China: Petrogenesis and tectonic implications. Journal of Asian Earth Science 47, 216–230.

Lameyre, J. and Bowden, P., 1982. Plutonic rock types series: discrimination of various granitoid series and related rocks. Journal of Volcanology and Geothermal Research 14, 169-186.

Large, R.R., Gemmell, J.B., Paulick, H. and Huston, D.L., 2001. The alteration box plot: A simple approach to understanding the relationship between alteration mineralogy and lithogeochemistry associated with volcanic-hosted massive sulfide deposits. Economic geology 96, 957-971.

Lassiter, J.C., Depaolo, D.J., Mahoney, J.J., 1995. Geochemistry of the Wrangellia Flood-Basalt Province - Implications for the Role of Continental and Oceanic Lithosphere in Flood-Basalt Genesis. The Jounal of Petrology 36, 983–1009.

Laurent, O., Martin, H., Moyen, J.F. and Doucelance, R., 2014. The diversity and evolution of late-Archean granitoids: Evidence for the onset of “modern-style” plate tectonics between 3.0 and 2.5 Ga. Lithos 205, 208-235.

.Le Bas, M.J., Le Maitre, R.W., Streckeisen, A., Zanettin, B., 1986. A chemical classification of volcanic rocks based on the total alkali-silica diagram. The Journal of Petrology 27, 745-750.

Liao, F.X., Chen, N.S., Santosh, M., Wang, Q.Y., Gong, S.L., He, C. and Mustafa, H.A., 2018. Paleoproterozoic Nb–enriched meta-gabbros in the Quanji Massif, NW China: Implications for assembly of the Columbia supercontinent. Geoscience Frontiers, 9, 577-590.

Ludwig, K.R., 2003. ISOPLOT 3.0: A Geochronological Toolkit for MicrosoftExcel. Berkeley Geochronology Center. Special, Publication No. 4.

Maaløe, S., 1982. Petrogenesis of Archaean Tonalites. Geol. Rundschau 71, 328–346.

Manikyamba, C., Kerrich, R., 2011. Geochemistry of alkaline basalts and associated high-mg basalts from the 2.7ga penakacherla terrane, dharwar craton, india: An archean depleted mantle-oib array. Precambrian Research 188, 104–122.

Manikyamba, C., Kerrich, R., 2012. Eastern Dharwar Craton, India: Continental lithosphere growth by accretion of diverse plume and arc terranes. Geoscience Frontiers 3, 225–240.

Manikyamba, C., Kerrich, R., Naqvi, S.M., Mohan, M.R., 2004a. Geochemical systematics of tholeiitic basalts from the 2.7 Ga Ramagiri-Hungund composite greenstone belt, Dharwar craton. Precambrian Research 134, 21–39.

Manikyamba, C., Naqvi, S.M., Mohan, M.R., Rao, T.G., 2004b. Gold mineralisation and alteration of Penakacherla schist belt, India, constraints on Archaean subduction and fluid processes. Ore Geology Reviews 24, 199–227.

Manikyamba, C., Naqvi, S.M., Subba Rao, D. V., Ram Mohan, M., Khanna, T.C., Rao, T.G., Reddy, G.L.N., 2005. Boninites from the Neoarchaean Gadwal Greenstone belt, Eastern Dharwar Craton, India: Implications for Archaean subduction processes. Earth and Planetary Science Letters 230, 65–83.

Manikyamba, C., Kerrich, R., Khanna, T.C., Keshav Krishna, A., Satyanarayanan, M., 2008. Geochemical systematics of komatiite-tholeiite and adakitic-arc basalt associations: The role of a mantle plume and convergent margin in formation of the Sandur Superterrane, Dharwar craton, India. Lithos 106, 155–172.

Manikyamba, C., Kerrich, R., Khanna, T.C., Satyanarayanan, M., Krishna, A.K., 2009. Enriched and depleted arc basalts, with Mg-andesites and adakites: A potential

paired arc-back-arc of the 2.6 Ga Hutti greenstone terrane, India. Geochimica et Cosmochimica Acta 73, 1711–1736.

Manikyamba, C., Kerrich, R., Polat, A., Raju, K., Satyanarayanan, M., Krishna, A.K., 2012. Arc picrite-potassic adakitic-shoshonitic volcanic association of the Neoarchean Sigegudda greenstone terrane, western Dharwar craton: Transition from arc wedge to lithosphere melting. Precambrian Research 212–213, 207–224.

Manikyamba, C., Kerrich, R., Polat, A., Saha, A., 2013. Geochemistry of two stratigraphically-related ultramafic (komatiite) layers from the Neoarchean Sigegudda greenstone terrane, Western Dharwar Craton, India: Evidence for compositional diversity in Archean mantle plumes. Lithos 177, 120–135.

Manikyamba, C., Ganguly, S., Saha, A., Santosh, M., Singh, M.R., Subba Rao, D.V., 2014a. Continental lithospheric evolution: constraints from the geochemistry of felsic volcanic rocks in the Dharwar Craton, India. Precambrian Research 95, 65-80.

Manikyamba, C., Saha, A., Santosh, M., Ganguly, S., Singh, M.R., Rao, D.S. and Lingadevaru, M., 2014b. Neoarchaean felsic volcanic rocks from the Shimoga greenstone belt, Dharwar Craton, India: geochemical fingerprints of crustal growth at an active continental margin. Precambrian Research 252, 1-21.

Manikyamba, C., Ganguly, S., Santosh, M., Singh, M.R. and Saha, A., 2014c. Arc-nascent back-arc signature in metabasalts from the Neoarchaean Jonnagiri greenstone terrane, Eastern Dharwar Craton, India. Geological Journal, 50, 651-669.

Manikyamba, C., Ganguly, S., Santosh, M., Saha, A., Chatterjee, A. and Khelen, A.C., 2015. Neoarchean arc–juvenile back-arc magmatism in eastern Dharwar Craton, India: geochemical fingerprints from the basalts of Kadiri greenstone belt. Precambrian Research 258, 1-23.

Manikyamba, C., Santosh, M., Kumar, B.C., Rambabu, S., Tang, L., Saha, A., Khelen, A.C., Ganguly, S., Singh, T.D., Rao, D.V.S., 2016. Zircon U-Pb geochronology, Lu-Hf isotope systematics, and geochemistry of bimodal volcanic rocks and associated granitoids from Kotri Belt, Central India: Implications for Neoarchean–Paleoproterozoic crustal growth. Gondwana Research 38, 313–333.

Manikyamba, C., Ganguly, S., Santosh, M., Subramanyam, K.S.V., 2017. Volcano-sedimentary and metallogenic records of the Dharwar greenstone terranes, India: Window to Archean plate tectonics, continent growth, and mineral endowment. Gondwana Research 50, 38–66.

Martin, H., 1986. Effect of steeper Archean geothermal gradient on geochemistry of subduction-zone magmas. Geology 14, 753–756.

McCulloch, M.T., Gamble, J.A., 1991. Geochemical and geodynamical constraints on subduction zone magmatism. Earth and Planetary Sciences Letters 102, 358–374.

McKenzie, D., O'Nions, R.K., 1995. The source regions of oceanic island basalts. Jounal of Petrology 36, 133–159.

Mehnert, K.R., 1973. Migmatites and the oriin of granitic rocks. 3rd ed. Elsevier, Amsterdam.

Moyen, J.F., 2011. The composite Archaean grey gneisses: Petrological significance, and evidence for a non-unique tectonic setting for Archaean crustal growth. Lithos 123, 21–36.

Moyen, J.F., Martin, H., 2012. Forty years of TTG research. Lithos 148, 312–336.

Moyen, J.F., Martin, H., Jayananda, M., Auvray, B., 2003. Late Archaean granites: A typology based on the Dharwar Craton (India). Precambrian Research 127, 103–123.

Moyen, J.F., Stevens, G., Kisters, A., 2006. Record of mid-Archaean subduction from metamorphism in the Barberton terrain, South Africa. Nature 442, 559–562.

Moyen, J.F., Laurent, O., 2018. Archaean tectonic systems: A view from igneous rocks. Lithos 302-303, 99-125.

Münker, C., 1998. Nb/Ta fractionation in a Cambrian arc/back arc system, New Zealand: source constraints and application of refined ICPMS techniques. Chemical Geology 144, 23–45.

Nair, R., Chacko, T., 2008. Role of oceanic plateaus in the initiation of subduction and origin of continental crust. Geology 36, 583–586.

Naqvi, S.M. 1983. Early Precambrian clastic metasediments of Dharwar greenstone belts: implications to SIMA-SIAL transformation process. In: S.M. Naqvi and

J.J.W. Rogers (Eds.), Precambrians of South India, Geol. Soc. India Mem. 4, 220-236.

Naqvi, S.M., Rogers, J.J.W. 1987. Precambrian Geology of India. Oxford University Press: New York; 1–223.

Naqvi, S.M., Sawkar, R.H., Subba Rao, D. V., Govil, P.K., Gnaneswar Rao, T., 1988. Geology, geochemistry and tectonic setting of Archaean greywackes from Karnataka nucleus, India. Precambrian Research 39, 193–216.

Niu, Y., 2012. Earth processes cause Zr–Hf and Nb–Ta fractionations, but why and how? RSC Advances 2, 3587–3591. Nutman, A.P., Chadwick, B., Ramakrishnan, M., Viswanatha, M.N., 1992. SHRIMP U-Pb ages of detrital zircon in Sargur supracrustal rocks in western Karnataka, southern India. Journal of the Geological Society of India 39, 367-374.

Nutman, A.P., McGregor, V., Friend, C.R.L., 1996. The Itsaq Gneiss Complex of southern West Greenland ; the world's most extensive record of early crustal evolution. Precambrian Research, 78, 1-39.

O'connor, J.T., 1965. A classification for quartz-rich igneous rocks based on feldspar ratios. US Geological Survey Professional Paper B 525, 79-84.

Páez, G.N., Ruiz, R., Guido, D.M., Jovic, S.M. and Schalamuk, I.B., 2010. The effects of K-metasomatism in the Bahía Laura Volcanic Complex, Deseado Massif, Argentina: petrologic and metallogenic consequences. Chemical Geology 273, 300-313.

Pearce, J.A., 2008. Geochemical fingerprinting of oceanic basalts with applications to ophiolite classification and the search for Archean oceanic crust. Lithos 100, 14–48.

Pearce, J.A. and Norry, M.J., 1979. Petrogenetic implications of Ti, Zr, Y, and Nb variations in volcanic rocks. Contributions to Mineralogy and Petrology 69, 33-47.

Pearce, J.A., Peate, D.W., 1995. Tectonic implications of the composi tion of volcanic arc magmas. Earth and Planetary Science Letters 23, 251–285.

Pearce, J.A., Stern, R.J., 2006. Origin of back-arc basin magmas: Trace element and isotope perspectives. Back-Arc Spreading Systems: Geological, Biological, Chemical, and Physical Interactions 63-86.

Pearce, J.A., Lippard, S.J. and Roberts, S., 1984. Characteristics and tectonic significance of supra-subduction zone ophiolites. Geological Society, London, Special Publications 16, 77-94.

Pearce, J.A., Thirlwall, M.F., Ingram, G., Murton, B.J., Arculus, R.J. and Van der Laan, S.R., 1992. 13. Isotopic evidence for the origin of boninites and related rocks drilled in the Izu-Bonin (Ogasawara) forearc, Leg 125. In Proc. Ocean Drilling Program, Scientific Results College Station Texas, 125, 237-261.

Pearce, J.A., Barker, P.F., Edwards, S.J., Parkinson, I.J., Leat, P.T., 2000. Geochemistry and tectonic significance of peridotites from the South Sandwich arc-basin system, South Atlantic. Contribution to Mineralogy and Petrology. 139, 36–53.

Pearce, J.A., Stern, R.J., Bloomer, S.H. and Fryer, P., 2005. Geochemical mapping of the Mariana arc-basin system: Implications for the nature and distribution of subduction components. Geochemistry, Geophysics, Geosystems 6, 1-27.

Peccerillo, A. and Taylor, S.R., 1976. Geochemistry of Eocene calc-alkaline volcanic rocks from the Kastamonu area, northern Turkey. Contributions to Mineralogy and Petrology 58, 63-81.

Perfit, M.R., Gust, D.A., Bence, A.E., Arculus, R.J., Taylor, S.R., 1980. Chemical characteristics of island-arc basalts: Implications for mantle sources. Chemical Geoology 30, 227–256.

Peucat, J.J., Mahabaleswar, B., Jayananda, M., 1993. Age of younger tonalitic magmatism and granulitic metamorphism in the South Indian transition zone (Krishnagiri area); comparison with older Peninsular gneisses from the Gorur–Hassan area. Journal of Metamorphic Geology 11, 879–888.

Peucat, J.J., Bouhallier, H., Fanning, C.M., Jayananda, M., 1995. Age of the Holenarsipur Greenstone Belt, Relationships with the Surrounding Gneisses (Karnataka, South India). The Journal of Geology 103, 701–710.

Peucat, J.J., Jayananda, M., Chardon, D., Capdevila, R., Fanning, C.M., Paquette, J.L., 2013. The lower crust of the Dharwar Craton, Southern India: Patchwork of

Archean granulitic domains. Precambrian Research 227, 4–28.

Polat, A., 2012. Growth of Archean continental crust in oceanic island arcs. Geology, 40, 83.

Polat, A., Kerrich, R., 2001. Geodynamic processes, continental growth, and mantle evolution recorded in late Archean greenstone belts of the southern Superior Province, Canada. Precambrian Research 112, 5–25.

Polat, A., Kerrich, R., 2002. Nd-isotope systematics of ~2.7 Ga adakites, magnesian andesites, and arc basalts, Superior Province: Evidence for shallow crustal recycling at Archean subduction zones. Earth and Planetary Science Letters 202, 345–360.

Polat, A., Münker, C., 2004. Hf-Nd isotope evidence for contemporaneous subduction processes in the source of late Archean arc lavas from the Superior Province, Canada. Chemical Geology 213, 403–429.

Polat, A., Kerrich, R., 2006. Reading the geochemical fingerprints of archean hot subduction volcanic rocks: Evidence for accretion and crustal recycling in a mobile tectonic regime. Geophysical Monograph. Series. 164, 189–213.

Polat, A., Kerrich, R., Wyman, D.A., 1999. Geochemical diversity in oceanic komatiites and basalts from the late Archean Wawa greenstone belts, Superior Province, Canada: Trace element and Nd isotope evidence for a heterogeneous mantle. Precambrian Research 94, 139–173.

Polat, A., Hofmann, A.W., Rosing, M.T., 2002. Boninite-like volcanic rocks in the 3 . 7 – 3 . 8 Ga Isua greenstone belt , West Greenland : geochemical evidence for intra-oceanic subduction zone processes in the early Earth. Chemical Geology 184, 231–254.

Prigent, C., Guillot, S., Agard, P., Lemarchand, D., Soret, M., Ulrich, M., 2018. Transfer of subduction fluids into the deforming mantle wedge during nascent subduction: Evidence from trace elements and boron isotopes (Semail ophiolite, Oman). Earth and Planetary Science Letters 484, 213–228.

Radhakrishna, B.P., 1983. Archean granite–greenstone terrain of the South Indian shield. Geological Society of India, Memoir 4, 46.

Ramakrishnan, M., and Harinadha Babu, P., 1981, Western Ghats Belt, Swami Nath, J., and Ramakrishnan, M., Eds., Early precambrian supracrustals of Southern Karnataka: Calcutta, Geological Survey of India, 147–161.

Ramakrishnan, M., Vaidyanadhan, R. 2010. Geology of India.Volume-1. Geological Society of India, Bangalore.

Rajesh, H.M. and Santosh, M., 2004. Charnockitic magmatism in southern India. Journal of Earth System Science 113, 565-585.

Rajesh, H.M., Belyanin, G.A. and Van Reenen, D.D., 2018. Three tier transition of Neoarchean TTG-sanukitoid magmatism in the Beit Bridge Complex, Southern Africa. Lithos 296, 431-451.

Rapp, R.P., Watson, E.B. and Miller, C.F., 1991. Partial melting of amphibolite/eclogite and the origin of Archean trondhjemites and tonalites. Precambrian Research, 51, 1-25.

Ray, J., Saha, A., Ganguly, S., Balaram, V., Krishna, A.K. and Hazra, S., 2011. Geochemistry and petrogenesis of Neoproterozoic Mylliem granitoids, Meghalaya Plateau, northeastern India. Journal of Earth System Science 120, 459.

Reichow, M.K., Saunders, A.D., White, R. V., Al'Mukhamedov, A.I., Medvedev, A.Y., 2005. Geochemistry and petrogenesis of basalts from the West Siberian Basin: An extension of the Permo-Triassic Siberian Traps, Russia. Lithos 79, 425–452.

Rollinson, H.R., 2014. Using geochemical data: evaluation, presentation, interpretation. Routledge.

Rudnick, R.L., Fountain, D.M., 1995. Nature and composition of the continental crust: a lower crustal perspective. Reviews of Geophysics 33, 267–309.

Rudnick, R.L., Gao, S., 2003. Composition of the continental crust. In: Rudnick, R.L., Holland, H.D., Turekian, K.K. (Eds.), The Crust. : Treatise on the Geochemistry, Elsevier-Pergamon, Oxford 3, 1–64

Sajona, F.G., Maury, R.C., Bellon, H., Cotten, J., Defant, M.J., Pubellier, M., 1993. Initiation of subduction and the generation of slab melts in western and eastern

Mindanao, Philippines. Geology 21, 1007–1010.

Sajona, F.G., Maury, R.C., Bellon, H., Cotten, J., Defant, M., 1996. High field strength element enrichment of Pliocene-Pleistocene island arc basalts, Zamboanga Peninsula, Western Mindanao (Philippines). Journal of Petrology 37, 693–726.

Sampat Iyengar, P., 1910. The geology of the southern portion of Hassan district. Mysore Geological Department 11, 77-95.

Santosh, M., Li, S.S., 2018. Anorthosites from an Archean continental arc in the Dharwar Craton, southern India: Implications for terrane assembly and cratonization. Precambrian Research 308, 126–147.

Saunders, A.D., Tarney, J., Weaver, S.D., 1980. Transverse geochemical variations across the Antarctic Peninsula: Implications for the genesis of calc-alkaline magmas. Earth and Planetary Science Letters 46, 344–360.

Shang, C.K., Satir, M., Nsifa, E.N., Liégeois, J.P., Siebel, W. and Taubald, H., 2007. Archaean high-K granitoids produced by remelting of earlier Tonalite–Trondhjemite–Granodiorite (TTG) in the Sangmelima region of the Ntem complex of the Congo craton, southern Cameroon. International Journal of Earth Sciences 96, 817-841.

Shellnutt, J.G., Bhat, G.M., Wang, K.L., Brookfield, M.E., Jahn, B.M., Dostal, J., 2014. Petrogenesis of the flood basalts from the Early Permian Panjal Traps, Kashmir, India: Geochemical evidence for shallow melting of the mantle. Lithos 204, 159–171.

Singh, M.R., Manikyamba, C., Ganguly, S., Ray, J., Santosh, M., Singh, T.D. and Kumar, B.C., 2017. Paleoproterozoic arc basalt-boninite-high magnesian andesite-Nb enriched basalt association from the Malangtoli volcanic suite, Singhbhum Craton, eastern India: Geochemical record for subduction initiation to arc maturation continuum. Journal of Asian Earth Sciences 134, 191-206.

Singh, S.P., Subramanyam, K.S.V., Manikyamba, C., Santosh, M., Singh, M.R., and Kumar, B.C., 2018. Geochemical systematics of the Mauranipur-Babina greenstone belt, Bundelkhand Craton, Central India: Insights on Neoarchean mantle plume-arc accretion and crustal evolution. Geoscience Frontiers 9, 769-788.

Smith, T.E., Huang, C.H., Walawender, M.J., Cheung, P., Wheeler, C., 1983. The gabbroic rocks of the Peninsular ranges batholith, Southern California: cumulate rocks associated with calc-alkalic basalts and andesites. Journal of Volcanology and Geothermal Research 18, 249–278.

Smithies, R.H., Champion, D.C. and Cassidy, K.F., 2003. Formation of Earth's early Archaean continental crust. Precambrian Research 127, 89-101.

Smithies, R.H., Van Kranendonk, M.J., Champion, D.C., 2005. It started with a plume - Early Archaean basaltic proto-continental crust. Earth and Planetary Science Letters 238, 284–297.

Smithies, R.H., Champion, D.C. and Van Kranendonk, M.J., 2009. Formation of Paleoarchean continental crust through infracrustal melting of enriched basalt. Earth and Planetary Science Letters 281, 298-306.

Song, X.Y., Zhou, M.F., Keays, R.R., Cao, Z.M., Sun, M., Qi, L., 2006. Geochemistry of the Emeishan flood basalts at Yangliuping, Sichuan, SW China: Implications for sulfide FFsegregation. Contribution to Mineralogy and Petrology 152, 53–74.

Sreeramachandra Rao, K., 1970. Preliminary exploration for magnetite quartzite deposits in the Kodachadri region, West Coast Iron Ore Project. Shimoga district, Mysore State. Geological Suevey of India Report.

Streckeisen, A., 1979. Classification and nomenclature of volcanic rocks, lamprophyres, carbonatites, and melilitic rocks: Recommendations and suggestions of the IUGS Subcommission on the Systematics of Igneous Rocks. Geology *7*, 331-335.

Sun, S., McDonough, W.F., 1989. Chemical and isotopic systematics of oceanic basalts: implications for mantle composition and processes. Geological Society, London, Special Publications 42, 313-345.

Swami Nath, J., Ramakrishnan, M. (Eds.), 1981. Early Precambrian Supracrustals of Southern Karnataka. Geological Survey of India 112, 79-81.

Tang, L., Santosh, M., 2018. Neoarchean granite-greenstone belts and related ore mineralization in the North China Craton: An overview. Geoscience Frontiers 8,

751-768.

Taylor, P.N., Chadwick, B., Moorbath, S., Ramakrishnan, M., Viswanatha, M.N., 1984. Petrography, chemistry and isotopic ages of Peninsular Gneiss, Dharwar acid volcanic rocks and the Chitradurga granite with special reference to the late Archean evolution of the Karnataka craton, southern India. Precambrian Research 23, 349–375.

Thieblemont, D., Tegyey, M., 1994. Geochemical discrimination of differentiated magmatic rocks attesting for the variable origin and tectonic setting of calc-alkaline magmas. Comptes Rendus De Academie Des Sciences Series II 319, 87-94

Thompson, A.B., Connolly, J.A.D., 1995. Melting of the continental crust: Some thermal and petrological constraints on anatexis in continental collision zones and other tectonic settings. Journal of Geophysical. Research: Solid Earth 100, 15565–15579.

Tushipokla, Jayananda, M., 2013. Geochemical constraints on komatiite volcanism from Sargur Group Nagamangala greenstone belt, western Dharwar craton, southern India: Implications for Mesoarchean mantle evolution and continental growth. Geoscience Frontiers 4, 321–340.

Van Kranendonk, M.J., Smithies, R.H., Hickman, A.H., Champion, D.C., 2007. Chapter 4.1 Paleoarchean Development of a Continental Nucleus: the East Pilbara Terrane of the Pilbara Craton, Western Australia. Developments in Precambrian Geology 15, 307–337.

Wang, X.C., Li, X.H., Li, W.X. and Li, Z.X., 2007. Ca. 825 Ma komatiitic basalts in South China: First evidence for> 1500 C mantle melts by a Rodinian mantle plume. Geology 35, 1103-1106.

Wang, Y., Fan, W., Cawood, P.A. and Li, S., 2008. Sr–Nd–Pb isotopic constraints on multiple mantle domains for Mesozoic mafic rocks beneath the South China Block hinterland. Lithos 106, 297-308.

Wang, S., Zhang, D., Wu, G., Vatuva, A., Di, Y., Yan, P., Feng, H. and Ma, S., 2017. Late Paleozoic to Mesozoic extension in southwestern Fujian Province, South China: Geochemical, geochronological and Hf isotopic constraints from basic-intermediate dykes. Geoscience Frontiers 8, 529-540.

Wilson, M., and Davidson, J.P., 1984. The relative roles of crust and upper mantle in the generation of oceanic island arc magmas. Philosophical Transactions of the Royal Society A, London 310, 661-674.

Winchester, J.A. and Floyd, P.A., 1977. Geochemical discrimination of different magma series and their differentiation products using immobile elements. Chemical geology 20, 25-343.

Woodhead, J., Eggins, S., Gamble, J., 1993. High field strength and transition element systematics in island arc and back-arc basin basalts: evidence for multi-phase melt extraction and a depleted mantle wedge. Earth and Planetary Science Letters 114, 491-504.

Wyman, D., Kerrich, R., 2009. Plume and arc magmatism in the Abitibi subprovince: Implications for the origin of Archean continental lithospheric mantle. Precambrian Research 168, 4–22.

Wyman, D.A., Kerrich, R., Groves, D.I., 1999. Lode Gold Deposits and Archean Mantle Plume–Island Arc Interaction, Abitibi Subprovince, Canada. The Journal of Geololgy 107, 715–725.

Wyman, D.A., Ayer, J.A., Devaney, J.R., 2000. Niobium-enriched basalts from the Wabigoon subprovince, Canada: Evidence for adakitic metasomatism above an Archean subduction zone. Earth and Planetary Science Letters 179, 21–30.

Xiong, X.L., Adam, J. and Green, T.H., 2005. Rutile stability and rutile/melt HFSE partitioning during partial melting of hydrous basalt: implications for TTG genesis. Chemical Geology 218, 339-359.

Xiong, X.L., Liu, X.C., Zhu, Z.M., Li, Y., Xiao, W.S., Song, M.S., Zhang, S., Wu, J.H., 2011. Adakitic rocks and destruction of the North China Craton: Evidence from experimental petrology and geochemistry. Science China Earth Sciences 54, 858–870.

Xu, Y.G., Ma, J.L., Frey, F.A., Feigenson, M.D., Liu, J.F., 2005. Role of lithosphere-asthenosphere interaction in the genesis of Quaternary alkali and tholeiitic basalts

from Datong, western North China Craton. Chemical Geology 224, 247–271.

Yang, J., Godard, G., Kienast, J.R., Lu, Y., Sun, J., 1993. Ultrahigh pressure 60 kbar magnesite-bearing garnet peridotites from northeastern Jiangsu, China. Journal of Geology 101, 541–554.

Yaxley, G.M., 2000. Experimental study of the phase and melting relations of homogeneous basalt + peridotite mixtures and implications for the petrogenesis of flood basalts. Contribution to Mineralogy and Petrology 139, 326–338.

Zhai, M., 2014. Multi-stage crustal growth and cratonization of the North China Craton. Geoscience Frontiers 5, 457–469.

Zhang, R.Y., Liou, J.G., Cong, B.,1994. Petrogenesis of garnet bearing ultramafic rocks and associated eclogites in the Sulu ultrahigh-P metamorphic terrane, eastern China. Journal of Metamorphic Geology 12, 169–186.

Zhang, R.Y., Hirajima, T., Banno, S., Cong, B., Liou, J.G., 1995. Petrology of ultrahigh-pressure metamorphic rocks in southern Sulu region, eastern China. Journal of Metamorphic Geology 13, 659–675.

Zhang, H., Niu, H., Sato, H., Yu, X., Shan, Q., Zhang, B., Ito, J., Nagao, T., 2005. Late Paleozoic adakites and Nb-enriched basalts from northern Xinjiang, northwest China: Evidence for the southward subduction of the Paleo-Asian Oceanic Plate. Island Arc 14, 55–68.

Zhao, J., Zhou, M., 2007. Neoproterozoic Adakitic Plutons and Arc Magmatism along the Western Margin of the Yangtze Block, South China. The Jounal of Geology 115, 675–689.

Table 1 Lithostratigraphy of Western Ghat belt (after Ramakrishnan and Harinadha Babu, 1981)

		Laterite cover
	Deccan trap	Rhyodacite and granophyre
		Basic and ultrabasic intrusives
		Disconformity
Dharwar Super Group	Narsiparvata Formation	Acid volcanics, tuffs, ironstone, chloritic phyllites
	Kodachatri Formation	Algoma type BIFs (oxide and silicate facies), schist with rare dolomitic limestone
	Kudremukh Formation	Amygdular metavolcanics, greenstone, metagabbro, ultramafics, Cross bedded quartzite, metabasalt, BIFs.
	Walkunje Formation	Oligomictic conglomerate, cross bedded quartzite, garnetiferous schist
		Deformed angular unconformity
		Peninsular gneisses with TTG plutons (>3000 Ma)
		Tectonic contact
	Sargur Group	Quartzite,amphibolite,ironstone,garnetiferous mica schist,

(3100-3300 Ma)

silliminite-garnet schist, calc silicate and ultramafics

6

Table 2: Zircon U-Pb analytical data of Kudremukh-Agumbe greenstone belt

Spot No.	Pb_T ppm	U ppm	Th ppm	Th/U	$^{207}Pb/^{206}Pb \pm 1s$		$^{207}Pb/^{235}U \pm 1s$		$^{206}Pb/^{238}U \pm 1s$		$^{207}Pb/^{206}Pb$ age (Ma)		$^{207}Pb/^{235}U$ age (Ma)		$^{206}Pb/^{238}U$ age (Ma)		Concordance
L20 (TTG)																	
L-20-03	572	322	760	0.42	0.2255	0.0042	17.5876	0.3219	0.5622	0.0052	3020	30	2967	18	2876	21	96%
L-20-04	606	497	839	0.59	0.2325	0.0038	16.8532	0.2934	0.5225	0.0052	3069	27	2927	17	2710	22	92%
L-20-05	716	578	1158	0.50	0.2090	0.0031	13.4013	0.2029	0.4625	0.0034	2898	24	2708	14	2450	15	90%
L-20-06	589	573	878	0.65	0.2122	0.0031	14.6691	0.2517	0.4981	0.0048	2922	23	2794	16	2606	21	93%
L-20-07	558	574	851	0.67	0.2144	0.0033	14.8643	0.3392	0.4980	0.0074	2939	25	2807	22	2605	32	92%
L-20-08	707	447	862	0.52	0.2231	0.0037	18.7562	0.3270	0.6070	0.0052	3003	28	3029	17	3058	21	99%
L-20-09	606	896	922	0.97	0.1977	0.0033	13.1444	0.2273	0.4802	0.0042	2807	27	2690	16	2528	18	93%
L-20-10	506	607	648	0.94	0.2160	0.0037	16.5793	0.4139	0.5492	0.0076	2951	32	2911	24	2822	32	96%
L-20-11	730	495	1028	0.48	0.2107	0.0032	15.6536	0.2409	0.5362	0.0042	2911	24	2856	15	2768	18	96%
L-20-12	593	373	802	0.46	0.2221	0.0034	17.5658	0.3477	0.5693	0.0072	2998	25	2966	19	2905	30	97%
L-20-13	662	639	764	0.84	0.2296	0.0039	19.4276	0.3663	0.6094	0.0060	3049	27	3063	18	3068	24	99%
L-20-14	588	543	947	0.57	0.2057	0.0039	13.1218	0.2508	0.4598	0.0037	2872	31	2688	18	2439	16	90%
L-20-15	166	113	189	0.60	0.241	0.004	21.3863	0.433	0.639	0.006	3127	30	3156	20	3187	25	99%

					2	7		2	4	3							
L-20-16	678	353	980	0.36	0.2199	0.0036	16.2067	0.2740	0.5313	0.0039	2980	27	2889	16	2747	17	94%
L-20-17	652	441	902	0.49	0.2214	0.0035	16.5847	0.2598	0.5404	0.0036	2990	26	2911	15	2785	15	95%
L-20-18	697	533	956	0.56	0.2242	0.0034	16.7952	0.2610	0.5406	0.0040	3011	25	2923	15	2786	17	95%
L-20-19	597	503	868	0.58	0.2165	0.0035	15.3045	0.2485	0.5103	0.0038	2955	26	2834	16	2658	16	93%
L-20-20	486	569	555	1.02	0.2319	0.0042	19.8266	0.4142	0.6163	0.0071	3065	29	3083	20	3095	29	99%
L-20-21	683	569	877	0.65	0.2119	0.0043	15.9634	0.3531	0.5432	0.0045	2920	33	2875	21	2797	19	97%
L-20-22	715	555	1070	0.52	0.2147	0.0034	14.9813	0.3048	0.5029	0.0061	2942	26	2814	19	2626	26	93%
L-20-23	790	705	1031	0.68	0.2222	0.0033	17.3026	0.3022	0.5626	0.0062	2998	24	2952	17	2878	26	97%
L-20-26	669	737	968	0.76	0.2149	0.0038	15.0505	0.2800	0.5064	0.0045	2943	29	2818	18	2641	19	93%
L-20-27	652	653	911	0.72	0.2187	0.0039	16.1186	0.2986	0.5331	0.0046	2971	34	2884	18	2755	20	95%
L-20-28	657	475	946	0.50	0.2181	0.0035	15.9477	0.2729	0.5286	0.0044	2969	27	2874	16	2736	19	95%
L-20-29	568	558	861	0.65	0.2116	0.0034	14.4382	0.2823	0.4913	0.0045	2918	26	2779	19	2576	19	92%
L-20-30	587	545	771	0.71	0.2227	0.0033	17.2226	0.2830	0.5584	0.0047	3011	24	2947	16	2860	20	96%
L29 (Granite)																	
L-29-01	671	282	1015	0.28	0.2280	0.0036	16.8784	0.2829	0.5344	0.0046	3039	26	2928	16	2760	20	94%
L-29-02	622	606	1081	0.56	0.2309	0.0041	15.9379	0.4492	0.4983	0.0115	3058	29	2873	27	2606	50	90%

L-29-03	643	257	1032	0.25	0.2229	0.0041	15.4542	0.3410	0.4996	0.0066	3002	29	2844	21	2612	28	91%
L-29-04	434	367	679	0.54	0.2214	0.0036	16.0268	0.2842	0.5219	0.0048	2991	27	2878	17	2707	20	93%
L-29-14	388	172	577	0.30	0.2445	0.0040	17.8371	0.3800	0.5234	0.0064	3150	26	2981	21	2714	27	90%
L-29-24	559	227	810	0.28	0.2154	0.0031	16.4339	0.2337	0.5508	0.0043	2947	23	2902	14	2829	18	97%
L-29-22	350	570	464	1.23	0.2687	0.0043	20.8412	0.3356	0.5598	0.0042	3298	25	3131	16	2866	18	91%
L-29-23	629	387	871	0.44	0.2319	0.0033	18.3905	0.2912	0.5722	0.0055	3065	23	3010	15	2917	23	96%
L-29-10	747	240	967	0.25	0.2065	0.0037	16.4043	0.3075	0.5725	0.0051	2880	29	2901	18	2918	21	99%
L-29-27	488	591	647	0.91	0.2157	0.0036	17.4430	0.2937	0.5842	0.0052	2950	27	2960	16	2966	21	99%
L-29-13	829	230	1079	0.21	0.2150	0.0032	17.5180	0.2980	0.5869	0.0062	2944	24	2964	16	2977	25	99%
L-29-12	486	806	630	1.28	0.2912	0.0045	23.7462	0.3951	0.5876	0.0055	3424	24	3258	16	2980	22	91%
L-29-17	365	521	475	1.10	0.2483	0.0037	20.5440	0.3192	0.5961	0.0045	3174	24	3117	15	3014	18	96%
L-29-08	528	371	735	0.50	0.2325	0.0043	19.2543	0.3835	0.5978	0.0069	3069	30	3055	19	3021	28	98%
L-29-26	299	56	408	0.14	0.2155	0.0036	17.8886	0.3218	0.5996	0.0063	2947	28	2984	17	3028	25	98%
L-29-28	386	295	517	0.57	0.2325	0.0036	19.3098	0.3265	0.5996	0.0065	3069	19	3057	16	3028	26	99%
L-29-25	435	779	571	1.37	0.2232	0.0035	18.5679	0.3242	0.5996	0.0055	3006	25	3020	17	3028	22	99%
L-29-16	577	355	774	0.46	0.2238	0.0032	18.6508	0.2801	0.6006	0.0050	3008	23	3024	15	3032	20	99%
L-29-20	417	226	553	0.41	0.241	0.004	20.5885	0.396	0.615	0.006	3128	29	3119	19	3092	25	99%

					2	4		7	5	2								
L-29-19	801	196	1038	0.19	0.2304	0.0039	20.0138	0.400 07	0.6256	0.0073	3055	28	3092	19	3132	29		98%
L-29-15	644	125	821	0.15	0.2399	0.0034	21.2349	0.3468	0.6373	0.0063	3119	23	3149	16	3178	25		99%
L-29-09	585	272	768	0.35	0.2298	0.0045	20.3394	0.4178	0.6381	0.0070	3051	32	3108	20	3181	28		97%
L-29-29	604	191	759	0.25	0.2351	0.0034	20.8677	0.3409	0.6400	0.0065	3087	22	3132	16	3189	26		98%
L-29-07	755	221	926	0.24	0.2329	0.0038	21.5773	0.3812	0.6682	0.0065	3072	26	3165	17	3299	25		95%
L-29-11	553	257	669	0.38	0.2350	0.0039	21.8167	0.3884	0.6688	0.0065	3087	26	3176	17	3301	25		96%
L-29-05	649	140	795	0.18	0.2327	0.0035	21.9768	0.3802	0.6808	0.0071	3072	24	3183	17	3347	27		94%
L-31(Basalt)																		
L-31-01	124	286	113	0.40	0.1187	0.0025	6.0472	0.1337	0.3644	0.0041	1939	37	1983	19	2003	20		98%
L-31-06	303	517	133	0.26	0.1636	0.0032	11.0393	0.2190	0.4843	0.0045	2494	32	2526	19	2546	20		99%
L-31-07	341	568	143	0.25	0.1644	0.0029	11.3667	0.2115	0.4959	0.0047	2502	30	2554	17	2596	20		98%
L-31-10	63	210	103	0.49	0.0871	0.0018	3.0224	0.0685	0.2498	0.0031	1362	41	1413	17	1437	16		98%
L23 (Dyke)																		
L-23-01	442	574	798	0.72	0.1641	0.0029	9.6012	0.1721	0.4218	0.0031	2498	30	2397	17	2269	14		94%
L-23-02	175	16	510	0.03	0.1610	0.0033	6.7704	0.1504	0.3028	0.0032	2466	36	2082	20	1705	16		80%
L-23-03	228	44	489	0.09	0.163	0.003	9.3409	0.193	0.412	0.003	2492	35	2372	19	2224	16		93%

					5	4		6	0	5								
L-23-04	458	32	1069	0.03	0.1600	0.0029	8.5139	0.1500	0.3839	0.0027	2457	31	2287	16	2095	13	91%
L-23-05	236	239	434	0.55	0.1653	0.0028	9.9629	0.1750	0.4349	0.0035	2511	28	2431	16	2328	16	95%
L-23-06	122	30	266	0.11	0.1608	0.0027	8.9742	0.1610	0.4027	0.0034	2465	30	2335	16	2182	16	93%
L-23-07	159	224	284	0.79	0.1606	0.0028	9.4057	0.1668	0.4233	0.0034	2461	30	2378	16	2275	15	95%
L-23-08	202	24	481	0.05	0.1542	0.0029	8.0826	0.1568	0.3787	0.0031	2392	32	2240	18	2070	15	92%
L-23-09	286	368	521	0.71	0.1586	0.0030	9.2541	0.1760	0.4215	0.0030	2440	31	2363	18	2267	14	95%
L-23-10	396	138	738	0.19	0.1591	0.0026	10.2252	0.2290	0.4636	0.0072	2446	28	2455	21	2456	32	99%
L-23-11	314	461	558	0.83	0.1570	0.0025	9.4072	0.1535	0.4332	0.0036	2433	27	2379	15	2320	16	97%
L-23-12	790	112	1595	0.07	0.1561	0.0024	9.3490	0.1463	0.4325	0.0032	2414	26	2373	14	2317	14	97%
L-23-13	258	294	489	0.60	0.1566	0.0026	9.0479	0.1582	0.4172	0.0037	2419	28	2343	16	2248	17	95%
L-23-14	324	411	676	0.61	0.1544	0.0030	8.2023	0.1659	0.3841	0.0043	2395	32	2254	18	2095	20	92%
L-23-15	688	416	1756	0.24	0.1539	0.0029	7.7099	0.1947	0.3616	0.0068	2390	31	2198	23	1990	32	90%
L-23-16	774	58	1597	0.04	0.1562	0.0026	9.3310	0.1695	0.4310	0.0042	2417	28	2371	17	2310	19	97%
L-23-17	182	194	371	0.52	0.1626	0.0026	8.7365	0.1419	0.3878	0.0027	2483	27	2311	15	2113	12	91%
L-23-18	195	25	420	0.06	0.1570	0.0025	8.8867	0.1412	0.4088	0.0032	2424	26	2326	15	2210	15	94%
L-23-19	123	149	254	0.58	0.1595	0.0028	8.2479	0.1451	0.3736	0.0030	2450	30	2259	16	2046	14	90%
L-23-	48	80	81	0.	0.1	0.0	9.69	0.1	0.4	0.0	24	2	24	1	23	1	95%

20	1	4	6	98	629	028	42	685	296	035	87	9	06	6	04	6	
L-23-21	542	55	1196	0.05	0.1599	0.0031	9.07755	0.1900	0.4093	0.0047	2454	32	2346	19	2212	21	94%
L-23-22	215	206	388	0.53	0.1661	0.0031	10.1591	0.2018	0.4412	0.0043	2518	32	2449	18	2356	19	96%
L-23-23	514	290	997	0.29	0.1646	0.0027	9.77769	0.1574	0.4288	0.0031	2506	27	2414	15	2300	14	95%
L-23-24	440	208	939	0.22	0.1620	0.0024	9.04665	0.1391	0.4034	0.0033	2477	24	2343	14	2184	15	93%
L-23-25	253	299	509	0.59	0.1580	0.0024	8.49913	0.1334	0.3885	0.0030	2435	25	2285	14	2116	14	92%
L-23-28	377	451	706	0.64	0.1605	0.0025	9.21753	0.1477	0.4153	0.0033	2461	25	2360	15	2239	15	94%
L-23-29	785	61	1572	0.04	0.1603	0.0022	9.80990	0.1538	0.4426	0.0043	2458	25	2417	15	2362	19	97%
L-23-30	155	32	311	0.10	0.1603	0.0025	9.55585	0.1606	0.4309	0.0040	2459	27	2393	16	2310	18	96%

7

8

Table 3: Major and trace element geochemistry of granites from Kudremukh-Agumbe greenstone belt

	L16/4	L16/5	L16/6	L29/0	L29/1	L29/2	L29/3	L29/4	L29/5	L29/6
wt.%										
SiO_2	69.72	65.60	69.22	72.16	70.45	73.96	74.57	77.14	74.10	74.76
TiO_2	0.09	0.15	0.09	0.09	0.02	0.10	0.01	0.01	0.12	0.11
Al_2O_3	15.97	16.99	15.80	13.94	15.93	13.88	15.03	12.10	14.56	15.05
Fe_2O_3	1.44	1.44	1.14	1.42	0.58	1.34	0.55	0.64	1.34	1.14
MnO	0.01	0.01	0.01	0.01	0.00	0.01	0.02	0.00	0.01	0.01
MgO	0.21	0.25	0.20	0.21	0.11	0.25	0.12	0.09	0.30	0.29
CaO	1.26	1.62	1.30	0.87	1.05	0.68	1.07	0.52	0.68	0.61
Na_2O	6.03	8.41	6.41	5.28	6.78	4.10	3.78	3.42	3.92	3.48
K_2O	2.53	2.60	2.65	4.19	3.84	4.67	4.12	4.45	4.93	5.20
P_2O_5	0.05	0.04	0.03	0.02	0.02	0.02	0.01	0.02	0.02	0.02
LOI	0.75	1.98	0.91	0.9	0.63	1.73	0.62	0.4	1.3	1.08
Total	98.06	99.09	97.76	99.09	99.41	100.74	99.90	98.79	101.28	101.75
Mg#	13.95	16.17	16.32	14.12	17.41	17.17	19.52	13.52	19.92	22.04
ppm										
Cr	127	124	133	150	109	123	97	169	131	110
Co	1.91	2.17	1.69	1.86	2.02	1.27	1.39	1.23	2.19	2.08
Ni	6.51	6.69	6.87	6.27	6.45	7.93	6.74	6.47	7.96	7.66
Rb	66	26	83	168	390	114	173	179	306	279
Sr	509	495	504	172	159	197	238	150	173	192
Cs	4.47	2.98	4.67	15.41	17.95	6.97	5.72	10.11	19.13	19.43
Ba	590	81	479	303	516	228	546	433	569	704
Sc	2.03	2.21	1.99	1.97	3.10	1.18	1.32	1.55	3.00	3.17
V	11.34	10.57	8.49	7.23	8.45	3.52	5.52	3.58	6.81	5.66
Ta	1.97	0.74	2.50	2.13	4.37	11.75	6.80	9.05	6.65	2.65
Nb	5.70	4.59	7.13	8.30	13.23	9.48	6.08	9.26	14.97	11.68
Zr	304	310	331	421	179	346	161	119	216	63
Hf	3.30	3.77	3.59	3.95	3.52	2.89	1.46	1.38	2.68	0.85
Th	5.50	12.13	9.73	12.63	23.36	7.61	4.50	5.38	14.46	5.43
U	0.75	0.42	0.90	0.68	0.75	1.31	0.73	0.59	0.62	0.43
Y	10.49	8.58	7.63	61.21	114.08	49.29	26.07	22.51	82.73	28.18

La	13.26	27.43	14.86	21.94	41.10	11.81	7.92	8.92	25.18	8.29
Ce	27.13	56.40	30.32	47.68	90.08	25.03	16.45	19.97	55.23	18.32
Pr	3.39	6.96	3.81	5.97	11.25	3.19	2.13	2.48	6.96	2.30
Nd	12.17	23.95	13.28	20.35	38.38	11.18	7.33	8.68	23.70	8.03
Sm	2.56	4.37	2.68	5.45	9.76	3.36	2.03	2.37	6.14	2.13
Eu	0.89	0.97	0.95	0.88	1.18	0.76	0.68	0.66	1.04	0.87
Gd	2.11	2.88	1.91	5.20	9.33	3.48	2.04	2.22	6.21	2.20
Tb	0.34	0.39	0.29	1.23	2.19	0.90	0.53	0.50	1.49	0.54
Dy	1.59	1.54	1.23	7.45	13.14	5.74	3.12	2.81	9.51	3.37
Ho	0.32	0.29	0.25	1.75	3.16	1.37	0.73	0.65	2.28	0.80
Er	0.78	0.64	0.59	5.04	9.33	4.04	2.13	1.83	6.70	2.33
Tm	0.13	0.09	0.08	0.85	1.46	0.70	0.35	0.31	1.09	0.40
Yb	0.80	0.58	0.59	5.87	9.25	4.69	2.40	2.14	7.08	2.68
Lu	0.11	0.08	0.08	0.82	1.29	0.65	0.33	0.30	0.99	0.37
Cu	1.18	1.58	1.39	1.26	1.13	2.12	1.84	1.16	1.22	1.44
Pb	23	22	46	27	27	47	26	23	28	32
Zn	32	35	35	33	35	26	17	18	32	27
Ga	18	21	19	18	18	22	16	13	17	15
Total REE	65.59	126.56	70.92	130.46	240.90	76.90	48.19	53.85	153.59	52.62
Na_2O+K_2O	8.56	11.01	9.06	9.47	10.62	8.77	7.90	7.87	8.85	8.68
K_2O/Na_2O	0.42	0.31	0.41	0.79	0.57	1.14	1.09	1.30	1.26	1.49
A/CNK	0.97	0.82	0.93	0.94	0.93	1.06	1.19	1.06	1.12	1.21
A/NK	1.13	0.95	1.08	1.05	1.04	1.18	1.41	1.16	1.24	1.33
Fe*	0.86	0.84	0.84	0.86	0.83	0.83	0.80	0.86	0.80	0.78
FeO	1.30	1.30	1.03	1.28	0.52	1.21	0.49	0.58	1.21	1.03
$(La/Yb)_N$	11.82	33.77	17.99	2.68	3.19	1.81	2.36	2.99	2.55	2.22
Eu/Eu*	1.17	0.83	1.28	0.50	0.37	0.67	0.85	0.87	0.51	0.76
$(Gd/Yb)_N$	2.17	4.08	2.67	0.73	0.83	0.61	0.70	0.86	0.73	0.68
Sr/Y	48.50	57.68	66.07	2.82	1.39	4.01	9.14	6.66	2.09	6.81
Nb/Zr	0.02	0.01	0.02	0.02	0.07	0.03	0.04	0.08	0.07	0.19

10

11

Research Highlights:

- Kudremukh-Agumbe greenstone belt situated along the northwestern margin of western Dharwar Craton.
- ~2.49-2.48 Ga mafic volcanism and dykes associated with ~3.06-2.94 Ga TTG and granites.
- TTGs derived from high pressure melting of mafic crust and granites are the fractional crystalization products of TTG melts
- Fluid-fluxed metasomatism and melt-fluxed hybridization in a mantle wedge produced metabasalts in a subduction zone environment

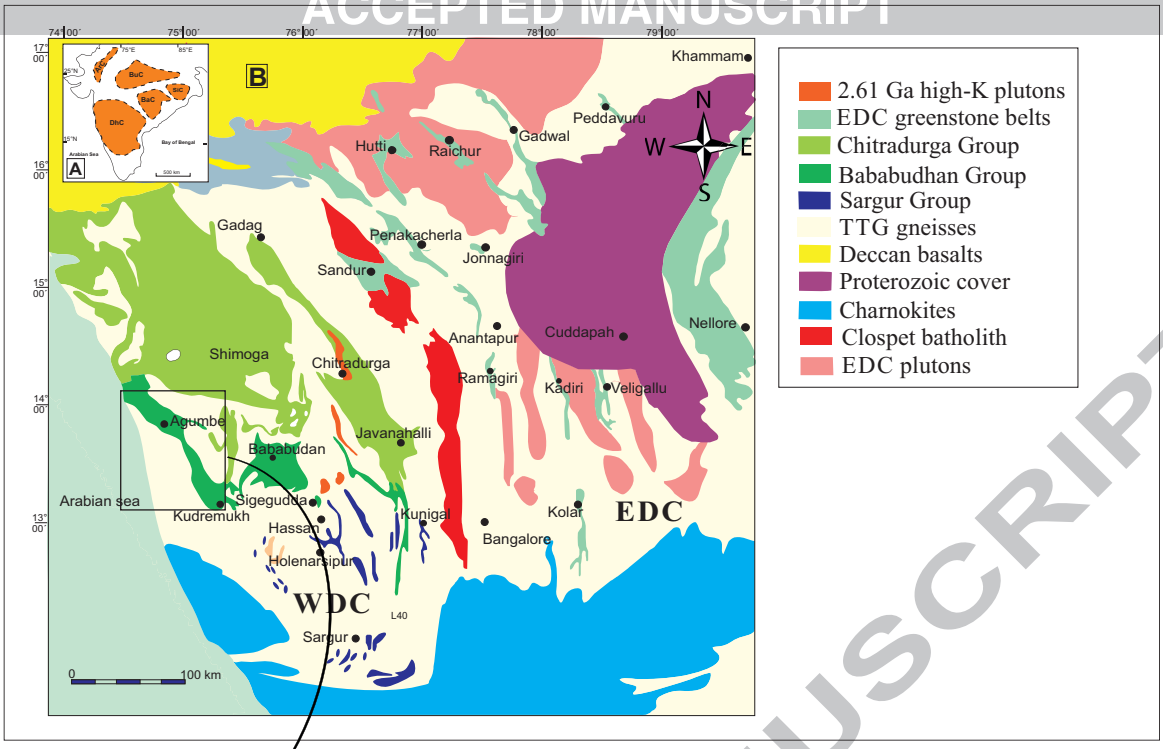

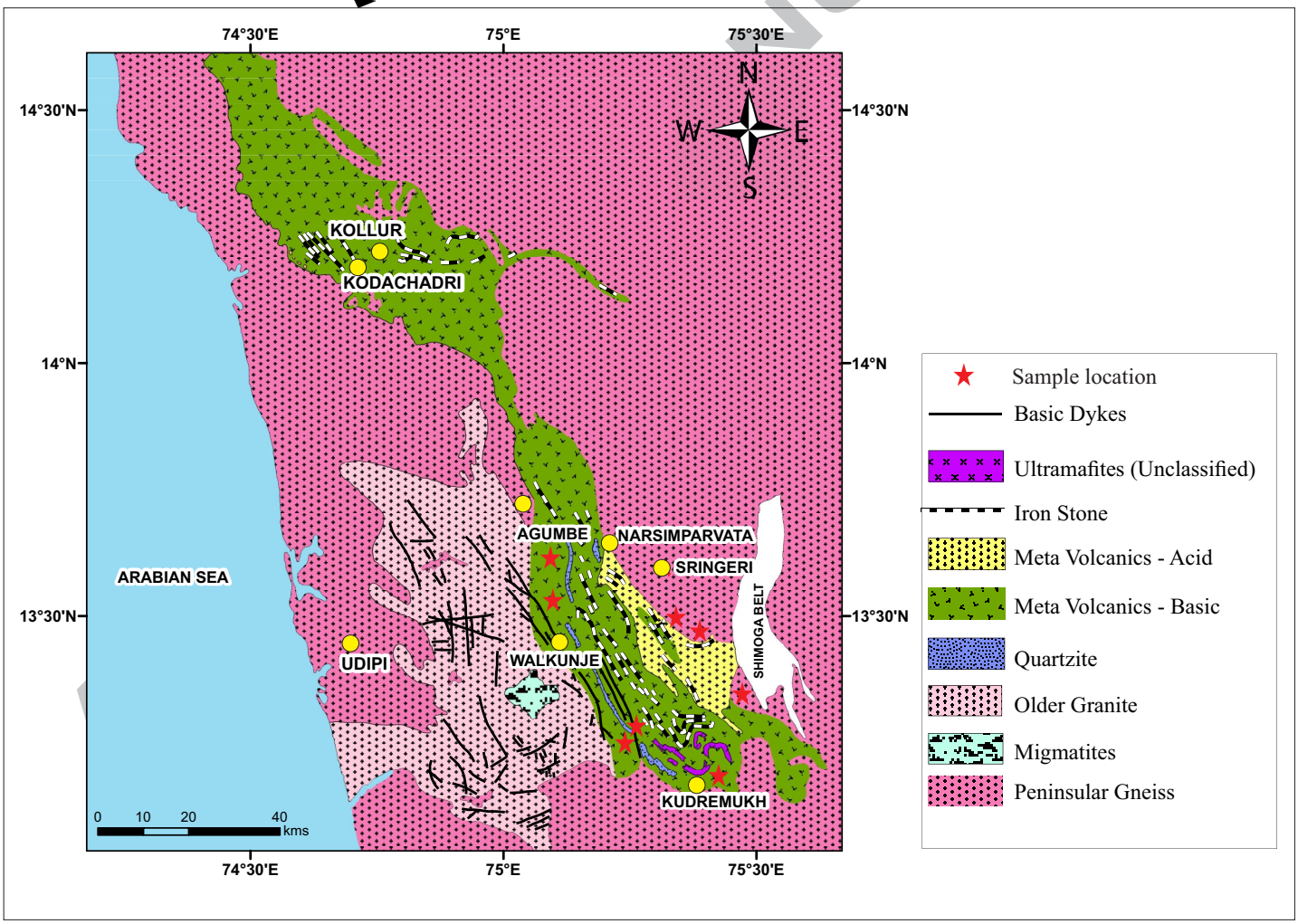

Fig. 1

Fig.2

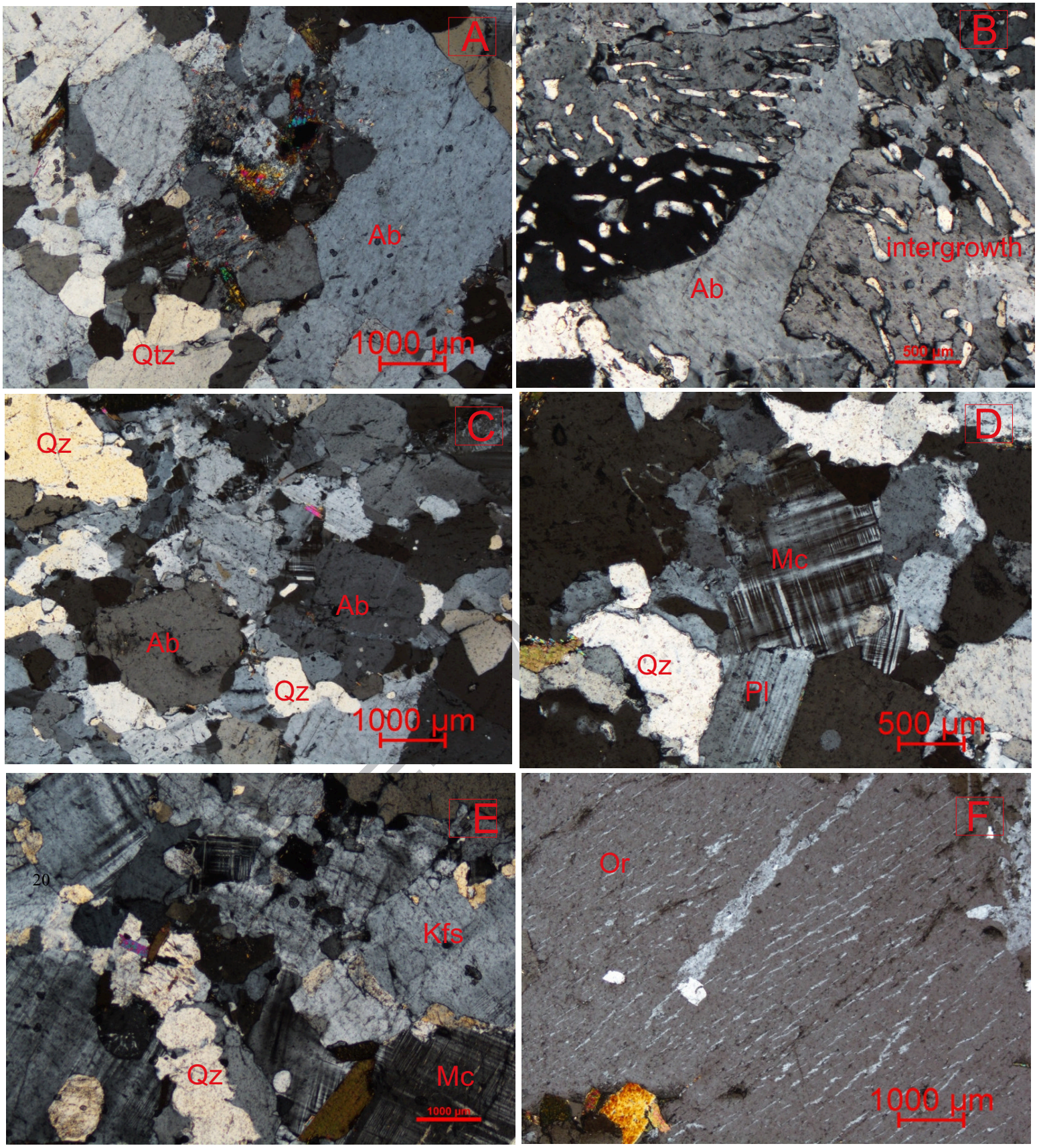
A
Ab
Qtz
1000 µm
B
intergrowth
Ab
500 µm
C
Qz
Ab
Ab
Qz
1000 µm
D
Mc
Qz
Pl
500 µm
E
Kfs
Qz
Mc
1000 µm
F
Or
1000 µm

Fig 3 (contd..)

Fig 3

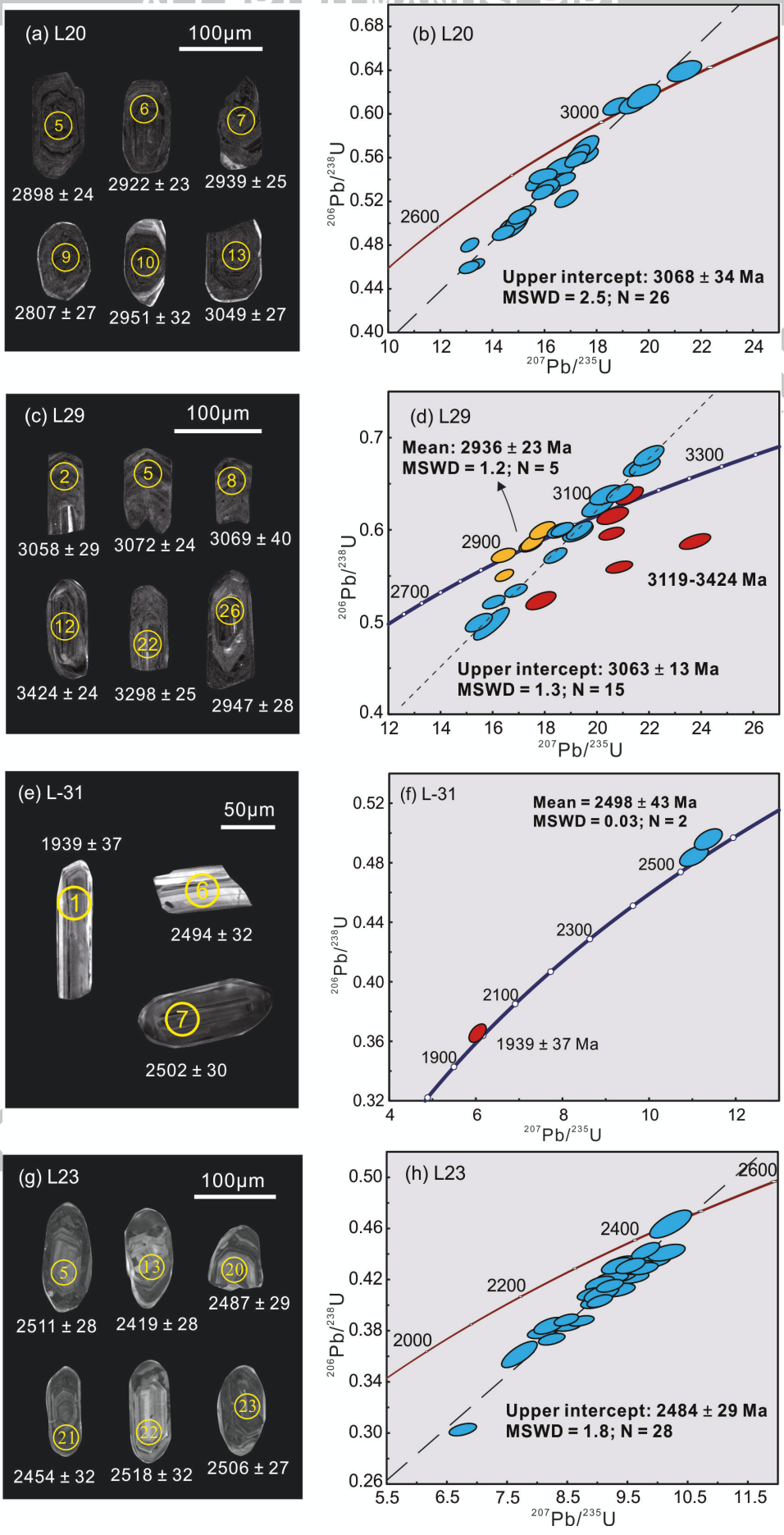

Fig. 4

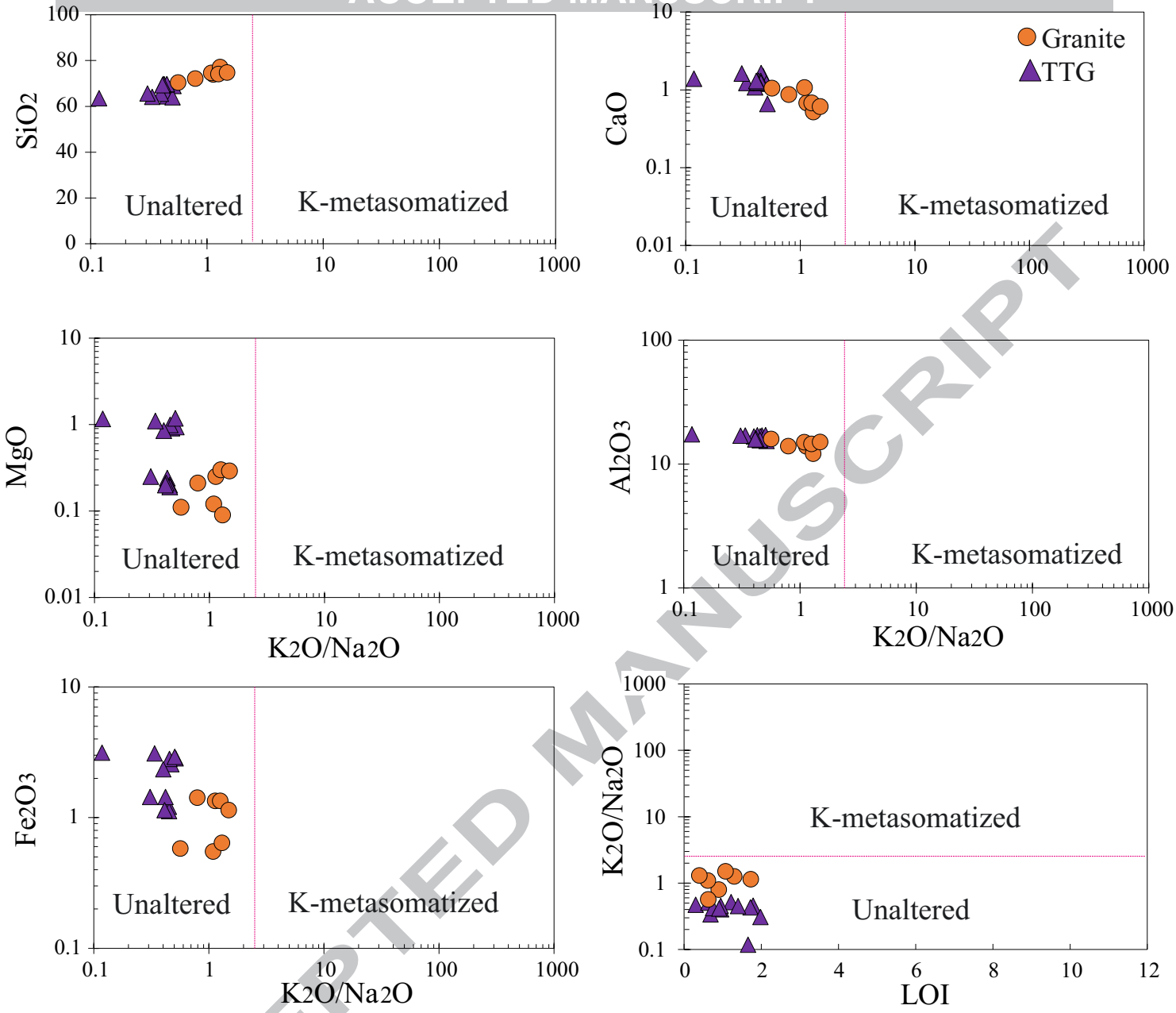

Fig. 5

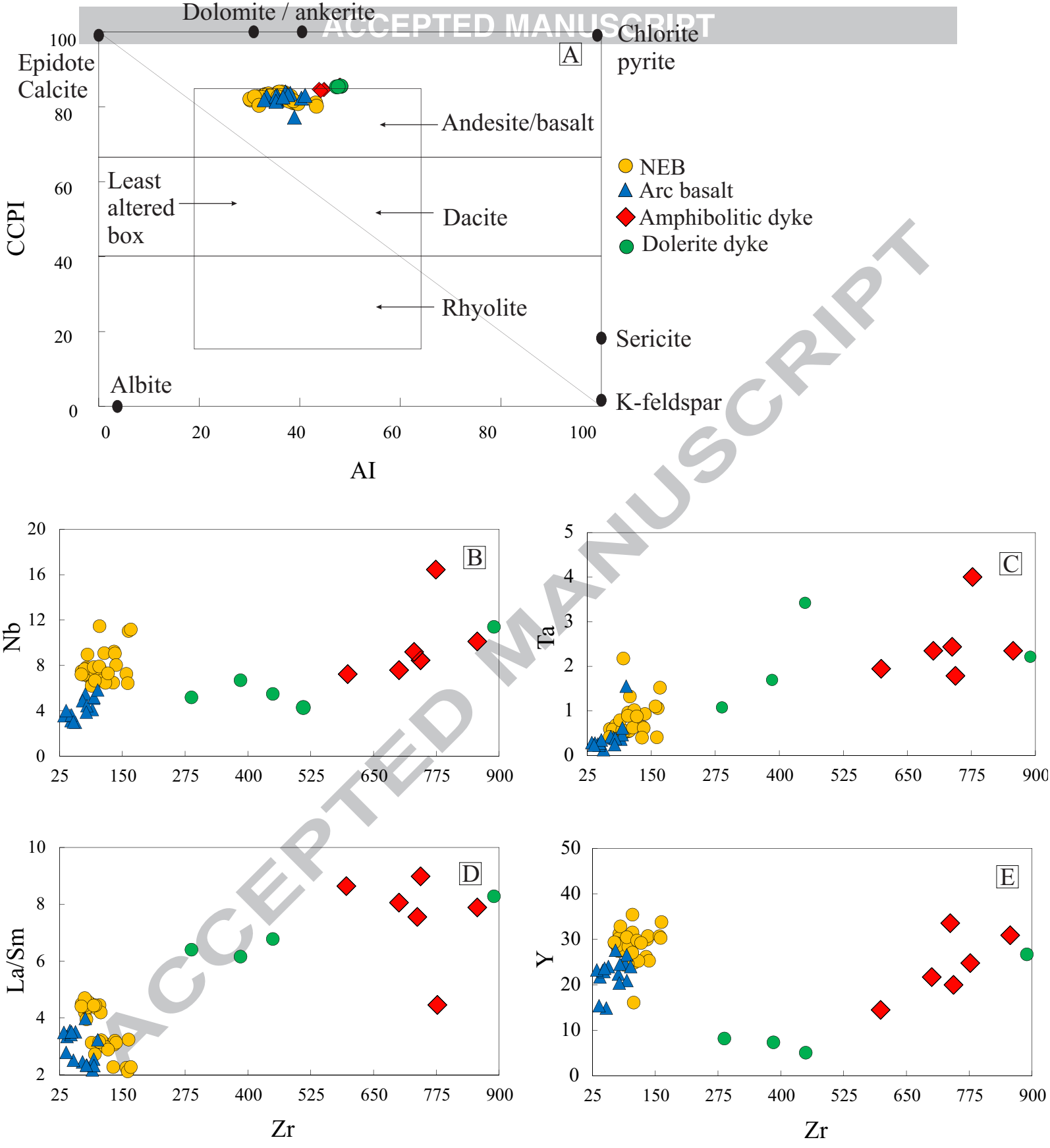

Fig. 6

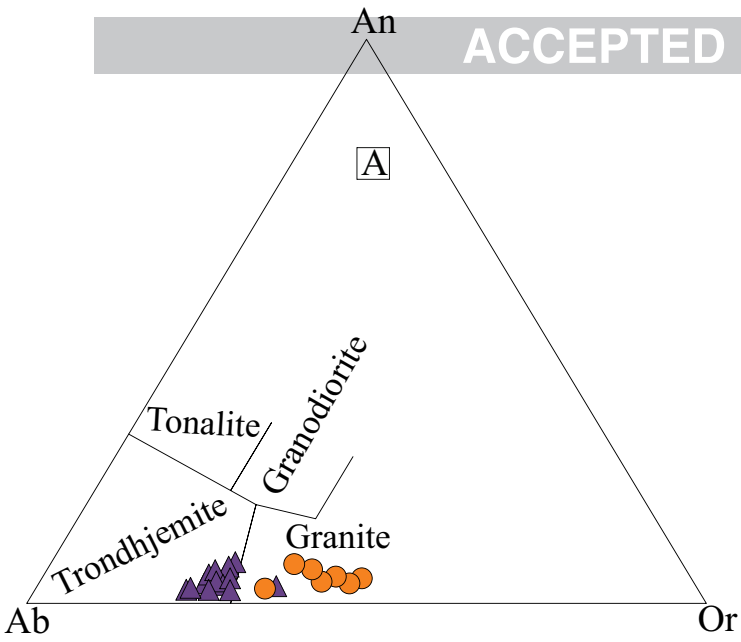

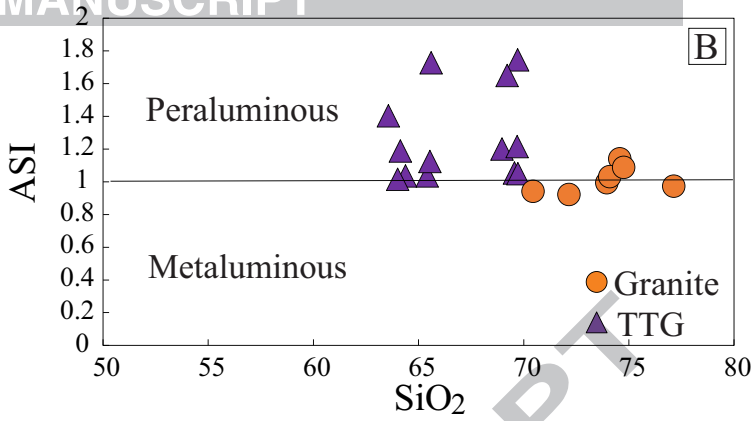

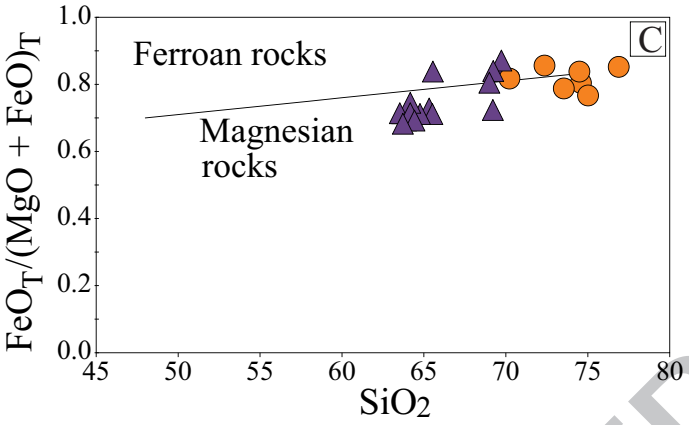

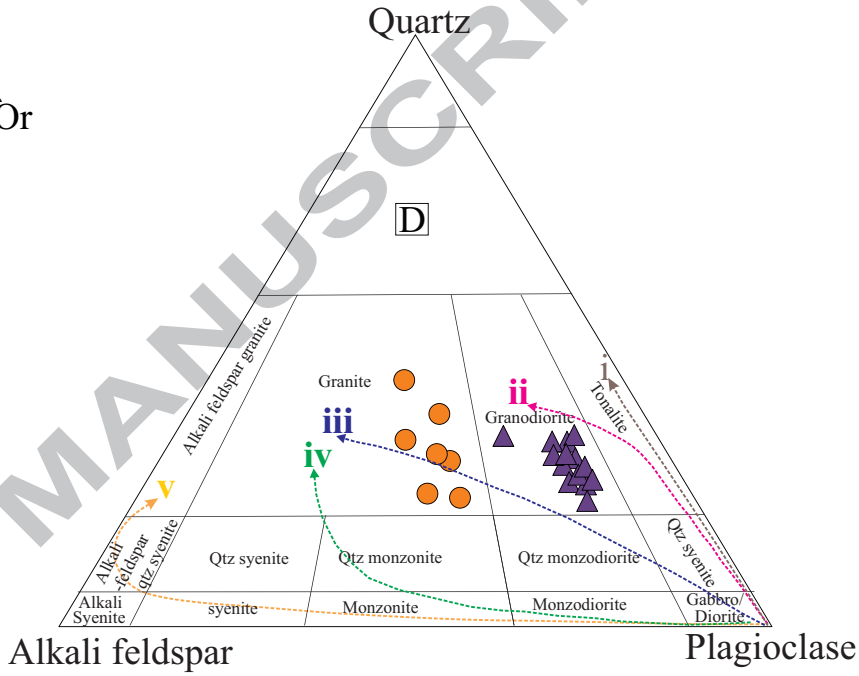

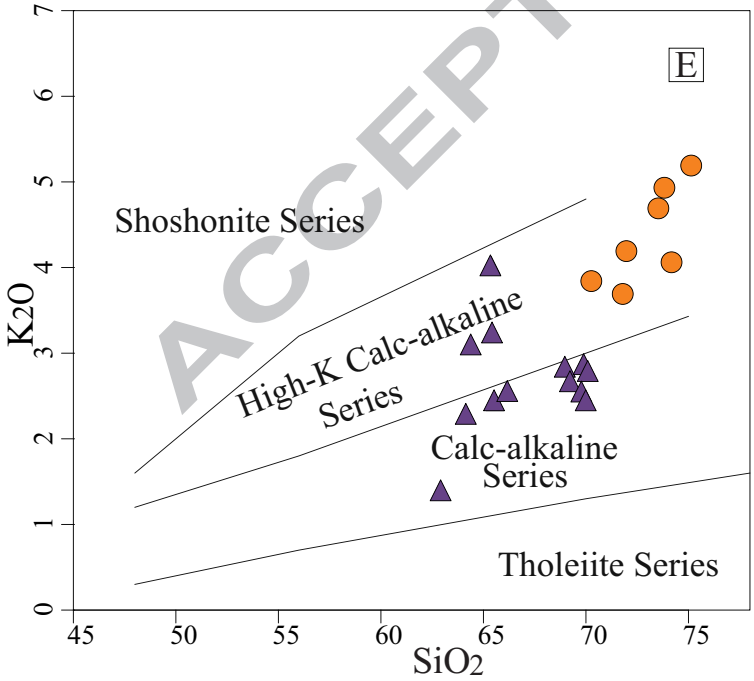

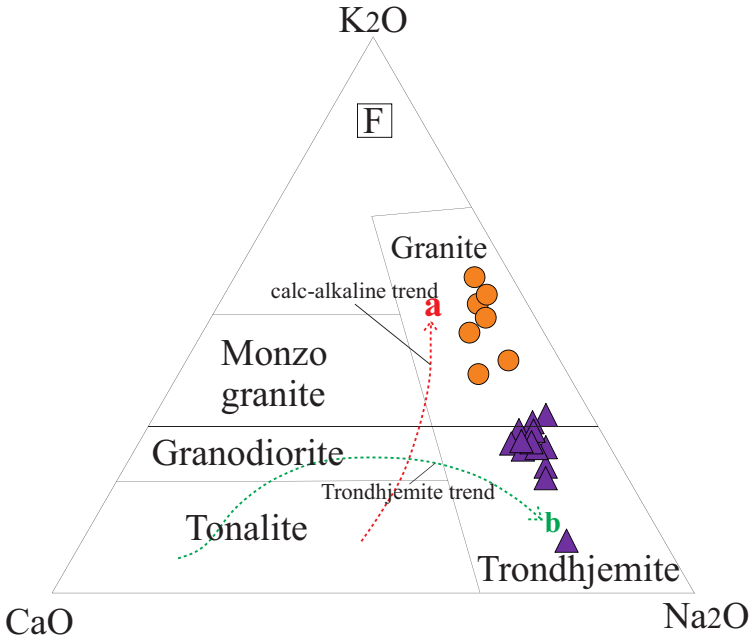

Fig.7

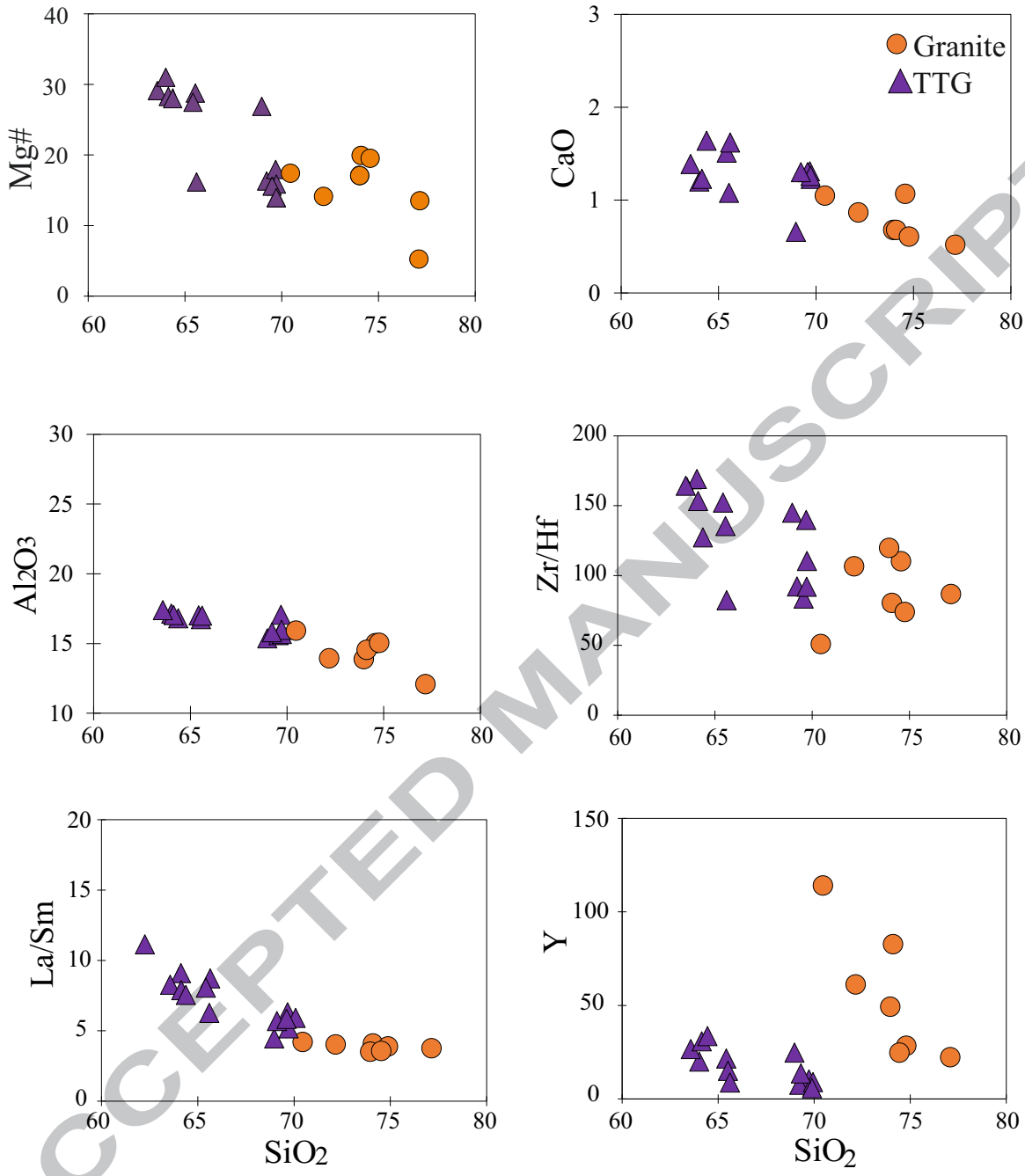

Fig. 8

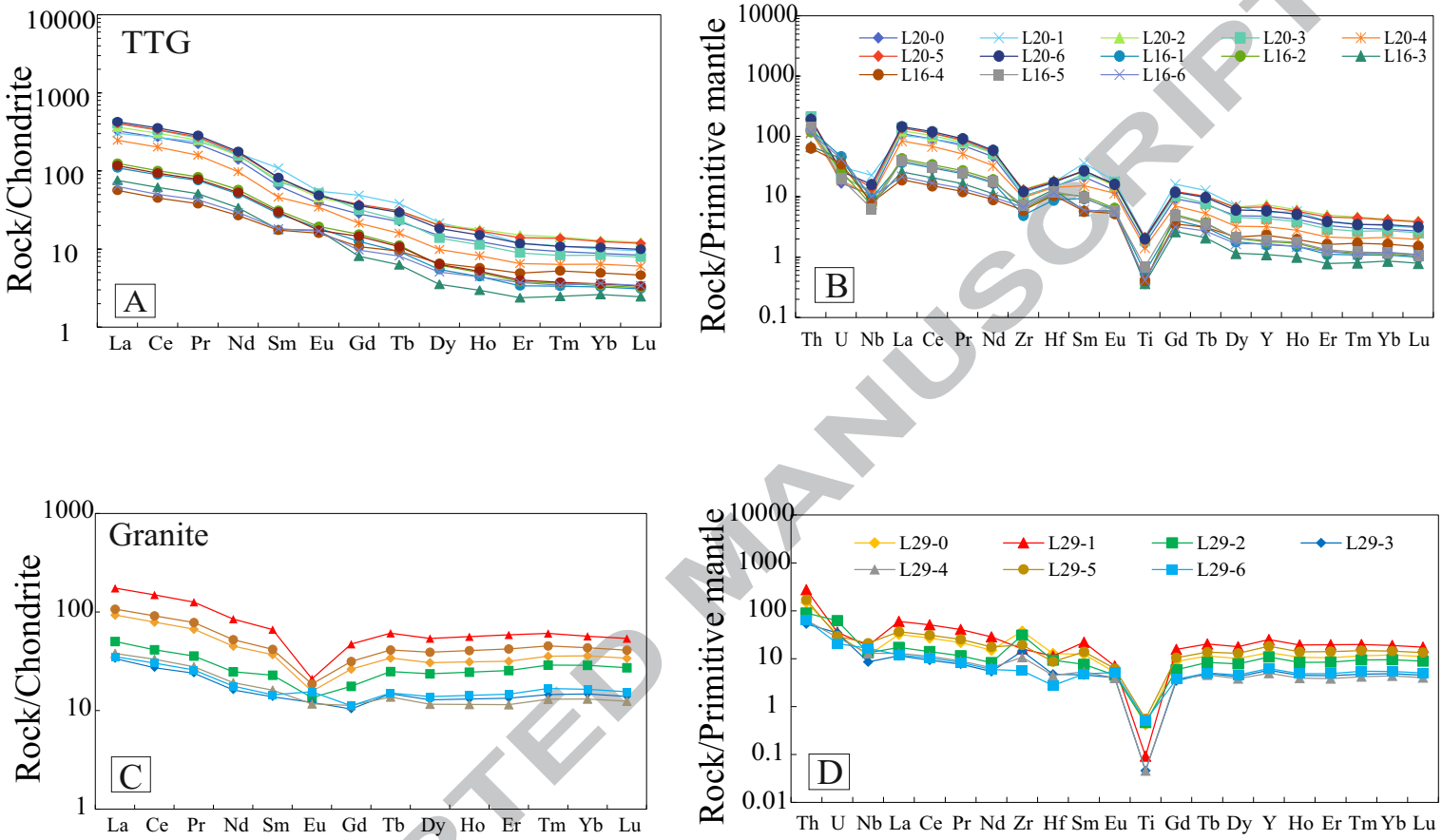

Fig.9

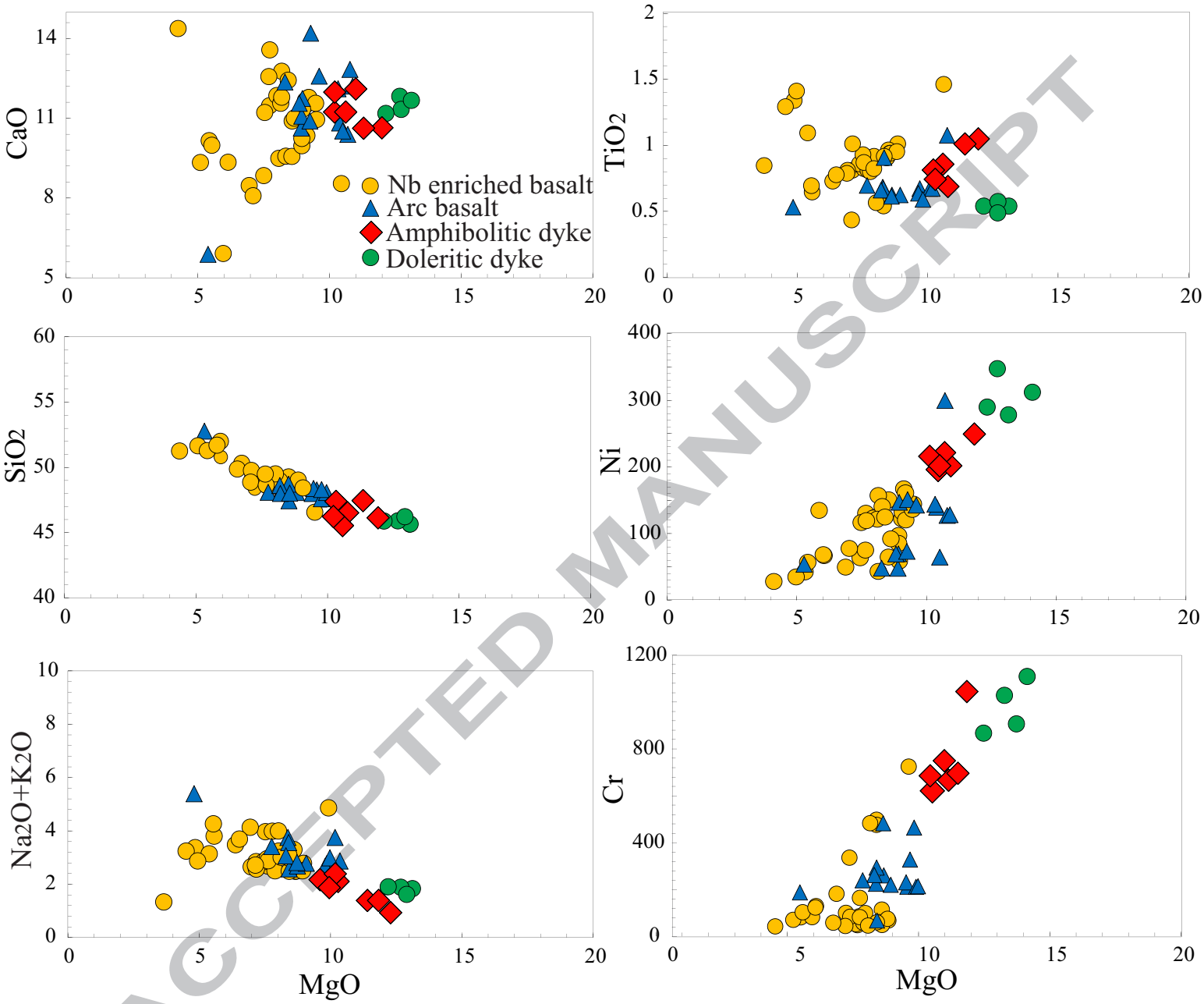

Fig 11

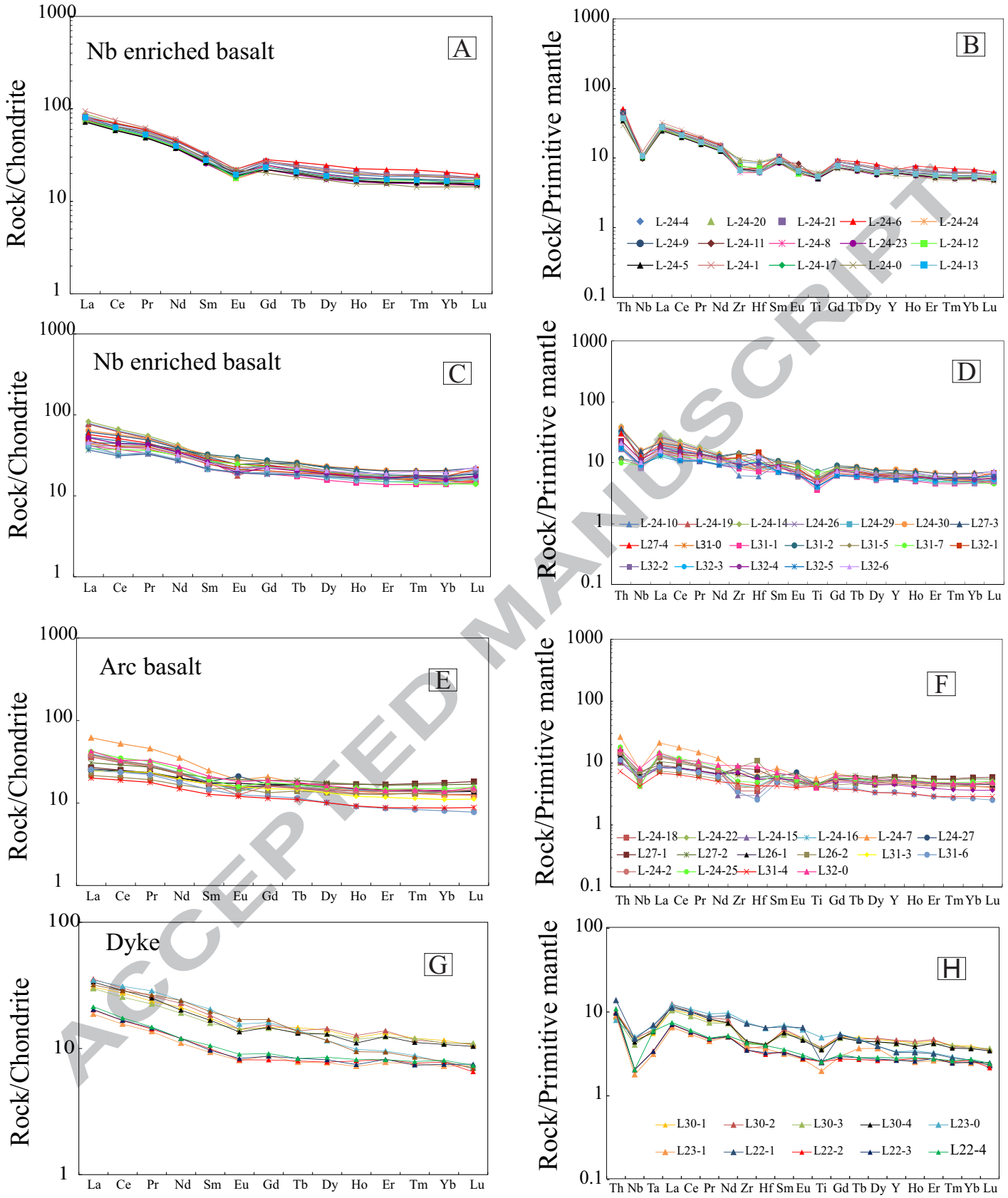

Fig.12

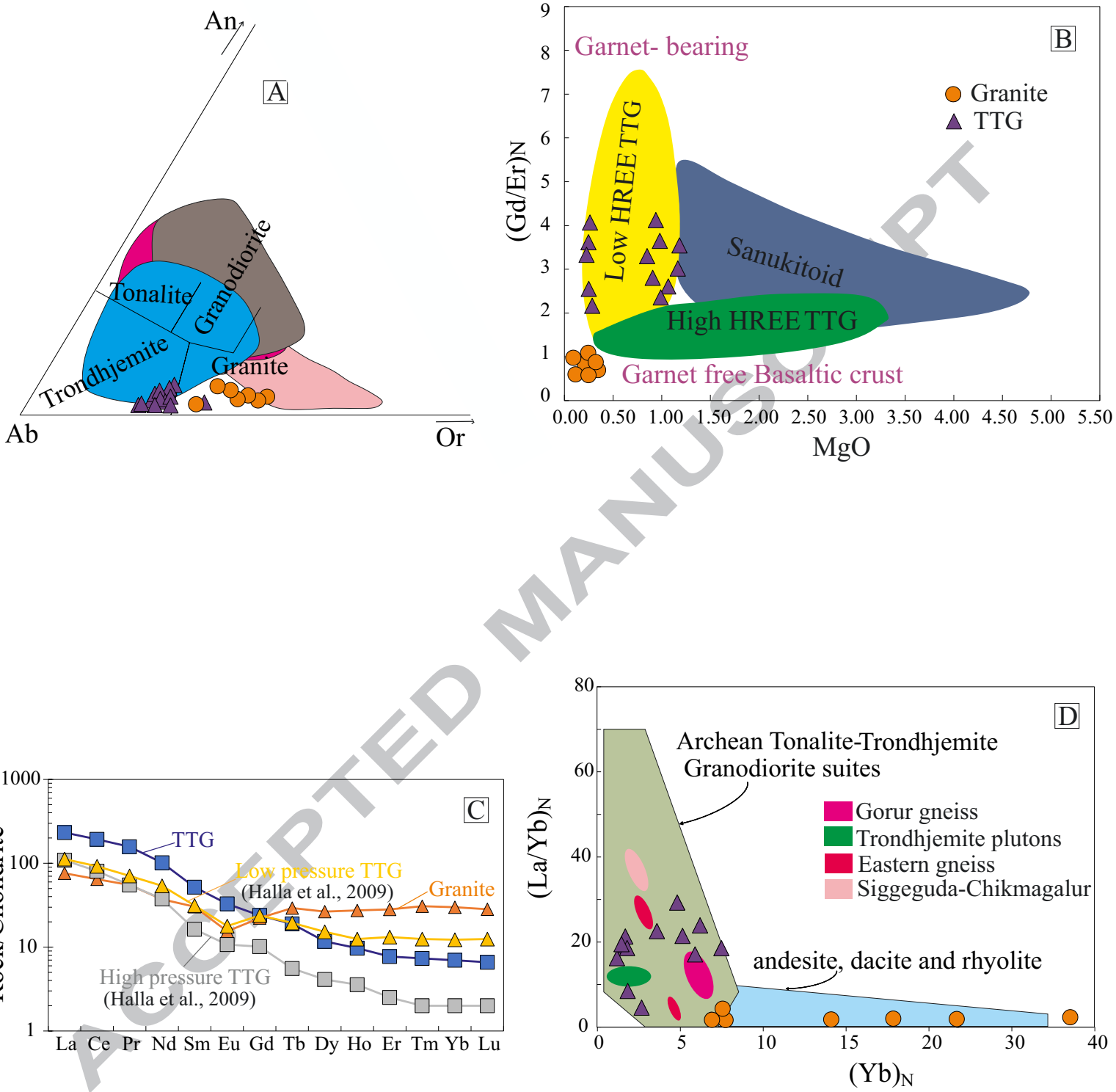

Fig 13

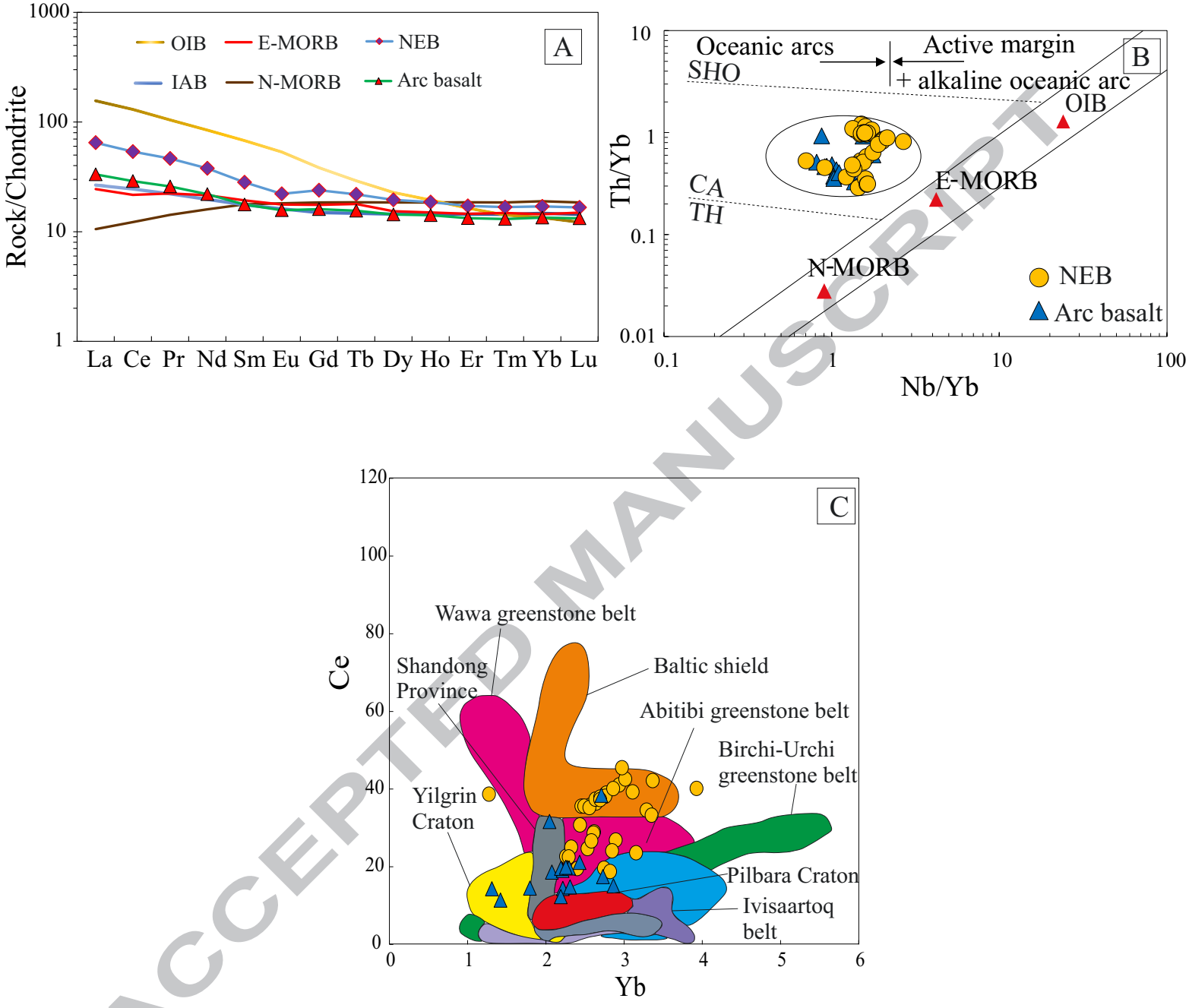

Fig 14

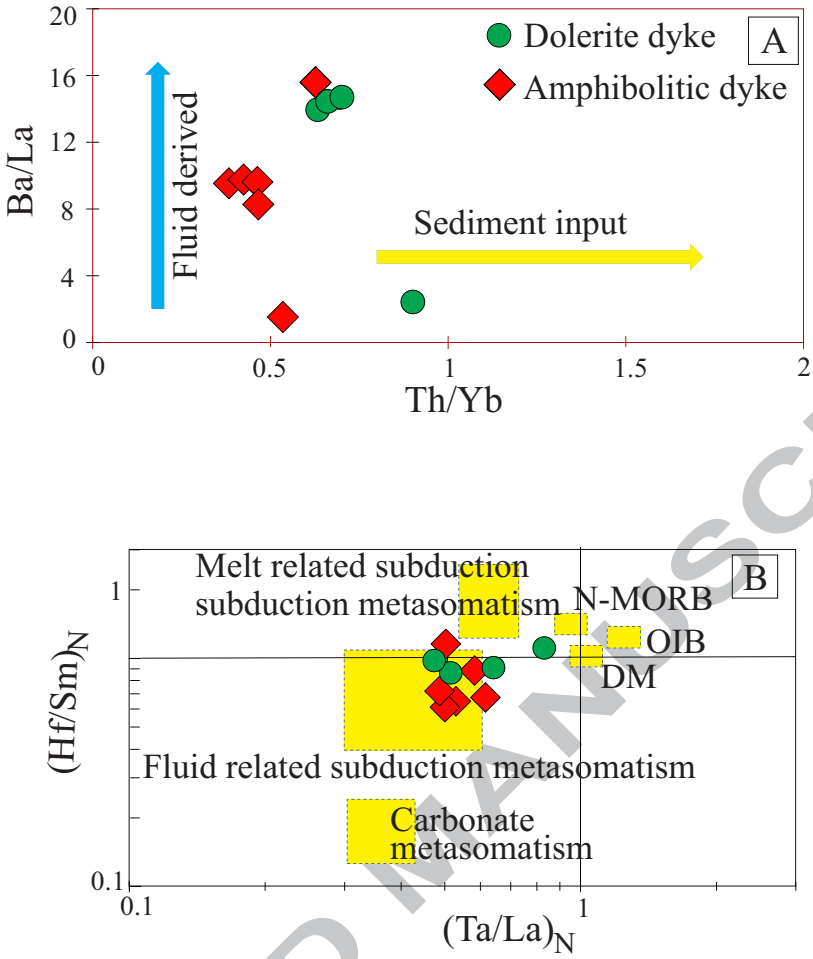

Fig 15

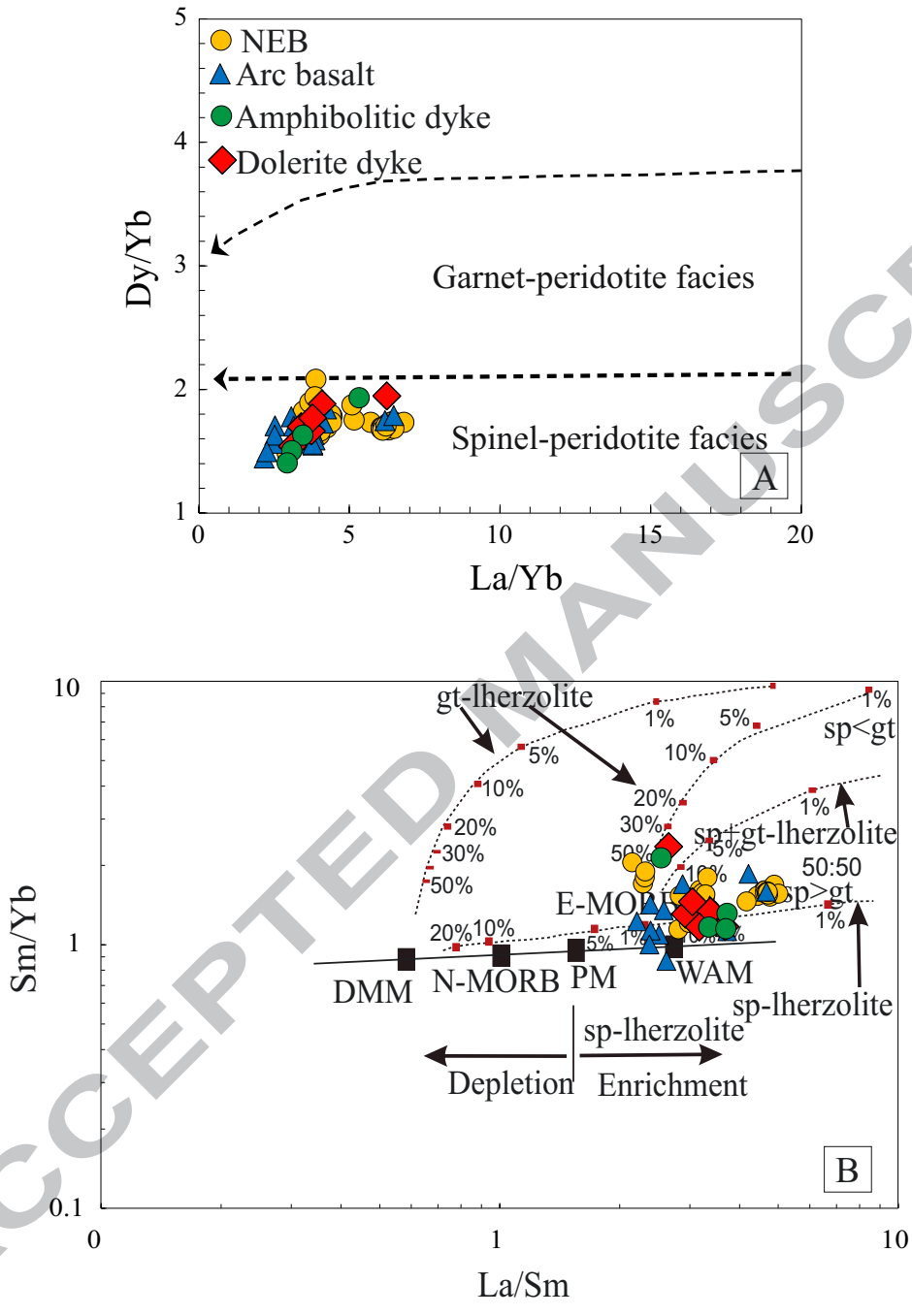

Fig. 16

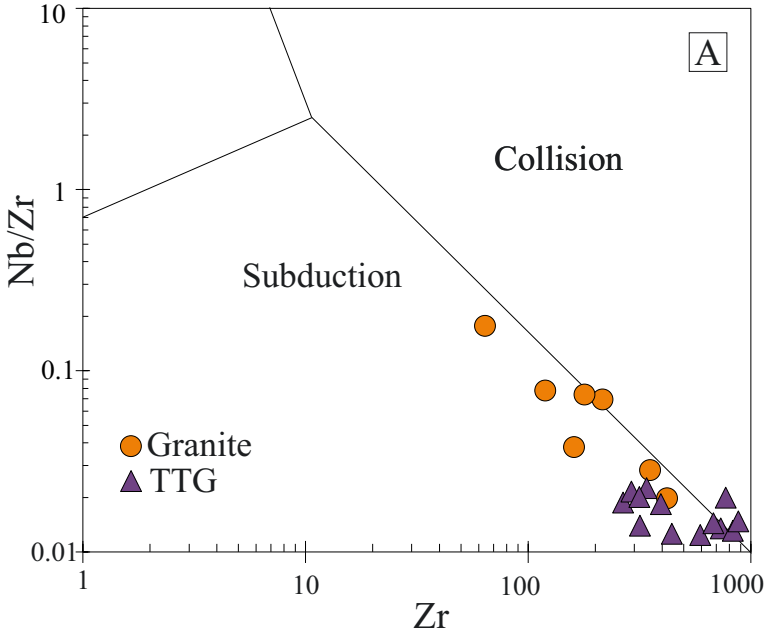

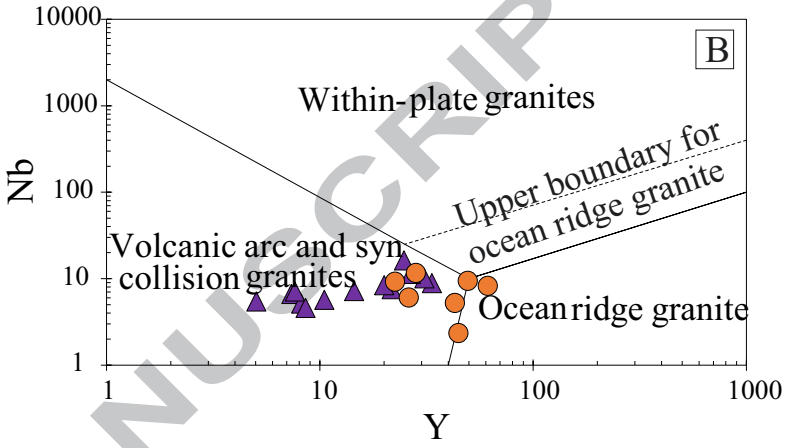

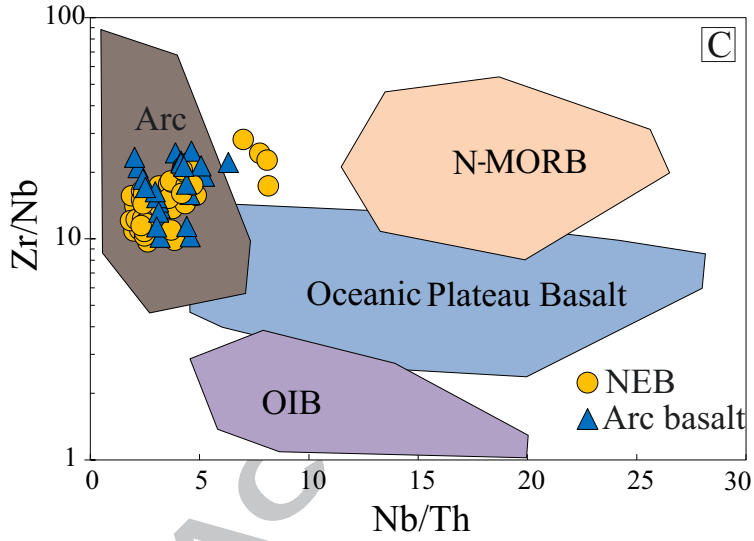

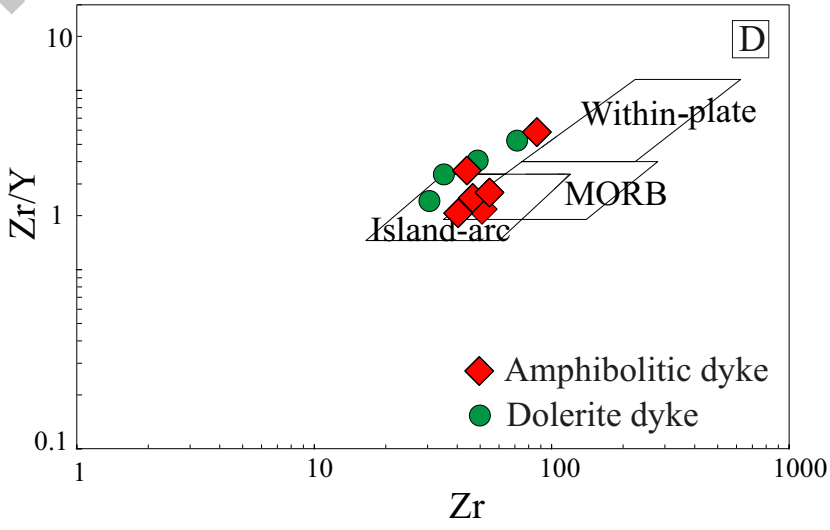

Fig. 17

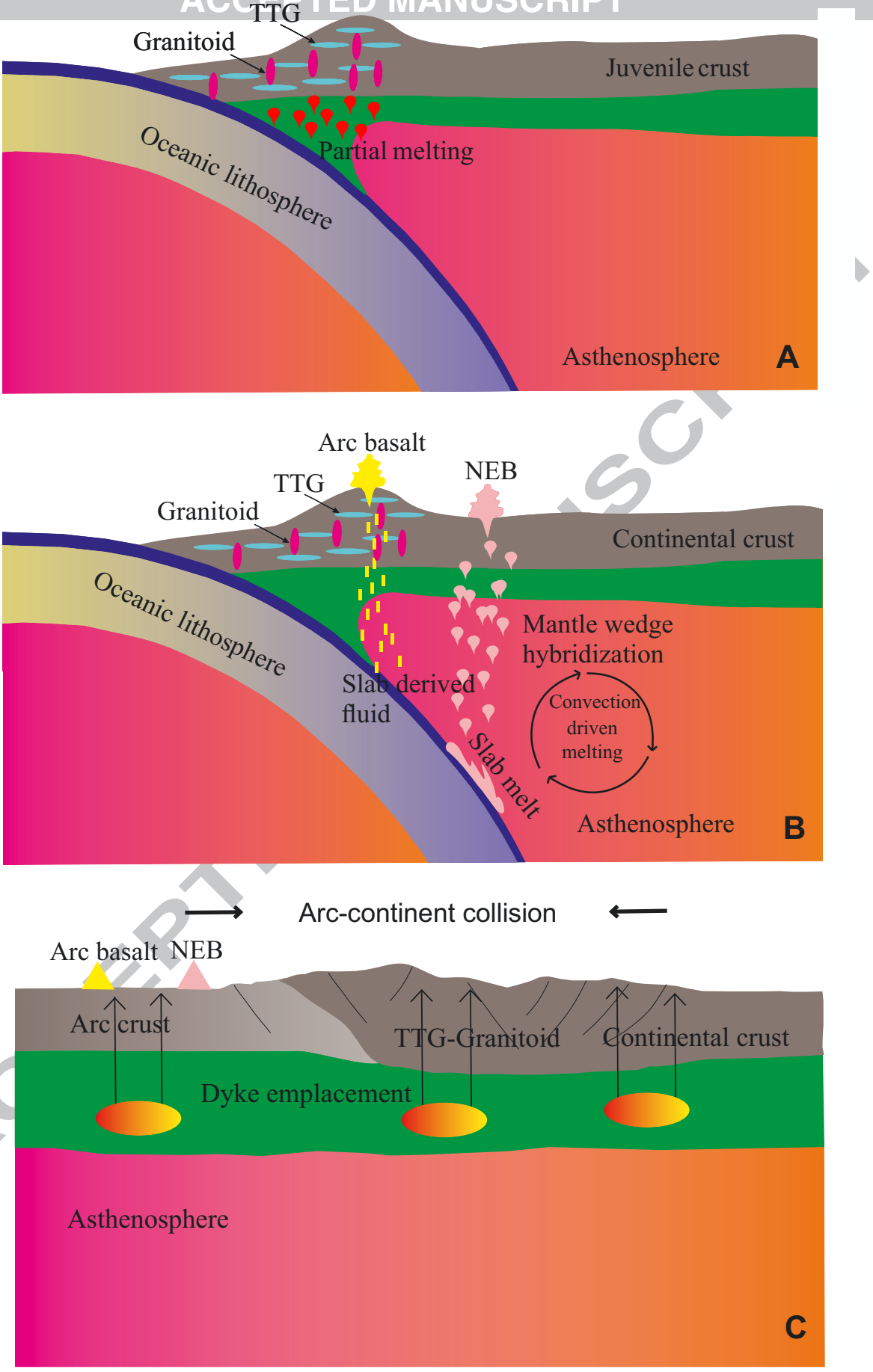

Fig 18

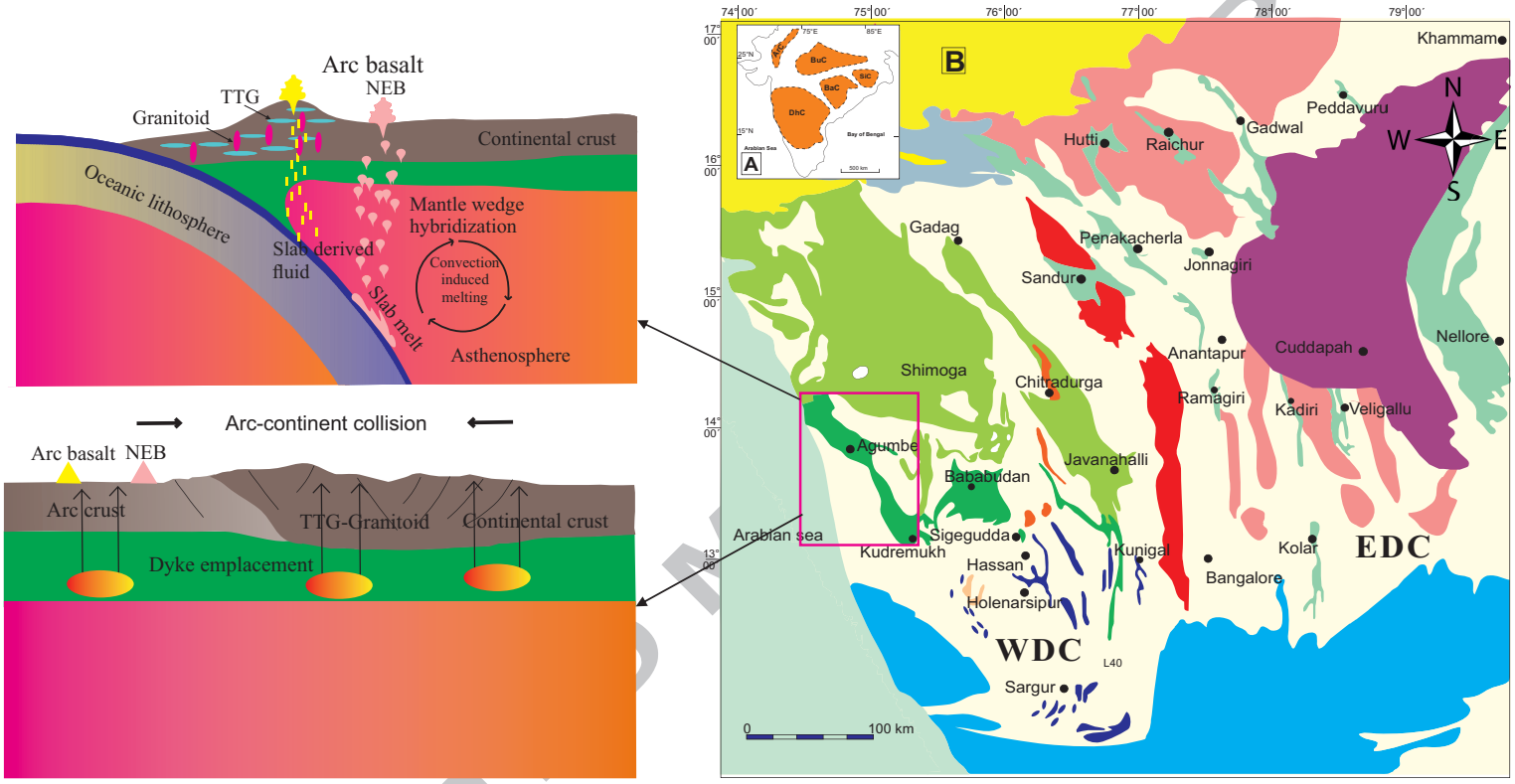

Graphical abstract